The Electronic, Structural, and Magnetic Properties of the Chromium Dihalides - from the Gas-phase to the Solid-state

A thesis submitted in partial fulfillment of the requirements of the degree

of

Doctor of Philosophy

in

Theoretical Chemistry

at

Massey University, Albany

New Zealand

Brian Michael Vest

June 10, 2008

Contents

List of Figures

List of Tables

Abstract

Unrestricted Kohn-Sham (broken symmetry) density functional calculations have been used to determine the low-energy geometries of the chromium dihalide molecules (CrX_2) and their clusters, Cr_2X_4, Cr_3X_6, and Cr_4X_8. The monomers are also investigated at a higher level, including coupled-cluster and state-average CASSCF computations. Our calculations show that the monomers have a $^5B_2$ ground state arising from the Renner-Teller distorted $^5\Pi_g$ transition state, leading to a bent geometry. The global minima of the gas-phase clusters of CrF_2 and $CrCl_2$ consist of two-dimensional, anti-ferromagnetically coupled chains of CrX_2 units forming four-membered, doubly bridged Cr_2X_2 rings, closely resembling their solid-state structures. The global minima of the $CrBr_2$ and CrI_2 clusters consist of the same two-dimensional chain-like structures for their dimers, but their trimers and tetramers consist of three-dimensional 'triangular' structures which contain two capping ligands bound to three chromium atoms along with a Cr-Cr bond. Each Cr atom within these clusters has spin quantum number S=2. There is approximately a constant change in energy, between 45-55 kcal/mol, with every new CrX_2 unit during cluster formation.

Information about the structure of the $CrCl_2$ clusters is used in the reanalysis of high-temperature electron diffraction data. The vapor at 1170 K contains about 77% monomeric molecules, 19% dimers, and a small amount of trimers. Monomeric $CrCl_2$ is found to be bent with a bond angle of 149(10)°, in good agreement with our computations.

Solid-state DFT calculations are performed on α-$CrCl_2$ to determine the lattice structure and spin-coupling constants for the Cr atoms within the crystals. The GGA (PW91) method produces a structure in good agreement with the literature. In the lowest energy structure, the spins of the Cr atoms within the chains along the crystallographic c-axis are anti-ferromagnetically coupled with four parallel spins situated almost exclusively in the d-bands of Cr along these chains. This anti-ferromagnetic coupling is also seen in the CrX_2 clusters.

Acknowledgements

First and foremost, I would like to give many thanks to my advisor Prof. Peter Schwerdtfeger. He has helped me more times than I can count with getting this thesis written and encouraged me to see the entire forest and not just the trees. I also want to thank him for his guidance, encouragement, and wonderful sense of humour. I would also like to thank Behnam Assadollahzadeh for his help with Gaussian and LaTeX templates and commands. He has also provided me with invaluable knowledge of various fishing spots around New Zealand and has taught me how to speak "proper" German. I want to also thank Andreas Hermann for his help with the solid-state of $CrCl_2$ and creating nice EPS files. Christian Thierfelder also deserves my thanks for helping me with various physics, mathematics, and Xmgrace problems. Lastly, I would like to thank Dr. Magdolna Hargittai for her help in understanding gas-phase electron diffraction.

Chapter 1

Introduction

The electronic and structural properties of the seemingly simple first-row transition metal dihalides have been debated by both theoreticians and experimentalists for many years [1, 2]. Infrared (IR) spectroscopy and electron diffraction (ED) have been the primary means of determining the geometry of these systems. The ED study of $CrCl_2$ [3], and CrF_2 [4] and the IR spectroscopic studies of different chromium dihalides [5–12] have been reported previously. However, the unambiguous determination of their geometry has been a problematic issue. According to the mass spectrometric study of chromium dihalides [13, 14] their vapor phase is complex, with considerable amount of larger clusters (up to tetramers) present beside the monomers. This fact makes the analysis of both electron diffraction and gas-phase spectroscopic results difficult, since the information concerning the monomeric molecules is buried among the ones corresponding to the different oligomers. Matrix-isolation infrared spectroscopic studies (MI-IR) might be a remedy to this problem, but they suffer from possible effects due to the interaction with the matrix. Another difficulty for spectroscopy is that chromium dihalides are rather involatile compounds, and the high temperatures needed to vaporize their molecules complicate the interpretation of the IR spectra because of the significant occupation of excited vibrational and rotational levels. Furthermore, these molecules have low-energy bending modes that are often outside the range of spectrometers. IR spectroscopy is also insensitive to the isotopic shifts of the antisymmetric stretching mode for quasi-linear molecules with bond angles between 150° to 180°, and this makes the determination of their shape ambiguous.

The general agreement from the above mentioned IR spectroscopic studies is that the structure of the chromium dihalides appear to be linear, with the primary evidence of linearity being the lack of a peak corresponding to the symmetric stretching frequency. However, the weak intensity of the symmetric stretching vibration for a quasi-linear molecule would be quite difficult to detect in the IR spectrum, and the possibility of non-linearity cannot be discarded. Further evidence for a possible bent structure stems from the earliest argon MI-IR experiment of $CrCl_2$ [5] in which the authors reported that the frequency pattern for the asymmetric stretching mode closely resembled that of a molecule with a bond angle between 120° and 150°. The earlier ED experiment by Hargittai et al. [3] reported a highly bent structure with a Cl-Cr-Cl bond angle of 110°. However, later it was communicated that due to the more complicated vapor composition than assumed in the study, the result should be disregarded [2].

In the last two decades, quantum chemical studies have become a powerful technique in aiding the interpretation of experimental data for the chromium dihalides. Before, earlier ligand field theory (LFT) was the accepted model to aid the interpretation of the spectra of transition metal halides. LFT predicts that the transition metal dihalides (MX_2) would be linear in the gas-phase, with a high-spin metal center, and only ionic interactions between the metal and the halides. In a linear MX_2 molecule ($D_{\infty h}$-symmetry ligand field), the relative energies of the metal d orbitals are in the order of $\delta_g < \pi_g < \sigma_g$ [15, 16]. Hence, LFT together with Hund's rule predicts that CrX_2 would have an electronic ground state of $^5\Sigma_g^+$ with an open shell electron configuration of $\delta_g^2\pi_g^2$. The two earliest ab-initio calculations [17, 18] on $CrCl_2$ agreed with this prediction, and the ground state of $CrCl_2$ was calculated to be the $^5\Sigma_g^+$ state with the $^5\Pi_g$ ($\delta_g^2\pi_g^1\sigma_g^1$) and $^5\Delta_g$ ($\delta_g^1\pi_g^2\sigma_g^1$) states being the first and second excited electronic states, respectively. However, the more recent DFT calculations by Wang and Schwarz [19] and also by Bridgeman and Bridgeman [20] gave the energy sequence $^5\Pi_g < {}^5\Sigma_g^+ < {}^5\Delta_g$. Bridgeman also suggested for the first time, that the first members of the transition metal dihalide series might have a bent equilibrium geometry with a flat bending potential. At about the same time, Jensen [21] determined a $^5B_2$ ground state for $CrCl_2$ as a result of the Renner-Teller type bending of the $^5\Pi_g$ state. He, again, noted a very flat bending potential with a barrier to inversion of only 100 cm^{-1} at a bond angle of 144.3°. In a more recent paper, Nielsen and Allendorf [22] also predicted the $^5B_2$ state as the ground state for CrF_2 and $CrCl_2$ using coupled cluster theory, CCSD(T). They also reported that the $^5B_2$ state for CrF_2

and $CrCl_2$ were only 0.8 and 0.1 kcal mol^{-1} lower in energy than the $^5\Pi_g$ transition state, respectively. This rather small energy difference is below the zero-point vibrational energy for the bending mode of $CrCl_2$. The barrier to inversion of the bent structure decreases going from F to I, and DFT calculations by Schiefenhövel et al. [23] predict that the ground state for CrI_2 is the $^5\Pi_g$ state. Interestingly, there are no papers published concerning the structure or ground state of $CrBr_2$. Based on the trends from previous quantum chemical studies, we predict that $CrBr_2$ could be either linear or bent with $^5\Sigma_g^+$, $^5\Pi_g$, or $^5B_2$ ground states as possible candidates. Such a small energy difference between the $^5\Pi_g$ and $^5B_2$ states makes the correct prediction of the ground state symmetry a formidable task for experimentalists, and to this date a definite assignment of the electronic ground state of any of the chromium dihalides remains an irresolute issue.

The breakdown of LFT for transition metal dihalides was discussed extensively by Wang and Schwarz [19] and Bridgeman and Bridgeman [20]. The computations show that ligand-induced $3d$-$4s$ hybridization from the partially filled $3d$ subshell on Cr lowers the energy of the σ_g orbital and the strong π-donating properties of the halide ligands tend to increase the energy of the π_g orbital. Jensen showed that inclusion of electron correlation is also important in determining the correct ground electronic state of $CrCl_2$; it increased the energy of the $^5\Sigma_g^+$ and $^5\Delta_g$ states relative to the $^5\Pi_g$ state by 3500 and 2600 cm^{-1}, respectively. Apparently, scalar relativistic effects contributed less than 600 cm^{-1} [21].

The computations up until now focused on the monomeric species. However, as discussed above, the vapor phase of the chromium dihalides contains a large amount of oligomers as well. The only computation on such species was done on Cr_2I_4 [23], where the structure was optimized with C_{2v} symmetry and a high-spin (nonet) ground state. No other possible geometry or spin-state was investigated, neither were the trimeric and tetrameric species.

Computations of transition metal dihalides face a number of serious difficulties. For transition metal containing compounds, wave-function based methods are computer time intensive and often require a multi-reference treatment [24]. Density functional theory, on the other hand, is plagued with correctly describing strong correlation and multi-reference character in such systems [25, 26]. As an example, Mott insulators of transition metal compounds are not well described by the generalized gradient approximation (GGA) in

DFT [27], and one is forced to add an on-site Hubbard-like repulsion term (LDA+U approach [28]). Spin symmetry breaking in transition metal compounds and consequently spin-spin coupling in magnetic materials are also affected by these deficiencies [29, 30].

In this thesis, we attempt to determine the gas-phase geometry and ground state properties of the series of chromium dihalide monomers, dimers, trimers, and tetramers $(CrX_2)_n$ with X=F–I and n=1–4, with an emphasis on $CrCl_2$, as there is a lack of experimental and/or quantum chemical data on the remaining dihalides. As mentioned previously, mass spectrometric studies have shown that oligomers up to the tetramers have been detected in the gas-phase. Hence, we will determine the geometry and magnetic properties of the chromium dihalide oligomers up to the tetramers as well as calculate their thermodynamic values. The shortcomings of DFT in correctly describing magnetic materials are addressed in detail, and the results of our DFT calculations for the monomers and dimers are compared with those from coupled-cluster theory (CCSD(T)) and complete active-space SCF (CASSCF) calculations. We also use our calculated global minima for the $CrCl_2$ monomers to the trimers in a re-evaluation of a previous ED experiment by Hargittai and coworkers [3].

The theory is outlined in the next chapter. The results of our quantum chemical investigations and electron diffraction analysis is given in Chapter 3. General trends from our investigations can be found in Chapter 4, and our conclusions are outlined in Chapter 5.

Chapter 2

Theory

2.1 Quantum Mechanics and Molecules

The interactions between n particles (electrons and nuclei) must be expressed quantum mechanically. The basic problem in non-relativistic quantum chemistry is thus to solve the (time-independent) Schrödinger equation [31]

$$\hat{H}|\Psi\rangle = E|\Psi\rangle \tag{2.1}$$

where $\hat{H}$ is the Hamilton operator for an atom or molecule that operates on the n-particle wavefunction Ψ. The total Hamilton operator can be written as a sum of kinetic and potential energy operators for the nuclei and electrons.

$$\hat{H} = \hat{T}_n + \hat{T}_e + \hat{V}_{ne} + \hat{V}_{ee} + \hat{V}_{nn} \tag{2.2}$$

The first two terms on the right hand side of Eq. 2.2 are the kinetic energy operators for the nuclei and electrons, respectively. The last three terms contain the Coulombic interactions among all of the nuclei and electrons. For a system with n electrons and N nuclei of mass M_N, Eq. 2.2 can be rewritten with quantum mechanical operators for each term (using atomic units)

$$\hat{H} = -\frac{1}{2}\sum_{i=1}^{n}\nabla_i^2 - \frac{1}{2M_N}\sum_{k=1}^{N}\nabla_k^2 - \sum_{i=1}^{n}\sum_{k=1}^{N}\frac{Z_k}{r_{ik}} + \sum_{i<j}\frac{1}{r_{ij}} + \sum_{k<l}\frac{Z_k Z_l}{R_{kl}} \tag{2.3}$$

where k, l runs over the nuclei and i, j over the electrons. Solving Eq. 2.3 for systems with many electrons and nuclei can become a daunting task. The Born-Oppenheimer

(BO) approximation [32] can therefore be used to simplify the problem by removing the nuclear degrees of freedom. This approximation is validated on the basis that nuclei are significantly more massive than electrons; hence, electronic relaxation occurs in a much shorter time frame with respect to nuclear motion. If this is assumed, then the second term (nuclear kinetic energy) can be neglected (clamped nucleus approximation). The last term involving Coulombic nuclear-nuclear interactions can be separated from the electronic part and treated as a constant. Thus, the BO approximation decouples the nuclear-electronic problem to a set of equations which describe electrons moving in a potential created by the static field of the nuclei. The time-independent, non-relativistic Schrödinger equation simplifies to

$$\hat{H}_{el}|\Psi_{el}\rangle = E_{el}|\Psi_{el}\rangle \tag{2.4}$$

where

$$\hat{H}_{el} = -\frac{1}{2}\sum_{i=1}^{n}\nabla_i^2 - \sum_{i=1}^{n}\sum_{k=1}^{N}\frac{Z_k}{r_{ik}} + \sum_{i<j}\frac{1}{r_{ij}} \tag{2.5}$$

and

$$E_{tot} = E_{el} + \sum_{k<l}\frac{Z_k Z_l}{R_{kl}} \tag{2.6}$$

When solving the molecular Schrödinger equation, the electronic wavefunction Ψ_{el} (which will be labeled as Ψ for the rest of the chapter), is unknown, and an initial guess of the wavefunction needs to be chosen. Certain properties such as the indistinguishability of electrons and the antisymmetry (Pauli principle) of Ψ with respect to electron permutation must be obeyed. Also, the efficiency in quantum chemical calculations is based on the choice of the trial wavefunction Ψ, and a function that is prohibitively complex should not be chosen. Slater [33] devised a way to satisfy the first two requirements by expressing the electronic wavefunction in a determinantal form, called a Slater Determinant (SD). The SD can be constructed from n spin orbitals χ_n by [34]:

$$\Psi(\mathbf{x_n}) = (n!)^{-1/2}\begin{vmatrix} \chi_1(\mathbf{x_1}) & \chi_1(\mathbf{x_2}) & \chi_1(\mathbf{x_3}) & \cdots & \chi_1(\mathbf{x_n}) \\ \chi_2(\mathbf{x_1}) & \chi_2(\mathbf{x_2}) & \chi_2(\mathbf{x_3}) & \cdots & \chi_2(\mathbf{x_n}) \\ \vdots & \vdots & \vdots & \vdots & \vdots \\ \chi_n(\mathbf{x_1}) & \chi_n(\mathbf{x_2}) & \chi_n(\mathbf{x_3}) & \cdots & \chi_n(\mathbf{x_n}) \end{vmatrix} \tag{2.7}$$

There are just two possible spin "functions" (α and β), and the generation of spin functions which are mixtures of these two are usually not considered. Hence, the computational

problem is the determination of the spatial orbitals (ψ_i) which are the spatially dependent part of χ_i:

$$\chi_i(\mathbf{x}) = \psi_i(\mathbf{r})\sigma \tag{2.8}$$

where σ can be either α or β spin. The spatial functions ($\psi_i(\mathbf{r})$) can be expanded into a linear combination of basis functions which are fixed for a particular calculation and are chosen based on both theoretical and practical grounds. These basis functions ($\phi_k(\mathbf{r})$) are the key elements to the successful calculation of any molecular electronic structure:

$$\psi_i(\mathbf{r}) = \sum_{k=1}^{m} \phi_k(\mathbf{r}) C_{ki} \tag{2.9}$$

where there are m basis functions with which to expand the n optimum molecular orbitals. The Hartree-Fock variational method optimizes the coefficients C_{ki} to ensure the lowest energy description of the molecular system. For practical reasons, these basis functions are usually chosen to be Gaussian functions centered at the nuclei. For example, the product of two Gaussians located at different centers is the same as a single Gaussian located at a center in-between. This property alone greatly speeds up the calculation of the two-electron integrals, which involve products of four Gaussians at different centers. Gaussian functions are also quite easy to implement into computational software packages.

The direct implementation of Gaussian functions into Eq. 2.9 would require a large amount of disk space, particulary for the storage of the electron repulsion integrals. A compromise is made in which the length of the explicit expansion in Eq. 2.9 is restricted by taking the basis functions themselves to be fixed linear combinations of primitive Gaussians, η_j:

$$\phi_k(\mathbf{r}) = \sum_{j=1}^{n_k} d_{jk} \eta_j(\mathbf{r}) \tag{2.10}$$

where the coefficients d_{jk} are fixed for a specific basis set. The general form of a primitive Gaussian located at the origin is a product of a Cartesian factor and an exponential:

$$\eta_j(\mathbf{r}) = N x^l y^m z^n (e^{-\alpha|\mathbf{r}|^2}) \tag{2.11}$$

where l, m, n are integers which characterize the type and order of the Gaussian function. The coefficient N is chosen to normalize the Gaussian function to unity.

2.2 Variational Principle

It is rarely the case that the wavefunction for a molecule is accurately known. In fact, not a single molecular wavefunction is known analytically. Any trial wavefunction consisting of a finite set of basis functions will always be an approximation of the exact wavefunction, Ψ_{ex}. It is helpful to know whether systematic changes in the trial wavefunction will lead to convergence and improvements in the wavefunction. The nonrelativistic Hamiltonian operator is bound from below, and the corresponding expectation values give an upper bound on the exact energy, E_o. If the trial wavefunction is the exact wavefunction, then

$$\begin{aligned} \langle \Psi | \Psi_{ex} \rangle &= 1 \\ \langle \Psi | \hat{H} | \Psi_{ex} \rangle &= E_o \end{aligned} \tag{2.12}$$

If they are not, then

$$\frac{\langle \Psi | \hat{H} | \Psi \rangle}{\langle \Psi | \Psi \rangle} > E_o \tag{2.13}$$

The variational principle is therefore written as:

$$\min_{\Psi \in \mathcal{H}} \frac{\langle \Psi | \hat{H} | \Psi \rangle}{\langle \Psi | \Psi \rangle} \geq E_o \tag{2.14}$$

Thus, it can be concluded that changes made to improve the trial wavefunction towards the limiting case of the exact wavefunction will lead to progressively lower energies because $\hat{H}$ is bound from below.

2.3 Hartree-Fock Theory

If Ψ consists of a SD of spin-orbitals ($|\Psi\rangle = |\Phi_1 \Phi_2 \Phi_3 \dots \Phi_n\rangle$), then the energy of the system can be calculated variationally. In the resulting Hartree-Fock (HF) equation, the one-electron Fock operator for a system of i electrons is given as

$$\hat{f}_i = \hat{h}_i + \sum_j^n (\hat{J}_{ij} - \hat{K}_{ij}) \tag{2.15}$$

where $\hat{h}_i$ includes the kinetic energy and Coulombic attraction operators among n electrons and N nuclei

$$\hat{h}_i = -\frac{1}{2}\nabla_i^2 - \sum_k^N \frac{Z_k}{r_{ik}} \tag{2.16}$$

The second term in Eq. 2.15 contains the classical Coulombic repulsion operator ($\hat{J}_{ij}$) between electrons i and j and the quantum mechanical exchange operator ($\hat{K}_{ij}$). The exchange operator has no classical analogue and arises from the antisymmetry of the wavefunction with respect to exchanging the coordinates of two electrons. For the total energy of a closed-shell system we get

$$\begin{aligned} E &= \sum_{i}^{n} \langle \Phi_i | \hat{f}_i | \Phi_i \rangle - \frac{1}{2} \sum_{ij}^{n} \langle \Phi_i | (\hat{J}_{ij} - \hat{K}_{ij}) | \Phi_i \rangle \qquad (2.17) \\ &= \sum_{i}^{n} \epsilon_i - \frac{1}{2} \sum_{ij}^{n} \left(\langle \Phi_i(1) \Phi_j(1) | \mathbf{r}_{12}^{-1} | \Phi_i(2) \Phi_j(2) \rangle - \langle \Phi_i(1) \Phi_j(2) | \mathbf{r}_{12}^{-1} | \Phi_j(1) \Phi_i(2) \rangle \right) \end{aligned}$$

The numbers within the parentheses represent electrons 1 and 2, and the $\mathbf{r}_{12}^{-1}$ operator represents the repulsive force between the charge densities of electrons 1 and 2. The resulting solution of the Schrödinger equation is described as independent electrons being influenced by nuclear attraction within a mean electric field created by all other electrons. The primary consequence of this is that HF theory does not include electron correlation.

2.4 Møller-Plesset Perturbation Theory

The underlying Møller-Plesset concept of perturbation theory is that HF provides a good first-order solution. This is expressed mathematically by decomposing the Hamilton operator into a reference ($\hat{H}_o$) and a perturbation ($\hat{V}$) operator. Hence, it is assumed that $\hat{V}$ is small relative to $\hat{H}_o$. HF theory gives roughly 99% of the total energy of a molecule in most cases; therefore, the correlation energy (E_{corr}) can be added as a small perturbation to the zeroth-order energy (E_o). For a perturbed system, the Schrödinger equation becomes

$$\hat{H}|\Psi\rangle = (\hat{H}_o + \hat{V})|\Psi\rangle = E_{tot} \qquad (2.18)$$

where

$$\hat{H}_o|\Psi_o\rangle = E_o|\Psi_o\rangle \qquad (2.19)$$

$$E_{tot} = E_o + E_{corr} \qquad (2.20)$$

If the perturbation is small, then Ψ and $\langle\Psi|\hat{H}|\Psi\rangle$ should be close to Ψ_o and $\langle\Psi_o|\hat{H}_o|\Psi_o\rangle$. It should therefore be possible to derive $\hat{H}$ and Ψ from $\hat{H}_o$ and Ψ_o from perturbation theory.

The wavefunction (Ψ) and corresponding eigenvalues (E_{tot}) for the perturbed system can be written as a Taylor expansion of nth order corrections $\Delta\Psi_n$ and ΔE_n. From this, it is possible to derive the following relationships

$$E_o = \langle\Psi_o|\hat{H}_o|\Psi_o\rangle \tag{2.21}$$

$$\Delta E_1 = \langle\Psi_o|\hat{V}|\Psi_o\rangle \tag{2.22}$$

$$\Delta E_2 = \langle\Psi_o|\hat{V}|\Delta\Psi_1\rangle \tag{2.23}$$

and so on for the nth perturbed term. The zeroth-order Hamilton operator ($\hat{H}_o$) is the same as the one-electron Fock operator given in Eq. 2.15, and Ψ_o is the HF wavefunction. Therefore, it can be seen that for a closed-shell system

$$E_o = \sum_i^n \langle\Phi_i|\hat{f}_i|\Phi_i\rangle = \sum_i^n \epsilon_i \tag{2.24}$$

$$\Delta E_1 = -\frac{1}{2}\sum_{ij}^n (\langle\Phi_i|\hat{J}_{ij} - \hat{K}_{ij}|\Phi_i\rangle) \tag{2.25}$$

The zeroth-order energy perturbation gives the sum of the molecular orbital energies. The energy at the first order of perturbation includes a correction for the overcounting of the electron-electron repulsion at zeroth-order. Hence, the sum of the zeroth and first-order energies is the same as the HF energy. The second order perturbation includes all doubly-excited occupations and ΔE_2 is written as:

$$\begin{aligned} \Delta E_2 &= \langle\Psi_o|V|\Delta\Psi_1\rangle \\ &= \sum_{a<b}\sum_{r<s} \frac{[\langle\Phi_a(1)\Phi_b(1)|\Phi_r(2)\Phi_s(2)\rangle - \langle\Phi_a(1)\Phi_r(1)|\Phi_b(2)\Phi_s(2)\rangle]^2}{\epsilon_a + \epsilon_b - \epsilon_r - \epsilon_s} \end{aligned} \tag{2.26}$$

The double sum is over all occupied orbitals a and b as well as over all virtual orbitals r and s. The sum of E_o, ΔE_1, and ΔE_2 is defined as the second-order Møller-Plesset [35] energy, or MP2 energy. MP2 is quite often used because most of the electron correlation comes from double excitations. However, MP2 tends to overestimate the correlation energy as well as underestimate bond lengths. Further perturbations which include third, fourth, fifth, etc. order excitations (labeled as MP3, MP4, MP5,...,MPn) can also be calculated but become considerably more time consuming computationally. MPn calculations assume that the HF reference wavefunction is close to representing the true wavefunction. If it is not a good starting point (in such cases as multi-reference systems), then the MPn calculation may fail to converge smoothly, leading to poor results, or even divergence.

2.5 Coupled-Cluster Theory

A better way to obtain the correlation energy is to expand the wavefunction as a linear combination of wavefunctions with all possible excitations considered.

$$|\Psi\rangle = c_o|\Psi_o\rangle + \sum_a \sum_r c_a^r|\Psi_a^r\rangle + \sum_{a<b} \sum_{r<s} c_{ab}^{rs}|\Psi_{ab}^{rs}\rangle + \ldots \tag{2.27}$$

The first term in Eq. 2.27 is the HF wavefunction, and the remaining terms consist of all possible determinants resulting from single, double, etc. excitations. When all of the possible excitations are considered, which is equivalent to a full configuration-interaction calculation (full-CI), then 100% of the correlation energy is calculated for a given basis set. However, such a calculation can only be achieved for very small systems with a few electrons and a small basis set.

Another way to rewrite the terms in Eq. 2.27 is to make it size-extensive, leading to coupled-cluster theory (CC) [36]. In CC, the best description of the true wavefunction within a given basis set can be written as

$$|\Psi_{cc}\rangle = e^{\mathbf{T}}\Psi_o \tag{2.28}$$

$$e^{\mathbf{T}} = \mathbf{1} + \mathbf{T} + \frac{1}{2}\mathbf{T}^2 + \frac{1}{6}\mathbf{T}^3 + \ldots = \sum_{n=0}^{\infty} \frac{1}{n!}\mathbf{T}^n \tag{2.29}$$

Each cluster operator $\mathbf{T}$ is defined as

$$\mathbf{T} = \mathbf{T}_1 + \mathbf{T}_2 + \ldots + \mathbf{T}_N \tag{2.30}$$

where N is the total number of electrons. Each $\mathbf{T}_i$ operator generates all ith excited Slater determinants from the HF reference wavefunction. For example, $\mathbf{T}_2$ operating on the HF wavefunction would lead to

$$\mathbf{T}_2|\Psi_o\rangle = \sum_{a<b} \sum_{r<s} t_{ab}^{rs}|\Psi_{ab}^{rs}\rangle \tag{2.31}$$

The coefficient t_{ab}^{rs} is called the amplitude for all double excitations and has a similar meaning to the c_{ab}^{rs} coefficient in Eq. 2.27. Combining Eqs. 2.29 and 2.30, the exponential operator can be written as

$$e^{\mathbf{T}} = \mathbf{1} + \mathbf{T}_1 + \left(\mathbf{T}_2 + \frac{1}{2}\mathbf{T}_1^2\right) + \left(\mathbf{T}_3 + \mathbf{T}_1\mathbf{T}_2 + \frac{1}{6}\mathbf{T}_1^3\right) + \ldots \tag{2.32}$$

The first two terms generate the HF reference wavefunction and all singles excitations. The first group of terms within the parenthesis generates all doubly excited terms, which

can be referred as connected ($\mathbf{T}_2$) and disconnected ($\mathbf{T}_1^2$) terms. The second parenthesis generates all triply excited terms, and so on. The coupled-cluster energy can be calculated by solving the Schrödinger equation for Ψ_{cc}.

$$\begin{aligned} E_{cc} &= \langle\Psi_o|\hat{H}e^{\mathbf{T}}|\Psi_o\rangle \\ &= \langle\Psi_o|\hat{H}(\mathbf{1}+\mathbf{T}_1+\mathbf{T}_2+\frac{1}{2}\mathbf{T}_1^2+\ldots)|\Psi_o\rangle \end{aligned} \tag{2.33}$$

The Hamilton operator only operates on one and two-electron terms. Given this property along with the definition of $\mathbf{T}_n$, Eq. 2.33 can be expanded to

$$\begin{aligned} E_{cc} &= \langle\Psi_o|\hat{H}|(\mathbf{1}+\mathbf{T}_1+\mathbf{T}_2+\frac{1}{2}\mathbf{T}_1^2)\Psi_o\rangle \\ &= E_o+\sum_r\sum_a t_a^r\langle\Psi_o|\hat{H}|\Psi_a^r\rangle+\sum_{a<b}\sum_{r<s}(t_{ab}^{rs}+t_a^rt_b^s-t_b^rt_a^s)\langle\Psi_o|\hat{H}|\Psi_{ab}^{rs}\rangle \\ &= E_o+\sum_{a<b}\sum_{r<s}(t_{ab}^{rs}+t_a^rt_b^s-t_b^rt_a^s)\langle\Psi_o|\hat{H}|\Psi_{ab}^{rs}\rangle \end{aligned} \tag{2.34}$$

Since Ψ_o is the HF wavefunction, Brillouin's theorem states that the second term in Eq. 2.34 must be zero.

The amplitudes for each excitation can be determined by multiplying a singly excited wavefunction $\langle\Psi_i^e|$ to the left of $\hat{H}e^{\mathbf{T}}|\Psi_o\rangle$ and integrating.

$$\begin{aligned} \langle\Psi_i^e|\hat{H}e^{\mathbf{T}}|\Psi_o\rangle &= E_{cc}\langle\Psi_i^e|e^{\mathbf{T}}\Psi_o\rangle \\ \langle\Psi_i^e|\hat{H}|(\mathbf{1}+\mathbf{T}_1+\mathbf{T}_2+\frac{1}{2}\mathbf{T}_1^2+\mathbf{T}_3+\mathbf{T}_1\mathbf{T}_2+\frac{1}{6}\mathbf{T}_1^3)\Psi_o\rangle &= E_{cc}\langle\Psi_i^e|\mathbf{T}_1\Psi_o\rangle \end{aligned} \tag{2.35}$$

Here, a set of coupled equations among all of the singles, doubles, and triples amplitudes are generated. All of the remaining $\mathbf{T}_N$ terms can be determined by multiplying by doubly, triply, quadruply, etc. excited wavefunctions instead of the singly excited wavefunction and integrating. The algorithms involved to solve the coupled equations can become very cumbersome and will not be discussed here. It is fair to say that only for small systems can a coupled-cluster calculation beyond triples be carried out. Therefore it is common for a coupled-cluster calculation to be truncated at the triples level of excitation. Including triple excitations can be done directly in a CCSDT calculation in which the cluster operator would include $\mathbf{T}_3$, or perturbatively in a CCSD(T) calculation. CCSD(T) has become the standard method for calculating electron correlation.

Unlike MP2 calculations, coupled-cluster is slightly more forgiving on the choice of the reference wavefunction. However, a CC calculation can become less accurate if the

HF guess provides a poor description of the wavefunction. This difficulty usually arises in multireference systems where a single determinant wavefunction is inadequate. In such a calculation, the singles amplitude is usually large, thus leading to oscillatory behavior for the higher-order excitations. A T_1-diagnostic calculation can be used to determine the quality of the CC result. It is defined as

$$T_1 = \frac{|\mathbf{t}_1|}{\sqrt{N}} \tag{2.36}$$

where $|\mathbf{t}_1|$ is the norm of the singles amplitude and N is the number of electrons. A value of $T_1 > 0.02$ indicates that the reference wavefunction has significant multi-determinant character, and the results of the CC calculation should be taken with caution.

2.6 Configuration Interaction

The HF solution provides, by definition, the best single-determinant description of the wavefunction, and the most rational way of including electron correlation is to create a linear combination of determinants that starts from the HF reference in which the electrons within the occupied orbitals are excited into virtual orbitals. Such a multi-determinant wavefunction is called configuration interaction (CI). Thus, the CI wavefunction would be

$$\Psi_{CI} = a_o\Psi_o + \sum_S a_S\Psi_S + \sum_D a_D\Psi_D + \sum_T a_T\Psi_T + \ldots = \sum_{i=0} a_i\Psi_i \tag{2.37}$$

The coefficients a_o, a_S, a_D, and a_T represent contributions from the reference wavefunction as well as from single, double, and triple excitations, respectively, and range in value from zero to one if the wavefunction is normalized. The energy of this system is minimized variationally such that the total CI wavefunction is normalized. This can be done by introducing a Lagrange multiplier, L, such that

$$L = \langle\Psi_{CI}|\hat{H}|\Psi_{CI}\rangle - \lambda[\langle\Psi_{CI}|\Psi_{CI}\rangle - 1] \tag{2.38}$$

The first bracket term is the total energy of the CI wavefunction. The second term represents the norm of the wavefunction. Expanding the CI wavefunction into multiple determinants, these two bracket terms become

$$\langle\Psi_{CI}|\hat{H}|\Psi_{CI}\rangle = \sum_{i=0}\sum_{j=0} a_i a_j\langle\Psi_i|\hat{H}|\Psi_j\rangle = \sum_{i=0} a_i^2 E_i + \sum_{i=0}\sum_{j\neq i} a_i a_j\langle\Psi_i|\hat{H}|\Psi_j\rangle \tag{2.39}$$

$$\langle \Psi_{CI} | \Psi_{CI} \rangle = \sum_{i=0} \sum_{j=0} a_i a_j \langle \Psi_i | \Psi_j \rangle = \sum_{i=0} a_i^2 \tag{2.40}$$

Placing these two terms into Eq. 2.38 and solving variationally yields

$$\frac{\delta L}{\delta a_i} = 2 \sum_j a_j \langle \Psi_i | \hat{H} | \Psi_j \rangle - 2\lambda a_i = 0$$

$$\frac{\delta L}{\delta a_i} = a_i (E_i - \lambda) + \sum_{j \neq i} a_j \langle \Psi_i | \hat{H} | \Psi_j \rangle = 0 \tag{2.41}$$

There is one equation for each a_i term in Eq. 2.41. Therefore, solving the variational problem leads to solving a set of CI secular equations.

If all possible combinations of excited determinants are included in Ψ_{CI}, then this is considered a full-CI calculation. In this calculation, all of the correlation energy is calculated, and Ψ_{CI} would be the best possible representation of the true wavefunction for a specific basis set. However, this type of calculation is very demanding and can only be done for small systems. Therefore, the CI calculation can be truncated to include specific excitations. A CIS calculation, which includes all single excitations, only leads to the HF reference energy. The lowest level CI calculation would be a CID calculation which includes only the doubly excited determinants. Larger numbers of configurations can be considered in CISD, CISDT, and CISDTQ calculations in which single, double, triple, and quadruple excitations are added to Ψ_{CI}. Since the computational time of a CI calculation increases factorally based on the number of excitations included, including up to the quadruple excitations can only be done for small systems.

2.7 Complete Active Space SCF

As mentioned previously, Ψ_{CI} is constructed by adding excited determinants to the HF wavefunction. For systems where a single-determinant wavefunction poorly describes the system, a full-CI calculation would be able to determine the correlation energy. Truncated CI calculations may not be able to properly describe a multi-reference system. This is because all of the important configurations may not be included in the series of determinants. For molecules with significant multireference character, such as transition metal compounds, it may be necessary to separate the HF wavefunction into specific parts and perform a full-CI only on the orbitals responsible for causing the multi-determinant behavior. This type of calculation is called a Complete Active Space SCF or CASSCF calculation.

The initial wavefunction for a CASSCF calculation is typically a converged R(O)HF reference wavefunction. This initial guess is then separated into three sections: inactive occupied orbitals, the active (occupied and virtual) space, and inactive virtual orbitals. The inactive occupied orbitals are all doubly occupied and are optimized during the SCF procedure, while the inactive virtual orbitals remain unoccupied. The orbitals within the active space are subjugated to a full-CI calculation. A CASSCF calculation is typically labeled as a CASSCF(n,m) calculation in which the active space consists of n electrons within m orbitals. The primary goal of a CASSCF calculation is not to calculate a large portion of the correlation energy. It is done to obtain all of the important configurations of a multi-determinant wavefunction and to recover all of the changes that occur in the correlation energy. The amount of computational time increases factorally with the increase in the number of possible configurations; hence, the selection of an appropriate active space is very important and requires more in-depth knowledge of the system at hand. The CI coefficients obtained from the active space of a CASSCF calculation do not have the same meaning as those from Eq. 2.37. The absolute value of the CI coefficients represent the weight of each configuration relative to other configurations. Again, the values of the CI coefficients can range from zero to one.

A CASSCF calculation often provides an unbalanced view of the electron correlation of the molecule, with only the active orbitals being correlated. Dynamic correlation can be calculated from a CASSCF wavefunction using two major techniques. The first method involves a truncated CI calculation with the reference wavefunction being the multi-determinant wavefunction instead of a single-determinant HF reference. This technique is labeled as a Multi-Reference Configuration Interaction or MRCI calculation. Truncating the MRCI to include only singles and doubles contributions can yield very accurate results; however, this type of calculation is computationally very expensive. The other technique involves an nth order Rayleigh-Schrödinger perturbation calculation from the CASSCF reference wavefunction and is called a CASPTn calculation. The computational technique involved in a CASPTn calculation is very similar to that of a Møller-Plesset calculation, and the computational details will not be described here. Since the CASSCF wavefunction will usually include all of the major determinants involved in a multi-reference system, it will provide a better reference wavefunction to perform a perturbative calculation. The level of perturbation is typically cut off to second (CASPT2) or third order (CASPT3) and often leads to very accurate results with less computational

effort than a MRCI calculation. However, the problem with any perturbative calculation is that the amount of perturbation is small with respect to the reference wavefunction. If an incorrect active space is chosen, then the results of a CASPTn calculation could be less accurate. In addition, if the energy differences among the orbitals are relatively close to one another (near degeneracy), then the energy could diverge. This can be seen from the denominator for the second order perturbative energy in Eq. 2.26. If the energies of the orbitals are closely spaced, then the value of $(\epsilon_a + \epsilon_b) - (\epsilon_r + \epsilon_s)$ will be close to zero, thus making the value of ΔE_2 very large.

2.8 Density Functional Theory

The basis of density functional theory (DFT) stemmed from a proof by Hohenberg and Kohn [37] that the ground state energy of a system can be determined completely by its electron density, $\rho(\mathbf{r})$. Kohn and Sham [38] devised a set of equations that could be used to calculate the energy of a system. The starting point of such a calculation involves creating a fictitious system of "non-interacting" electrons whose ground state electron density is identical to that of a real system where the electrons interact. The energy functional of such a system would be calculated by

$$E[\rho(\mathbf{r})] = T_e[\rho(\mathbf{r})] + V_{ne}[\rho(\mathbf{r})] + V_{ee}[\rho(\mathbf{r})] + \Delta T[\rho(\mathbf{r})] + \Delta V_{ee}[\rho(\mathbf{r})] \tag{2.42}$$

The first three terms on the right hand side of Eq. 2.42 are the kinetic energy term for a non-interacting system, the Coulombic attraction term between the nuclei and electrons, and the classical electron-electron repulsion term. The last two terms consist of corrections to the kinetic energy when going from a non-interacting to a real system and the non-classical electron-electron interactions, respectively. Within an orbital approach for the density, the energy functional can be rewritten as

$$\begin{aligned} E[\rho(\mathbf{r})] &= \sum_i^N \left(\langle \Phi_i | - \frac{1}{2}\nabla_i^2 | \Phi_i \rangle - \langle \Phi_i | \sum_k^M \frac{Z_k}{|\mathbf{r}_i - \mathbf{R}_k|} | \Phi_i \rangle \right) \\ &\quad + \sum_i^N \langle \Phi_i | \frac{1}{2} \int \frac{\rho(\mathbf{r}')}{|\mathbf{r}_i - \mathbf{r}'|} d\mathbf{r}' | \Phi_i \rangle + E_{xc}[\rho(\mathbf{r})] \end{aligned} \tag{2.43}$$

where Φ_i represents a Kohn-Sham orbital. The sums of i and k are over all electrons and nuclei, respectively. The E_{xc} term includes the corrections to the electron kinetic energy

as well as the non-classical repulsion terms and is labeled as the exchange-correlation energy. Within this approach, the one-electron density is expressed as

$$\rho(\mathbf{r}) = \sum_{i=1}^{N} \Phi_i^*(\mathbf{r})\Phi_i(\mathbf{r}) \tag{2.44}$$

The next step is to find the Kohn-Sham (KS) orbitals Φ_i that minimize the energy functional. This can be accomplished through a set of pseudoeigenvalue equations

$$h_i^{KS}\Phi_i = \epsilon_i\Phi_i \tag{2.45}$$

where h_i^{KS} is the one-electron KS operator, which is given by

$$h_i^{KS} = -\frac{1}{2}\nabla_i^2 - \sum_k^M \frac{Z_k}{|\mathbf{r}_i - \mathbf{R}_k|} + \int \frac{\rho(\mathbf{r}')}{|\mathbf{r}_i - \mathbf{r}'|}d\mathbf{r}' + V_{xc} \tag{2.46}$$

and

$$V_{xc} = \frac{\delta E_{xc}}{\delta\rho} \tag{2.47}$$

V_{xc} is a functional derivative of the exchange-correlation energy with respect to the electron density. It is a one-electron operator for which the expectation value of the KS Slater determinant is E_{xc}. Since the value of $E[\rho(\mathbf{r})]$ being minimized in Eq. 2.42 is exact (assuming the BO approximation and neglecting relativity), then the orbitals corresponding to the minimum energy must form the exact density of the non-fictitious system. Furthermore, these orbitals form the Slater-determinantal eigenfunctions of the separable, non-interacting Hamiltonian of Eq. 2.46.

It is apparent that there are many similarities between DFT and HF theory; however, there is one major difference between the two. DFT is exact (within the approximations used) if the value of E_{xc} as a function of ρ is known. The problem is that the value of E_{xc} is unknown and must be estimated. There are currently several different approximations of the exchange-correlation functional of the electron density, and the discussion of such functionals will be limited to the more popular ones used in this thesis. The types of methods used to approximate the functionals can be separated into three different categories: local density methods, gradient corrected semi-local methods, and hybrid methods including exact exchange.

2.8.1 Local Density Methods

It is customary to separate E_{xc} into two parts, a pure exchange and pure correlation functional. The kinetic energy correction is quite small compared to the other electronic corrections and is typically added implicitly through the adjustment of arbitrary coefficients. Hence, E_{xc} becomes

$$E_{xc}[\rho] = E_x[\rho] + E_c[\rho] = \int \rho(\mathbf{r})\epsilon_x[\rho(\mathbf{r})]d\mathbf{r} + \int \rho(\mathbf{r})\epsilon_c[\rho(\mathbf{r})]d\mathbf{r} \tag{2.48}$$

The functionals ϵ_x and ϵ_c are in terms of energy per particle.

In the Local Density Approximation (LDA), it is assumed that the density can be treated locally as a uniform electron gas and implies that the density is a slowly varying function. The exchange energy for a uniform electron gas was determined by Dirac [39]

$$E_x^{LDA}[\rho] = -C_x \int \rho^{4/3}(\mathbf{r})d\mathbf{r} \tag{2.49}$$

$$\Rightarrow \qquad \epsilon_x^{LDA}[\rho] = -C_x\rho^{1/3}$$

Equation 2.50 holds for any closed-shell system where the number of α and β electrons are equal. For open-shell systems, the Local Spin Density Approximation (LSDA) is used, and the exchange energy can be written as

$$E_x^{LSDA}[\rho] = -2^{1/3}C_x \int [\rho_\alpha^{4/3} + \rho_\beta^{4/3}]d\mathbf{r} \tag{2.50}$$

$$\Rightarrow \qquad \epsilon_x^{LSDA}[\rho] = -2^{1/3}C_x[\rho_\alpha^{1/3} + \rho_\beta^{1/3}]$$

The value of $\epsilon_x^{LSDA}[\rho]$ may also be written in terms of the total density and spin polarization

$$\epsilon_x^{LSDA}[\rho] = -\frac{1}{2}C_x\rho^{1/3}[(1+\zeta)^{4/3} + (1-\zeta)^{4/3}] \tag{2.51}$$

where

$$\zeta = \frac{\rho^\alpha - \rho^\beta}{\rho^\alpha + \rho^\beta}, \qquad \frac{4}{3}\pi r_s^3 = \rho^{-1} \tag{2.52}$$

The term r_s^3 is the effective volume containing one electron.

The correlation energy of a uniform electron gas has been determined from Monte Carlo methods for a number of different densities. Vosko, Wilk, and Nusair [40] were able to use these results to create a suitable analytic interpolation formula which could be used

in DFT. This formula, commonly labeled as VWN, interpolates between the unpolarized ($\zeta = 0$) and spin polarized ($\zeta = 1$) limits and is written as

$$\begin{aligned} \epsilon_c^{VWN}(r_s,\zeta) &= \epsilon_c(r_s,0) + \epsilon_a(r_s)\left[\frac{f(\zeta)}{f''(0)}\right][1-\zeta^4] + [\epsilon_c(r_s,1) - \epsilon_c(r_s,0)]f(\zeta)\zeta^4 \\ f(\zeta) &= \frac{(1+\zeta)^{4/3} + (1-\zeta)^{4/3} - 2}{2(2^{1/3}-1)} \end{aligned} \tag{2.53}$$

$\epsilon_c(r_s,\zeta)$ and $\epsilon_c(r_s)$ functionals are parameterized according to

$$\begin{aligned} \epsilon_{c/a}(x) &= A\left[ln\frac{x^2}{X(x)} + \frac{2b}{Q}tan^{-1}\left(\frac{Q}{2x-b}\right)\right. \\ &\quad \left. -\frac{bx_o}{X(x_o)}\left[ln\frac{(x-x_o)^2}{X(x)} + \frac{2(b+2x_o)}{Q}tan^{-1}\left(\frac{Q}{2x+b}\right)\right]\right] \\ x &= \sqrt{r_s} \\ X(x) &= x^2 + bx + c \\ Q &= \sqrt{4c-b^2} \end{aligned} \tag{2.54}$$

The parameters A, x_o, b, and c are fitting constants and are all different for $\epsilon_c(r_s,0)$, $\epsilon_c(r_s,1)$, and $\epsilon_a(r_s)$.

The LSDA approximation usually underestimates the correlation energy and tends to underestimate bond lengths, which leads to an overestimation of the dissociation energies. The uniform electron gas model fails to describe most molecules in which the electron density does not vary slowly; hence, the accuracy of a LSDA calculation is comparable somewhat to that of a HF calculation. However, the LDA works well for solid state metals.

2.8.2 Gradient Corrected Methods

As mentioned in the previous section, the electron density of most systems cannot be properly modelled as a uniform electron gas. Therefore, improvements over the LSDA approach must consider a non-uniform electron gas. The exchange and correlation energies would not only depend on the electron density, but they would also depend on the gradient of the electron density. Such methods are known as Generalized Gradient Approximations (GGA). Most GGA functionals are constructed with a correction term being added to the LSDA functional.

$$\epsilon_{xc}^{GGA}[\rho(\mathbf{r})] = \epsilon_{xc}^{LSDA}[\rho(\mathbf{r})] + \Delta\epsilon_{xc}\left[\frac{|\nabla\rho(\mathbf{r})|}{\rho^{4/3}(\mathbf{r})}\right] \tag{2.55}$$

There are many different formulae used to calculate the gradient correction term of Eq. 2.55, which will not be detailed here. The GGA exchange functionals used in this thesis were PW91 [41], PBE [42], and B88 [43]. The correlation functionals used were PW91 [41], PBE [44], and LYP [45, 46].

2.8.3 Hybrid Methods

Assume for a moment that the Hamilton operator for any system can be written as a function of a parameter (λ), which describes the extent of interelectronic interactions.

$$\hat{\mathbf{H}}_\lambda = \hat{\mathbf{T}} + \hat{\mathbf{V}}_{ext}(\lambda) + \lambda\hat{\mathbf{V}}_{ee} \tag{2.56}$$

where $0 \leq \lambda \leq 1$. The $\hat{\mathbf{T}}$ term is the kinetic energy operator for each electron. The $\hat{\mathbf{V}}_{ext}(\lambda)$ operator is the external potential operator. The $\lambda = 0$ limit describes a system of non-interacting electrons, and the $\lambda = 1$ limit describes a system with fully interacting electrons. Using the Hellmann-Feynman theorem, one can show that the exchange-correlation energy can be written as

$$E_{xc} = \int_0^1 \langle\Psi_\lambda|\hat{\mathbf{V}}_{xc}(\lambda)|\Psi_\lambda\rangle d\lambda \tag{2.57}$$

Equation 2.57 is known as the Adiabatic Connection Formula [47]. At the $\lambda = 0$ limit, there is no correlation energy, and E_{xc} is equal to the exchange energy (E_x^{HF}). The exact exchange energy can be calculated from a Slater Determinant of HF orbitals. For intermediate values of λ as well as at the $\lambda = 1$ limit, $\hat{\mathbf{V}}_{xc}$ and Ψ_λ are unknown, and the exchange-correlation energy is parameterized such that these values are added as an exchange-correlation parameter of either GGA or LDA to E_x^{HF}. Thus, the value of E_{xc} from Eq. 2.57 would be

$$E_{xc} = (1-a)E_{xc}^{DFT} + aE_x^{HF} \tag{2.58}$$

where a is a constant that is optimized from experiments. The first term on the right hand side of Eq. 2.58 can be further split up and parameterized to include a variety of different methods (GGA, LDA, or both) to estimate the correlation and exchange energies. In this thesis, the B3LYP [40, 45, 48, 49] hybrid functional was used. Within this model, E_{xc} is defined as

$$E_{xc}^{B3LYP} = (1-a)E_x^{LSDA} + aE_x^{HF} + b\Delta E_x^B + (1-c)E_c^{LSDA} + cE_c^{LYP} \tag{2.59}$$

a, b, and c are all fitted constants and are equal to 0.20, 0.72, and 0.81, respectively.

2.8.4 Broken Symmetry DFT

Molecular systems such as organic radicals or weakly interacting transition metal complexes cannot be properly described by a single SD. The application of DFT or any other single determinant ab-initio method will be both technically and conceptually problematic.

Spin unrestricted Kohn-Sham (UKS) equations are similar to the UHF method proposed by Pople and Nesbet [50] and by Berthier [51]. Applications of UHF encountered certain problems related to spin contamination arising from the fact that the UHF wavefunction is not an eigenfunction of $\langle S^2 \rangle$. Advanced wavefunction methods such as MCSCF, CI, and CASSCF can accurately calculate properties of multireference systems with the correct $\langle S^2 \rangle$ but are computationally intensive. Density functional methods do not suffer from the same problems as advanced wavefunction methods because electron correlation is implicitly included within the exchange-correlation functional. However, possible artifacts can arise within spin unrestricted DFT because the real system of interacting electrons possesses well-defined spin symmetries, and the UKS noninteracting reference system does not.

Radicals and open shell systems with high spin ground states can be described reasonably well with the UKS approach. However, problems remain if the system of interest exhibits a low spin ground state of broken symmetry between ρ_α and ρ_β, or when the property of interest concerns energy differences among high and low spin states. These types of systems include biradicals and a broad range of polynuclear complexes with open shell transition metal atoms. A practical solution would be to use a restricted Kohn-Sham approach, as this would provide the correct spin symmetry for the non-interacting reference system. It has been shown, however, that the RKS approach leads to unusually high energies for the low spin states. Covalent bonding among transition metal centers in anti-ferromagnetically coupled systems is overestimated, and metal-metal bonds are too short [52]. If the symmetry constraints for the spin are lifted within a UKS approach, then the resulting KS wavefunction can minimize to a broken symmetry solution. These solutions allow for the localization of spin density on two or more weakly interacting atoms within a molecule. For example, the broken symmetry solution for a singlet state of an anti-ferromagnetically coupled transition metal dimer is described as having an excess of α spin localized on one metal atom with a concomitant amount of excess β spin on the other metal atom [53]. This type of system would be described as an equal mixture of

the low and high spin states, and within a UHF approach, the wavefunction would have significant spin contamination. The value of $\langle S^2 \rangle$ for a singlet state typically resembles that of an average between the high spin and low spin values. Though broken symmetry solutions to the KS equations are founded upon the flaws of estimating the exchange-correlation functional, they have provided reasonable geometries and trends for weakly interacting, anti-ferromagnetically coupled systems [52, 54, 55].

The broken symmetry approaches provide a way to bypass the problem of dealing with low spin states in UKS calculations; however, the problem still remains that the real system must possess spin symmetry. Broken symmetry DFT also tends to overstabilize low spin states and cannot accurately reproduce magnetic coupling constants for many systems. The use of broken symmetry UKS theory is currently an active area of research, and several computational techniques have been created to deal with the shortcomings of this theory [53, 56–61].

2.9 Basis Set Superposition Errors

Basis sets are usually centered on the nuclei. Since complete basis sets cannot be used in practice, the N^4 or higher scaling of computational time with respect to N basis functions limits the number of basis functions that can be used to hundreds or a few thousand at best. The mean absolute error associated with basis set incompleteness can be quite large and on the order of several hartree; however, the primary goal of most ab-initio calculations is to compare relative energies. It is therefore necessary to make the error as constant as possible.

Fixing the position of the basis functions at the nuclei allows for a compact basis set, otherwise sets of basis functions centered at many different points in geometrical space would be needed. Comparing the energies of molecules with a different geometry using a nuclei-fixed basis set introduces an error. The quality of the basis set is not the same at all geometries because the electron density around one nucleus may be described by functions centered at another nucleus. This error can become significant when describing small effects, such as van der Waals interactions or hydrogen bonding. For example, consider two molecules A and B interacting to form the complex AB. The simplest approach to calculating the complexation energy would be to subtract the energies of the isolated species A and B from the complex AB (assuming a size extensive method). Assuming weak

interactions between A and B, then the electron distributions for A and B in the complex AB would be similar to those of the isolated species. In the complex, however, basis functions from A can compensate for some of the basis set incompleteness in B and vice-versa. The complexation energy will therefore be artificially lowered and the interactions between A and B overestimated. This effect is known as the Basis Set Superposition Error (BSSE). In the limit of a complete basis set, the BSSE will be zero, and the addition of basis functions will not give any improvement. The simplest approach to eliminating the BSSE is to add more basis functions until the complexation energy no longer changes. Unfortunately, this requires large basis sets and can only be achieved for small systems. Therefore, when determining complexation energies for weakly bound systems, a balance must be made between computational cost and BSSE when selecting basis sets.

An approximate way of assessing the BSSE is the Counterpoise (CP) correction [62,63]. In this method, the BSSE is estimated as the difference between the monomer energies with the regular basis sets and the energies calculated with the full set of basis functions for the complex. Consider again molecules A and B with nuclear-centered basis functions denoted by subscripts a and b, and the complex AB having the combined basis functions ab. The geometries of the two isolated molecules are first optimized. The geometries of the A and B molecules within the complex will usually be slightly different from the isolated species, and the complex geometry will be denoted by a *. The complexation energy can be calculated by

$$\Delta E_{complexation} = E(AB)^*_{ab} - E(A)_a - E(B)_b \tag{2.60}$$

To estimate how much of this complexation energy is due to the BSSE, four additional energy calculations need to be performed. The energies of fragments A and B need to be calculated with the geometries they have within the complex. Two additional energy calculations of the fragments with the complex geometry are carried out with the full set of basis functions ab. For example, the energy of A is calculated in the presence of both the normal (a) basis functions and the (b) basis functions of fragment B centered at the corresponding nuclear positions, but the B nuclei are not present. Such basis functions located at fixed points in space without nuclei are referred to as ghost orbitals. The energy of fragment A will be lowered due to the presence of these ghost orbitals. The CP energy correction is therefore defined as

$$\Delta E_{cp} = E(A)^*_{ab} + E(B)^*_{ab} - E(A)^*_a - E(B)^*_b \tag{2.61}$$

The counterpoise corrected complexation energy is given as $\Delta E_{complexation} - \Delta E_{cp}$. If the counterpoise energy correction is significant compared to the complexation energy, then a re-evaluation of the basis sets needs to be done. As basis sets are often at HF-limit quality, the largest BSSE comes from electron correlation.

2.10 The Pseudopotential Approximation

The treatment of atoms and molecules with a large number of electrons from HF or DFT techniques is still a challenge to quantum chemists due to the fact that computational time scales as N^m with N being the number of basis functions. The increase in CPU power and the development of sophisticated algorithms over the last few decades has made it possible to calculate properties of lighter atoms and molecules with results at or near experimental accuracy. However, further approximations without significant loss of accuracy are needed for heavy or large molecules, as an all-electron treatment for these types of systems is still computationally time consuming. Such an approximation is called the pseudopotential approximation (PPA) or effective core potential (ECP) method originally introduced by H. Hellmann [64] as the combined approximation method [65]. In the PPA, the electrons are separated into core and valence spaces and applies to the basic idea that the valence electrons are primarily responsible for chemical bonding and processes. The PPA is introduced into the electronic Hamiltonian by [66]:

$$\hat{H}_v = -\frac{1}{2}\sum_{i}^{n_v}\nabla_i^2 + \sum_{i<j}^{n_v}\frac{1}{r_{ij}} + \sum_{i}^{n_v}\sum_{a}^{N_c}\left[V_{PP}^a(r_{ai}) - \frac{Q_a}{r_{ai}}\right] + \sum_{a<b}^{N_c}\frac{Q_aQ_b}{r_{ab}} \tag{2.62}$$

$\hat{H}_v$ is the valence electron model Hamiltonian with n_v valence electrons and N_c cores (nuclei), and V_{PP} is the corresponding pseudopotential for core-valence interactions. The indices a and b run over all cores (nuclei) and i, j run over all valence electrons. Q_a is the charge of core a and is equivalent to $Z_a - N_c^a$, N_c^a being the number of core electrons of atom a. For an all-electron treatment of a specific atom, $Q_a = Z_a$. The last term in Eq. 2.62 describes the Coulombic core-core repulsion. Additional corrections are needed if one goes beyond the frozen-core approximation.

Non-relativistic quantum chemical calculations on heavy atoms fail to reproduce an accurate treatment of basic properties such as ionization potentials, electron affinities, excitation energies, and static dipole polarizabilities; hence relativistic effects for these

systems cannot be neglected. Even though relativistic basis sets [67–70] as well as Dirac-Hartree-Fock (DHF) coupled cluster calculations including Breit interactions for many-electron heavy atomic systems are now available, a fully relativistic treatment for heavy elements is still a formidable task. There are two main approaches toward the treatment of large molecules with heavy elements. One of these methods is relativistic density dunctional theory (RDFT) [71] in which relativistic Hamiltonians are introduced into a DFT scheme. Current RDFT schemes suffer from the fact that they cannot be improved to high accuracy to describe certain interactions (for example Van der Waals) even with the development of more accurate functionals within the GGA [72].

The other alternative is to stay with relativistic ab-initio calculations and reduce the number of electrons in the Hamiltonian. Since the core electrons are not as important in describing most chemical properties as the valence electrons, one might consider a frozen core approximation and apply the PPA model to approach heavy elements. Such an approach is not trivial, as several fundamental issues need to be addressed before a PPA model is adopted. One concern with the PPA is that the electrons cannot be separated into core and valence electrons, as this violates the Pauli principle. Transferability among different molecules as well as fitting techniques for different pseudopotentials are of further concern. Relativistic perturbation operators act in the close vicinity of the nucleus, and it is not obvious how a relativistic scheme can be implemented into the PPA using nodeless orbitals. Lastly, core properties such as electric field gradients and magnetic shielding tensors cannot be obtained directly from pseudopotential schemes.

Given that there are several concerns associated with using a PPA description for heavy atoms, there are many advantages for using such an approximation. Atomic and molecular properties for elements with large relativistic effects have been calculated very accurately using the PPA. Removing the core and replacing them with nodeless pseudoorbitals significantly reduces the number of basis functions for an atomic or molecular calculation. The amount of the BSSE is reduced for weakly interacting systems. Relativistic effects can be included implicitly in the pseudopotential through the adjustment procedure to relativistic atomic calculations. This eliminates the need to carry out a fully relativistic treatment for molecules containing heavy elements.

2.10.1 Introducing Pseudopotentials into the Hartree-Fock Equations

Before introducing the PPA into the HF equations, appropriate core and valence spaces must be chosen. This task is not trivial, and several properties must be considered before selecting these corresponding spaces. First, the core should be chosen within a region where there is little overlap between the core and valence spaces. This can be achieved by comparing the outermost core orbital with the innermost valence orbital through the examination of orbital energies, overlap regions, r-expectation values, etc. Next, the static dipole polarizability of the core should be small. This defines a hard core where polarization effects from other electrons and nuclei are relatively small. The core density should not change significantly with the addition or removal of valence electrons. The valence electrons from other atoms should not penetrate into the core. Core penetration causes large errors associated with overlap between cores of different atoms. Given the above criteria, core spaces are typically chosen to be closed shell and contain the innermost s, p, d, or f orbitals.

For a neutral atom with N_c core electrons and $n_v = Z - N_c$ valence electrons, the Hartree-Fock core and valence electron densities can be written as:

$$\rho_c(\mathbf{r}) = \sum_{c \in core} N_c |\phi_c(\mathbf{r})|^2 \tag{2.63}$$

$$\rho_v(\mathbf{r}) = \sum_{v \in valence} n_v |\phi_v(\mathbf{r})|^2 \tag{2.64}$$

The HF equation for the valence electrons would be

$$\hat{F}\phi_v = \epsilon_v \phi_v \tag{2.65}$$
$$\langle \phi_v | \phi_c \rangle = 0$$

For simplicity it is assumed that the valence space consists of a single electron, and the core space is closed-shell. An extension into systems with many electrons within the valence space is given in Ref. [73]. If a new valence orbital (χ_v) is created by mixing in core orbitals, then we have:

$$\chi_v = \phi_v + \sum_c a_{cv}\phi_c \tag{2.66}$$
$$a_{cv} = \langle \phi_c | \chi_v \rangle$$

we obtain

$$\langle\chi_v|\hat{F}|\chi_v\rangle = \epsilon_v + \sum_c a_{cv}^2\epsilon_c \tag{2.67}$$

The linear combination in Eq. 2.67 can be chosen such that the radial part of χ_v becomes nodeless in the region $(0,\infty)$, which is called the pseudoorbital transformation. The aim is to construct a new Fock operator such that

$$\hat{F}'\chi_x = \epsilon_v\chi_v \tag{2.68}$$

where ϵ_v is identical to that in Eq. 2.66. The HF equation for χ_v thus becomes

$$\begin{aligned}
\hat{F}\chi_v &= \epsilon_v\phi_v + \sum_c a_{cv}\epsilon_c\phi_c \\
&= \epsilon_v\chi_v + \epsilon_v(\phi_v - \chi_v) + \sum_c a_{cv}\epsilon_c\phi_c \\
&= \epsilon_v\chi_v + \sum_c a_{cv}(\epsilon_c - \epsilon_v)\phi_c \\
&= \epsilon_v\chi_v + \sum_c \langle\chi_v|\phi_c\rangle(\epsilon_c - \epsilon_v)\phi_c
\end{aligned} \tag{2.69}$$

The last term in Eq. 2.69 can be brought to the left hand side and after inserting Eq. 2.67 for the coefficients a_{cv} we obtain

$$[\hat{F} + \hat{P}_{core}]\chi_v = \hat{F}_{PK}\chi_v = \epsilon_v\chi_v \tag{2.70}$$

where $\hat{F}_{PK}$ stands for the Philips-Kleinman operator. $\hat{P}_{core}$ is a specific core projection operator such that

$$\hat{P}_{core} = \sum_c (\epsilon_v - \epsilon_c)|\phi_c\rangle\langle\phi_c| \tag{2.71}$$

The Fock operator can now be split into a sum of valence and core operators, with the core operator being absorbed into pseudopotential operator ($\hat{V}_{pp}(\mathbf{r})$) for the valence electron at position $\mathbf{r}$. Hence, the total Fock operator becomes

$$\hat{F} = \hat{F}_{valence} + \hat{V}_{pp}(\mathbf{r}) = \hat{F}_{valence} - \frac{N_c}{r} + \sum_c (2\hat{J}_c - \hat{K}_c) + \hat{P}_{core} \tag{2.72}$$

Solving the HF equations for χ_v leads to

$$\frac{\langle\chi_v|\hat{F}_{valence} + \hat{V}_{pp}|\chi_v\rangle}{\langle\chi_v|\chi_v\rangle} = \langle\phi_v|\hat{F}_{valence} + \hat{V}_{pp}|\phi_v\rangle = \langle\phi_c|\hat{F}_{valence} + \hat{V}_{pp}|\phi_c\rangle = \epsilon_v \tag{2.73}$$

Equation 2.72 is considered the starting point for all pseudopotential approximations in which $\hat{V}_{pp}$ can take on a variety of different forms within different PPA schemes. There are two major types of pseudopotentials, which will be discussed briefly below: *Energy consistent pseudopotentials* and *Shape consistent pseudopotentials*.

Within the pseudopotential approximation, $\hat{V}_{pp}$ is replaced by a local or non-local potential which is bound from below by a linear combination of Gaussian type orbitals (GTO's). One therefore chooses l-dependent semi-local pseudopotentials of the form [74–77]

$$\begin{aligned}\hat{V}_{pp} &= \hat{V}_{pp}^{local}(\mathbf{r}) + \sum_{l=0}^{L_{max}} \hat{V}_{pp}^{l}(\mathbf{r}) \sum_{m=-l}^{l} |lm\rangle\langle lm| \\ &= \sum_{n=1}^{N_L} A_n r^{k_n} e^{-\alpha_n r^2} + \sum_{l=0}^{L_{max}} \sum_{n=1}^{N_{SL}} B_{ln} r^{k_{ln}} e^{-\beta_{ln} r^2} \sum_{m=-l}^{l} |lm\rangle\langle lm| \end{aligned} \tag{2.74}$$

where the sum over the m term is an l-dependent operator projecting onto the Hilbert subspace of angular momentum l, and k is an integer with a value $k \geq -2$.

Energy consistent pseudopotentials (EC-PP or EC-ECP) are fitted such that the pseudopotential parameters A_n, α_n, B_{ln}, and β_{ln} in Eq. 2.74 are adjusted to an atomic valence spectrum by a least squares fit procedure.

$$\sum_i w_i (\Delta E_i^{AE} - \Delta E_i^{PP})^2 = min. \tag{2.75}$$

where w_i are weight factors, and ΔE_i^{AE} are ionization potentials, electron affinities, and excitation energies for neutral or charged atoms. These reference data are obtained from numerical HF calculations [78].

The same parameters described above in Eq. 2.74 can also be adjusted such that the valence orbitals are reproduced to high accuracy above a certain cut-off radius (R_c). This fitting process can be done by modifying all-electron orbitals such that they are nodeless in the core region below R_c and adjusting the pseudopotential parameters such that they match these orbitals [79–81]. These pseudopotentials are called shape consistent pseudopotentials (SC-PP or SC-ECP). The primary drawback to this procedure is that a large number of Gaussians are required to obtain an accurate fit.

As mentioned previously, relativistic operators act in the vicinity of the nucleus. Parameterization of the pseudopotentials to relativistic data therefore seems to successfully transfer both direct and indirect relativistic effects to the valence orbitals. The parameterization procedure for modeling these effects into the PPA can come from a variety

of different data. Reference energies or orbitals can be taken from scalar relativistic, spin-orbit coupled, or fully relativistic all-electron calculations. The PPA can be introduced at the scalar (spin-orbit averaged) relativistic level (SRPP, ARPP, or AREP), at the two-component level (SOPP or REP), or derived from the 4-component Dirac equation [82–85].

2.11 Gas-phase Electron Diffraction

When a beam of electrons hits a set of randomly oriented molecules in the gas-phase, the electrons are diffracted by the charge distribution of these molecules. The resulting defraction pattern contains a large amount of information about the system, such as internuclear distances, relative isomer conformations, vibrational information, and the relative composition [86]. These molecules can be considered "free" molecules, i.e. free from intermolecular effects, as the diffraction chamber is kept at very low (typically between 10^{-5}–10^{-6} torr) pressures.

The apparatus for a typical ED experiment is shown in Figure 2.1. The source of electrons comes from the electron gun, which consists of a tungsten filament that releases a beam of electrons when heated. The electrons are accelerated toward an anode at a potential of 40–50 kV. A magnetic lens is used to focus the electron beam to a diameter between 0.1–0.2 mm before it enters the diffraction chamber. The diffraction chamber itself is kept at a low pressure through the use of a diffusion pump. The molecular beam is introduced into the diffraction chamber through the nozzle, which has a diameter of roughly 0.3 mm. To obtain reasonably high values of the scattering intensities, the pressure of the molecular beam should be between 10–20 torr. To avoid ruining the vacuum in the diffraction chamber, the molecular beam is collected in a cold trap. A rotating sector is used to reduce the exposure of the detector (photographic plate) at low scattering angles. Lastly, a beam-stop is used to prevent the primary beam from reaching the detector. The diffraction pattern is usually collected at two and sometimes three different distances from the diffraction center. This makes it possible to cover a larger range of scattering angles than would be covered at a single distance.

A vast majority of the gas-phase ED studies employ the independent-atom model, which states that the atoms within a molecule can be considered as spherically symmetric, independent diffraction centers. This model can be applied to a gas consisting of rigid,

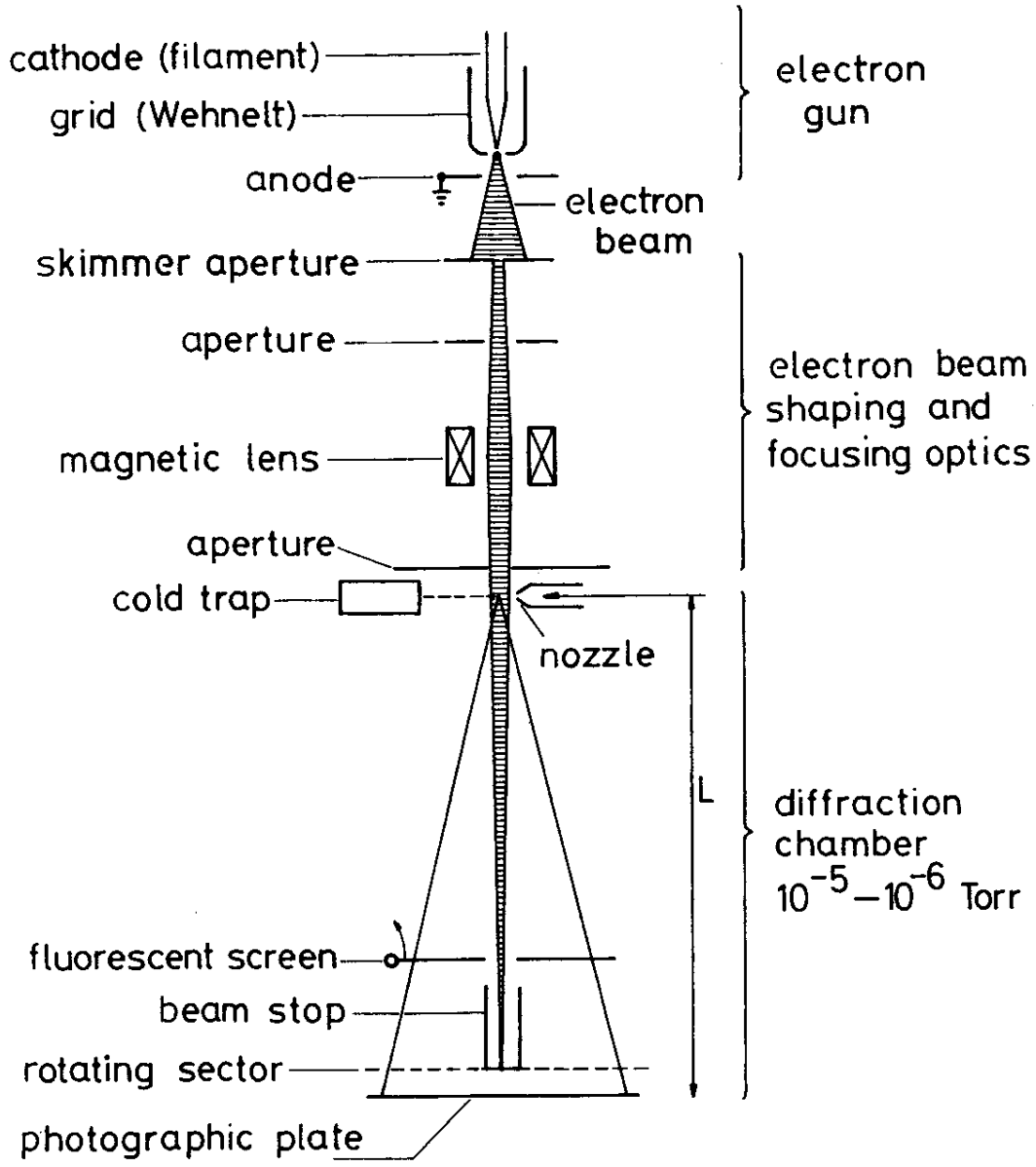

Figure 2.1: Scheme of an apparatus for gas-phase electron diffraction (from Ref. [86]).

non-vibrating molecules, and to that of a gas containing vibrating molecules. Given a set of randomly oriented rigid molecules, the intensity of elastically scattered electrons can be calculated by:

$$I(s) = KI_oR^{-2}\sum_{i=1}^{N}\sum_{j=1}^{N} f_i(s)f_j^*(s)\frac{\sin sr_{ij}}{sr_{ij}} \tag{2.76}$$

where I_o is the intensity of the incident electron beam, R is the distance between the

observation point and the scattering center, K is a constant that can be expressed in terms of fundamental constants, N is the number of atoms in the molecule, $f_i(s)$ and $f_j(s)$ are the scattering amplitudes of the i-th and j-th atoms, respectively, r_{ij} is the internuclear distance, and the variable s is defined as $s = (4\pi/\lambda)\sin(\theta/2)$ (where λ is the wavelength of the electron beam and θ is the scattering angle).

Although the molecules are randomly oriented, the diffracted electrons can interfere with one another depending on internuclear distances. Hence, the diffracted intensity can be split into an atomic contribution, $I_a(s)$, which contains no structural information, and a molecular contribution, $I_m(s)$, which contains all of the structural information.

$$I(s) = I_a(s) + I_m(s) = KI_oR^{-2}\sum_{i=1}^{N}|f_i(s)|^2 + KI_oR^{-2}\sum_{i=1}^{N}\sum_{j\neq i}^{N} f_i(s)f_j^*(s)\frac{\sin sr_{ij}}{sr_{ij}} \quad (2.77)$$

In addition to elastic scattering, inelastic scattering needs to be considered. While elastic scattering is found for a wide range of scattering angles, inelastic scattering is primarily found at small scattering angles. Assuming that the inelastic scattering is incoherent, we obtain the following equation:

$$I_t(s) = I_i(s) + I_a(s) + I_m(s) = I_b(s) + I_m(s) \quad (2.78)$$

where $I_t(s)$ is the total diffracted intensity, and $I_b(s)$ represents the background intensity.

The atomic scattering amplitudes, $f_i(s)$, can be introduced at different levels of approximation. In the quasi-kinematic approximation, the incident electron wave undergoes a significant phase shift as it propagates through an atomic field. The phase shift increases with increasing atomic number and scattering angle. Taking into account these considerations, the atomic scattering amplitudes take the form:

$$f_i(s) = |f_i(s)|e^{i\eta_i(s)} \quad (2.79)$$

where $|f_i(s)|$ is the modulus of the amplitude, and $\eta_i(s)$ is the phase angle in radians. If these complex scattering angles are used in the determination of the molecular intensity, we get:

$$I_m(s) = KI_oR^{-2}\sum_{i=1}^{N}\sum_{j\neq i}^{N} g_{ij}(s)\frac{\sin sr_{ij}}{sr_{ij}} \quad (2.80)$$

where

$$g_{ij}(s) = |f_i(s)||f_j(s)|\cos[\eta_i(s) - \eta_j(s)] \quad (2.81)$$

Treating molecules as rigid and non-vibrating is usually a poor approximation. This is especially true for nonvolatile systems in which high temperatures are required to vaporize the sample. Molecules with low frequency, large amplitude vibrations are also poorly described by such an approximation. If the vibrational motions are assumed to be harmonic, then the following equation for the molecular intensity is obtained:

$$I_m(s) = KI_oR^{-2}\sum_{i=1}^{N}\sum_{j\neq i}^{N} g_{ij}(s)\exp(-l_{ij}^2 s^2/2)\frac{\sin sr_{ij}}{sr_{ij}} \tag{2.82}$$

Here l_{ij} is the mean vibrational amplitude along the line connecting the two nuclei, and r_{ij} is now an effective nuclear distance, denoted as r_a, which can be approximated by relating it to the vibrationally averaged internuclear distance at the temperature of the ED experiment, r_g, by the following equation:

$$r_a \approx r_g - \frac{l^2}{r_a} \tag{2.83}$$

If the vibrations are anharmonic, then the $\sin(sr_{ij})$ term is replaced by $\sin[s(r_{ij}-\kappa_{ij}s^2)]$ where κ_{ij} is an asymmetry factor related to the a constant in the Morse equation and can be determined from the ED experiment.

Structural analysis of an ED experiment requires two basic steps. The first being the choice of a molecular model. The second step involves the refinement of the model and comparing the theoretical and experimental intensities. The molecular model usually comes from the results of quantum chemical calculations. If the model is not known in advance, then geometrical information can be found from the radial distribution function, and models are tested from trial-and-error until a satisfactory one is found.

The starting model is usually refined by the least-squares method, minimizing the sum of the weighted squares of the differences between the experimental molecular intensities, $I_m^E(s) = I_t^E(s) - I_b^E(s)$, and the corresponding theoretical values calculated from Eq. 2.82, $I_m^T(s)$. The least squares method is applied iteratively until convergence is reached. Careful attention must be paid to the converged structure, as several different minima can exist in the least-squares refinement. The converged structure should be chemically reasonable; to further aid in convergence, the starting parameters should not deviate significantly from their experimental values. Often the molecular intensities are not used, rather they are

modified into the following forms:

$$sM^E(s) = \frac{s[I_t^E(s) - I_b^E(s)]}{I_b^E(s)} \quad (2.84)$$

$$sM^T(s) = \frac{sI_m^T(s)}{I_a^T(s)} \quad (2.85)$$

The background term, $I_b^E(s)$, can be determined by hand-tracing a smooth curve through the oscillations of the total experimental intensities, or for more difficult systems, it can be determined by fitting a high-order polynomial through the oscillations. The curve is adjusted repeatedly through the analysis. These adjustments should not effect the geometrical parameters, and only the least-squares standard deviations should be effected by the changes.

There are several different quantities that can be determined and/or adjusted during the least-squares refinement. Some of them are real molecular parameters, and others refer to the conditions of the experiment:

1. Geometrical parameters and bond length differences.
2. Mean amplitudes of vibration, l_{ij}, for bonded and non-bonded distances.
3. Asymmetry parameters, κ_{ij}, and shrinkage parameters, δ_{ij}.
4. Conformer populations.
5. Gas-phase composition of systems with different oligomers.
6. Coefficients of the polynomials used to fit the background curve.

The structural analysis of an ED experiment is not a straightforward procedure. Two or more different parameters may couple with one another, producing several different possibilities for molecular structures. This process is even more complicated for systems containing different oligomers, as several differences in bond lengths and angles may couple with each other.

2.12 Computational Details

To determine all possible low-energy structures, we performed geometry optimizations using symmetry-broken unrestricted Kohn-Sham density functional theory (BS-DFT) [41]

with the PW91 functional, the Los-Alamos pseudopotentials, and corresponding valence double-zeta basis sets (LanL2DZ) [79, 87] for Cr and the halides (F, Cl, Br, I). These preliminary calculations were carried out for a large variety of possible three dimensional structures with chromium in different coordination and spin states. All minima that yielded energies within a window of 1 eV from the global minimum were considered for further refinement. To determine an accurate DFT method to use for the intensive analysis of the chromium dihalide oligomers, the results of different local (LSDA), GGA (PW91 and PBE), and hybrid (B3LYP) DFT geometry optimizations on the monomer were compared with available literature data as well as from our UHF, MP2, CCSD(T), CASSCF, and CASPT2 calculations. After comparing our DFT results on the chromium dihalide monomers with the literature data, it was determined that B3LYP best represented the CrF_2 and $CrCl_2$ molecules and PW91 best represented the structures for $CrBr_2$ and CrI_2. Using the geometries from the PW91/LanL2DZ geometry optimizations of the oligomers as a starting point, we carried out geometry optimizations for the chromium dihalides using the methods mentioned above. Here we used a modified energy-consistent Stuttgart scalar relativistic small-core pseudopotential and corresponding valence basis set with a [8s8p7d18f]/(7s7p5d3f) contraction scheme for Cr [88]. An aug-cc-pVDZ basis set was used for F and Cl [89–91]. The basis sets for Br and I consisted of an energy-consistent Stuttgart scalar relativistic small-core pseudopotential and corresponding augmented double-zeta valence basis set with a [9s8p8d]/(5s4p3d) contraction scheme for Br and a [9s7p7d]/(5s4p3d) contraction scheme for I [92]. For $CrCl_2$, we also used the B3PW91 functional together with the Stuttgart pseudopotential for Cr and a cc-pVTZ basis set for Cl to obtain a second set of bond distances and angles for the electron diffraction analysis. All of the geometry optimizations were performed using the Gaussian03 software package [93]. The Cartesian coordinates of the lowest energy structures we calculated from our preliminary and intensive geometry optimizations as well as the modified basis sets used for Cr, Br, and I are given in the Appendix.

A different refinement scheme was used for the intensive tetramer analysis. All of the high-spin (septendecet) structures were optimized with the B3LYP or PW91 functionals, and their energies were compared. If a structure was above 0.5 eV from the lowest energy septendecet structure, the low-spin (nonet and singlet) states were not examined. This scheme was used because the high-spin states were significantly easier to obtain SCF and geometry convergence than the low-spin states; hence, the number of low-spin structures

that needed to be analyzed was kept to a minimum. The energy of the lowest lying septendecet structure was always close to that of the global minima and smaller than 0.5 eV.

Harmonic vibrational frequencies were calculated analytically, if possible. These frequencies were used to calculate the zero-point vibrational energy correction, the enthalpy and Gibbs free energies of atomization from 1000–2000 K and 1 atm. of pressure. The vibrational analysis was also carried out to obtain the force constants in cartesian coordinates, which was needed for the normal coordinate analysis of $CrCl_2$.

Basis set superposition errors (BSSE) for the clusters were calculated using the counterpoise correction by Boys and Bernardi [62, 63], but including two-body terms between CrX_2 fragments only.

Because of the open-shell nature of the chromium dihalides' electronic structures, we also performed complete active space self-consistent field calculations, CASSCF, followed by second-order perturbation theory, CASPT2, for both the monomer and dimer species, as well as full-space coupled cluster calculations (CCSD(T)) for the monomer. Initial guesses of the wavefunctions were obtained from restricted open-shell Hartree-Fock calculations. For the low lying $^5B_2$, $^5\Sigma_g^+$, $^5\Pi_g$, and $^5\Delta_g$ states of the monomer, we applied CASSCF(16,15), which denotes 16 electrons distributed over 15 orbitals. This active space consisted of the five $3d$ metal orbitals on Cr (δ_g, π_g, σ_g) along with the valence p orbitals from both halides. Also included within the active space were virtual orbitals consisting of σ_g and σ_u symmetry and a pair of π_u orbitals. The geometry was kept at the optimized B3LYP or PW91 structures, as these calculations were quite computer time consuming. For the CASPT2 calculation, we had to reduce the active space to (4,5) for the $^5B_2$, $^5\Sigma_g^+$, $^5\Pi_g$, $^5\Delta_g$, $^3\Sigma_g^-$, and $^1\Sigma_g^+$ states, which distributes 4 electrons in the metal $3d$ orbitals. Here we were able to carry out a geometry optimization. For the dimers, we used the same active space as for the monomers, which results in a CASSCF(8,10) of the ten $3d$ metal orbitals on the Cr atoms. Only the singlet and nonet states of the dimer were examined, as these calculations became again prohibitively expensive, and the geometry was also fixed to that obtained from the B3LYP or PW91 intensive calculations. For the $^5\Pi_g$ and $^5\Delta_g$ states, a state-averaged CASSCF calculation had to be performed to correctly describe the multireference character in these states. All multireference calculations were performed using the program system Molpro [94].

2.13 Solid-state Calculations

The ground state properties of α-$CrCl_2$ were calculated using DFT in conjunction with a plane wave basis set as implemented in the Vienna *Ab initio* Simulation Package [95]. Electron-electron interactions were modeled using the LSDA [37, 96] or the GGA by Perdew et al. [41] (PW91) of the exchange-correlation energy. The electron-ion interactions were modeled using the projector augmented wave (PAW) method [97, 98] with a cutoff of 450 eV in the expansion of the electronic wavefunction. Brillouin zone (BZ) integrations were done on a regular mesh in reciprocal space, equivalent to 128 k-points in the BZ of the primitive α-$CrCl_2$ unit cell. Geometry optimizations were carried out by first optimizing the cell lattice vectors and all internal coordinates for a number of different cell volumes, using either a conjugate-gradient or quasi-Newton algorithm to minimize the Hellmann-Feynman forces. We considered the structures to be in equilibrium if the Cartesian force vectors of the atomic forces were below 5 meV $Å^{-1}$. The resulting $E(V)$ curve was fitted with a Vinet equation of state (EOS) [99], and the cell parameters and internal structure were optimized at the equilibrium cell volume $V_\circ$.

To calculate the anti-ferromagnetically coupled infinite chain of $CrCl_2$, we performed DFT calculations with the PW91 functional employing the PAW method with a plane wave basis set as implemented in the Vienna *Ab-initio* Simulation Package. Using a supercell approach, neighboring chains were separated by at least 25 Å. Along the chain direction, two irreducible k-points were found to suffice to sample the Brillouin zone.

2.14 Electron Diffraction Analysis

We reanalyzed the earlier electron diffraction experimental data on $CrCl_2$ [3]. We did not feel comfortable with the conclusions of that publication after learning that the vapors of chromium dichloride might have contained trimeric species as well besides the monomers and dimers that were taken into account in that analysis [2]. Therefore, taking into consideration the computed structures of the dimer and trimer, we introduced certain constraints into the electron diffraction analysis about the bond length differences of these species and the monomer. Similarly, we also accepted some of the bond lengths of the oligomers from computation, in order to decrease the number of refineable parameters in the ED analysis.

2.14.1 Experimental Details

A sample of $CrCl_2$ was provided by Professor Herald Schäfer from the University of Münster [100]. $CrCl_2$ is a rather involatile solid; hence, high-temperature experimental conditions were needed for the ED analysis. The diffractometer used was the 'Budapest Apparatus' [101, 102] with a high-temperature molybdenum nozzle used to inject the sample [103] into the diffraction chamber. The nozzle temperature was set to 1170±50 K. Because the $CrCl_2$ vapor may be complex, the combined electron diffraction/quadrupole mass spectrometric technique was utilized [102,104]. The wavelength of the electron beam was 0.04911 Å, and the two nozzle-to-plate distances were 189.29 mm and 497.66 mm. The ranges of intensity data used at 50 cm and 19 cm were $2.00 \leq s \leq 14.00$ Å^{-1} and $9.25 \leq s \leq 29.00$ Å^{-1} ($s = 4\pi\lambda^{-1}\sin\frac{1}{2}\theta$, where λ is the electron wavelength and θ is the scattering angle), respectively. The data intervals were $\Delta s = 0.125$ and 0.250 Å^{-1}, respectively.

2.14.2 Least-Squares Refinement

We first needed the mean amplitudes of vibration from our monomer, dimer, and trimer global minima before any least-squares treatment of our system began. To accomplish this, we first performed harmonic vibrational calculations on the global minima to obtain the Hessian in Cartesian coordinates. This force-field along with the respective atomic motions were used to carry out a normal coordinate analysis and calculate the mean amplitudes of vibration through the use of the ASYM20 software package [105].

The least-squares method was applied to the molecular intensities in the form of the corresponding equation:

$$sM(s) = \sum_i \sum_{j \neq i} \frac{|f_i(s)||f_j(s)|}{B(s)} \cos[\eta_i(s) - \eta_j(s)] \exp(-\frac{1}{2} l_{ij}^2 s^2) \sin[s(r_{ij} - \kappa_{ij} s^2)] \quad (2.86)$$

where $|f(s)|$ and $\eta(s)$ are the absolute values and phases of the complex electron scattering angles [106,107], r_{ij} are the internuclear distances, l_{ij} and κ_{ij} are the corresponding mean amplitudes of vibration and asymmetry constants, and $B(s)$ is the background scattering. The least-squares refinement was done through the use of a modified version of the KCED software package [108].

Our strategy for the least-squares treatment was the following: we accepted as constraints, at least at the initial stages of the refinement, all the differences of the different

cluster bond lengths from that of the monomer. It is well known that the physical meaning of bond lengths coming from different techniques is different [109] and simply taking over bond lengths from the computation (equilibrium bond length, r_e^M) to the analysis of electron diffraction data (where we determine thermal average bond lengths, r_g) would be erroneous. However, taking the *differences* of bond lengths approximately cancels the difference between their physical meaning, and therefore, their use as constraints is an accepted procedure. The stretching vibrations of metal halides are usually anharmonic, and this influences the molecular intensities. The so-called asymmetry parameter, κ, describing the stretching anharmonicity, can usually be refined. However, with so many closely spaced bond lengths this was impossible; therefore, we assumed the asymmetry parameter based on other transition metal dihalides [110].

Furthermore, we also accepted the bond angles of the dimer and trimer from the computation. We also carried out normal coordinate analyses based on the computed frequencies and force fields of all three species, in order to calculate vibrational amplitudes. These amplitudes were used as starting parameters, and many of them were later refined during the analysis. The parameters that were refined at the first stages of the analysis were the bond length and the vibrational amplitudes of the monomer molecule, the vapor composition, and the vibrational amplitudes of the other chromium-chlorine bond lengths grouped together with the monomer amplitude. We also refined the amplitudes of the most important nonbonded distances. The analysis was performed with the so-called static analysis, meaning that a thermally averaged structure was refined. Such a structure suffers from the shrinkage effect and usually has a lower symmetry than the equilibrium structure. Therefore, we introduced and refined the parameters describing the puckering and bending motions of the dimers and trimers.

We found that with the above constraints, the agreement between the experimental and theoretical distributions was not satisfactory, especially in the region of the bond length, indicating that the constrained bond length differences did not quite correspond to the measured structures. Therefore, we tried to carefully refine them, and they usually refined to somewhat smaller values than the computed ones. Since the computed bond length differences were not exactly the same from different levels of computations, we decided that allowing to refine these values was justified. Further, we let the bond angle of the monomer and those of the dimer also refine. They stayed close to the computed values.

2.15 Thermodynamic Analysis

The frequency analyses allowed us to determine the values of ΔH, ΔG, and ΔS of atomization at 298.15 K as well as from 1000–2000 K. Given these values, we were able to calculate the thermodynamics of the stepwise cluster formation within these temperature ranges as well as approximate the equilibrium vapor composition of these systems. We assumed that the clusters are formed in a stepwise fashion, meaning that the following reactions were examined:

$$\begin{aligned}
&(1) \quad 2\mathrm{CrX_2} \rightarrow \mathrm{Cr_2X_4} \\
&(2) \quad \mathrm{Cr_2X_4} + \mathrm{CrX_2} \rightarrow \mathrm{Cr_3X_6} \\
&(3) \quad \mathrm{Cr_3X_6} + \mathrm{CrX_2} \rightarrow \mathrm{Cr_4X_8} \\
&(4) \quad 2\mathrm{Cr_2X_4} \rightarrow \mathrm{Cr_4X_8}
\end{aligned}$$

The equilibrium constants for these reactions are:

$$K_1 = \frac{P_d}{P_m^2} \tag{2.87}$$

$$K_2 = \frac{P_{tr}}{P_m P_d} \tag{2.88}$$

$$K_3 = \frac{P_{tet}}{P_m P_{tr}} \tag{2.89}$$

$$K_4 = \frac{P_{tet}}{P_d^2} \tag{2.90}$$

where P_m, P_d, P_{tr}, P_{tet} represent the partial pressures of the monomer, dimer, trimer, and tetramer, respectively. If we assume a constant total pressure of the gas mixture, then we can calculate the value of P_m by solving the following equation and taking only the realistic roots:

$$0 = P_m + K_1 P_m^2 + K_1 K_2 P_m^3 + (K_1 K_2 K_3 + K_1^2 K_4) P_m^4 - P_T \tag{2.91}$$

where P_T is the total pressure, and for simplicity reasons, this value was set to 1 atmosphere. The partial pressures of the remaining species can be determined through the use of Eq. 2.91 along with the equilibrium expressions.

Chapter 3

Results

3.1 Monomers

The results of the different-level computations on the CrF_2, $CrCl_2$, $CrBr_2$, and CrI_2 monomers are listed in Tables 3.1, 3.2, 3.3, and 3.4, respectively, together with the available literature data. Experimental structural parameters are also given for comparison. Considering the calculations of the linear geometries, from the three possible high-spin states: $^5\Sigma_g^+$ ($\delta_g^2\pi_g^2$), $^5\Pi_g$ ($\delta_g^2\pi_g^1\sigma_g^1$), and $^5\Delta_g$ ($\delta_g^1\pi_g^2\sigma_g^1$), DFT predicts that the $^5\Pi_g$ state is lowest in energy. However, the $^5\Pi_g$ state is not a local minimum, rather a second-order transition state, which splits into two nondegenerate states of $^5B_2$ and $^5A_2$ symmetry, of which the $^5B_2$ state is the ground state. Figure 3.1 depicts the bending potential curves for the $^5B_2$ and $^5A_2$ states of CrF_2 to CrI_2 from B3LYP (CrF_2 and $CrCl_2$) and PW91 ($CrBr_2$ and CrI_2) calculations. We see that the $^5B_2$ state is at a maximum at 180° for all of the chromium dihalides, with minima located between 140° for CrF_2 to roughly 175° for CrI_2. The $^5A_2$ state for all of the chromium dihalides has a minimum at 180° and increases in energy substantially with bending. Note that the bending curve for the $^5A_2$ state becomes flatter going down the halide group. All of the chromium dihalides have a shallow bending potential for the $^5B_2$ state, below 0.1 eV from all computations except HF. The bending potential decreases substantially going from F to I, which is also reflected by an increase in the bond angle of the $^5B_2$ state. For CrI_2, the $^5B_2$ state lies less than 0.060 eV below the $^5\Pi_g$ state from all of the DFT, CCSD(T), and MP2 calculations. Interestingly, the bond angle of the $^5B_2$ state changes only slightly among the different DFT methods, with the exception of CrI_2, as the very shallow bending potential may be

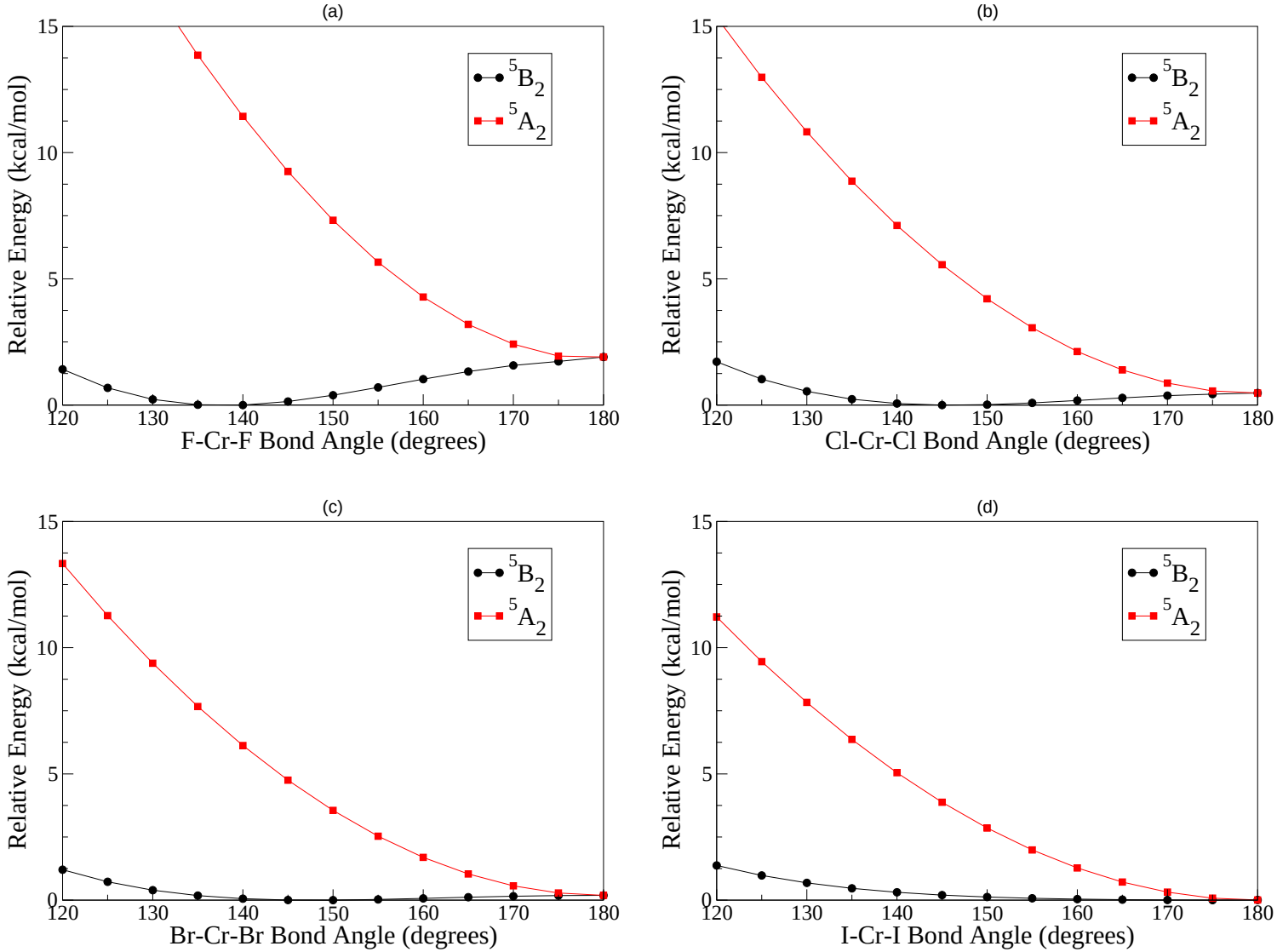

Figure 3.1: DFT bending potential curves of the $^5B_2$ and $^5A_2$ states for (a) CrF_2, (b) $CrCl_2$, (c) $CrBr_2$, and (d) CrI_2.

Table 3.1: Relative energies, geometrical parameters, and vibrational frequencies of CrF_2 in different electronic states. Energies in eV, distances in Å, angles in degrees, and frequencies in cm^{-1}.

State	Method[a]	Ref.[b]	ΔE	R(CrF)	$\angle$(FCrF)	ν^c_{bend}	$\nu_{sym-str}$	$\nu_{asym-str}$
	exp.	[2, 4]	-	1.776[d]	-	135(32)[e],155.4[f]	593[g]	654.5[f],688[g]
	exp.	[6]	-	-	-	-	-	697[h]
$^5B_2$	B3LYP		0	1.778	136.3	119.5	613.7	715.8
	PW91		0	1.767	132.8	138.6	623.9	715.4
	PBE		0	1.769	132.7	139.6	621.3	711.9
	LSDA		0	1.731	132.3	151.8	676.0	773.0
	CCSD(T)		0	1.791	149.3	-	-	-
	UHF		0.402	1.829	153.4	61.7	567.7	743.3
	MP2		0.007	1.789	151.4	77.4	575.3	980.2
	CASPT2		0.079	1.795	143.1	-	-	-
	CASSCF[i]		0	1.778	136.3	-	-	-
	B3LYP	[22]	0	1.7860	137.5	116	600	701
	CCSD(T)	[22]	0	1.7987	145.1	99	574	748
$^5\Pi_g$	B3LYP		0.079	1.789	180	$116.0i$/155.8[j]	580.8	736.9
	PW91		0.117	1.783	180	$128.4i$/151.5[j]	580.3	728.4
	PBE		0.120	1.785	180	$128.8i$/150.9[j]	577.3	724.6
	LSDA		0.129	1.747	180	$141.4i$/148.0[j]	626.0	776.6
	CCSD(T)		0.018	1.795	180	-	-	-
	UHF		0.409	1.831	180	$44.5i$/162.1[j]	553.2	728.8
	MP2		0.020	1.793	180	$58.9i$/174.5j	563.4	738.2
	CASPT2		0.161	1.803	180	-	-	-
	CASSCF[i]		0.010	1.789	180	-	-	-
	BP-VWN	[19]	0	1.772	180	i[j]	584	700
$^5\Sigma^+_g$	B3LYP		0.201	1.835	180	131.0	577.8	672.7
	PW91		0.493	1.834	180	120.7	568.5	661.6
	PBE		0.500	1.836	180	119.7	566.6	659.0
	LSDA		0.678	1.800	180	106.9	604.0	702.1
	CCSD(T)		0.080	1.842	180	-	-	-
	UHF		0	1.848	180	157.1	585.1	699.8
	MP2		0	1.841	180	142.7	574.0	673.5
	CASPT2		0	1.841	180	-	-	-
	CASSCF[i]		0.798	1.835	180	-	-	-
	BP-VWN	[19]	0.47	1.825	180	-	-	-

Table 3.1 *Continued*

State	Method[a]	Ref.[b]	ΔE	R(CrF)	$\angle$(FCrF)	ν^{c}_{bend}	$\nu_{sym-str}$	$\nu_{asym-str}$
$^5\Delta_g$	B3LYP		1.124	1.826	180	82.2	562.6	706.4
	PW91		1.395	1.822	180	$39.6i^{j}$	563.4	699.0
	PBE		1.413	1.825	180	$47.7i^{j}$	560.4	695.2
	LSDA		1.596	1.788	180	$85.4i^{j}$	601.4	740.4
	CCSD(T)		1.062	1.834	180	-	-	-
	UHF		1.231	1.855	180	121.8	536.8	711.3
	MP2		1.002	1.836	180	113.7	548.6	705.0
	CASPT2		1.078	1.842	180	-	-	-
	CASSCF[i]		1.052	1.826	180	-	-	-
$^3\Sigma^-_g$	B3LYP		1.665	1.739	180	$110.5i^{j}$	616.6	813.2
	PW91		1.681	1.729	180	$126.3i^{j}$	624.7	811.2
	PBE		1.680	1.731	180	$125.4i^{j}$	622.7	808.2
	LSDA		1.461	1.691	180	$134.2i^{j}$	683.6	872.4
	CCSD(T)		1.738	1.739	180	-	-	-
	UHF		3.383	1.788	180	$46.5i^{j}$	566.5	784.7
	MP2		2.113	1.741	180	85.9	594.6	812.4
	CASPT2		2.396	1.772	180	-	-	-
	BP-VWN	[19]	1.41	1.721	180	-	-	-
$^1\Sigma^+_g$	B3LYP		4.114	1.720	180	98.1	669.0	779.5
	PW91		4.102	1.714	180	42.4	662.5	776.0
	PBE		4.107	1.716	180	41.7	659.3	772.3
	LSDA		3.669	1.684	180	$21.9i^{j}$	707.7	826.4
	CCSD(T)		4.201	1.734	180	-	-	-
	UHF		6.440	1.749	180	173.8	658.6	780.7
	MP2		4.274	1.717	180	151.2	670.9	773.3
	CASPT2		3.489	1.770	180	-	-	-
	BP-VWN	[19]	3.71	1.710	180	-	-	-

[a] Unless otherwise mentioned, a CASSCF(4,5) was used. [b] Unless otherwise stated, the data given are from this study. [c] For the linear structures, the bending mode is doubly degenerate. [d] ED (r_e) value from Ref. [4]. [e] Estimated gas-phase value from Ref. [4]. [f] MI-IR (Ar) from Ref. [6]. [g] Estimated value from Ref. [2]. [h] Estimated gas-phase value from Ref. [6]. [i] A CASSCF(16,15) was used. [j] Imaginary frequency in the bending mode.

Table 3.2: Relative energies, geometrical parameters, and vibrational frequencies of $CrCl_2$ in different electronic states. Energies in eV, distances in Å, angles in degrees, and frequencies in cm^{-1}.

State	Method[a]	Ref.[b]	ΔE	R(CrCl)	∠(ClCrCl)	ν^c_{bend}	$\nu_{sym-str}$	$\nu_{asym-str}$
	exp.	[5,9]	-	-	-	-	-	493.5[d],457.4[e]
		[7,8]	-	-	-	110.5[g]	-	475[f],458.5[g]
		[12]	-	-	-	-	-	422[h]
	exp.[i]			2.196(20)	149(9.5)			
$^5B_2$	B3LYP		0	2.193	146.7	49.3	349.4	472.8
	B3PW91[j]		0	2.175	143.6	56.8	357.6	476.7
	PW91		0	2.171	141.3	54.4	358.1	473.1
	PBE		0	2.173	140.7	56.9	357.5	471.2
	LSDA		0	2.123	137.5	63.9	390.6	506.0
	CCSD(T)		0	2.194	167.0	32.4	337.9	492.2
	UHF		0.219	2.270	180	39.4/92.6	314.9	468.1
	MP2		0	2.191	177.4	5.3	332.6	495.2
	CASPT2		0.035	2.201	167.5	-	-	-
	CASSCF[k]		0	2.193	146.7	-	-	-
	B3LYP	[21]	0	2.201	144.3	57.2	344.2	467.3
	CCSD(T)	[22]	0	2.199	156.2	45	338	486
$^5\Pi_g$	B3LYP		0.020	2.198	180	$47.4i/92.4^l$	329.6	479.0
	B3PW91[j]		0.027	2.182	180	$46.2i/98.1^l$	334.1	484.5
	PW91		0.030	2.181	180	$50.8i/92.5^l$	330.1	478.4
	PBE		0.033	2.183	180	$53.1i/91.1^l$	328.5	476.0
	LSDA		0.045	2.136	180	$54.2i/94.8^l$	356.4	511.9
	CCSD(T)		0.032	2.194	180	-	-	-
	UHF		0.219	2.270	180	39.4/92.6	314.9	468.1
	MP2		0.001	2.191	180	$3.8i/100.0^l$	332.5	495.2
	CASPT2		0.085	2.202	180	-	-	-
	CASSCF[k]		0.075	2.198	180	-	-	-
	CASSCF	[111]	-	2.175	180	-	-	-
	B3LYP	[21]	0.012	2.209	180	-	-	-
	BP-VWN	[19]	0	2.173	180	i^l	358	476
	LSDA	[20]	0	2.15	180	85	315	480
	HF	[18]	0.282	2.309	180	-	-	-

Table 3.2 *Continued*

State	Method[a]	Ref.[b]	ΔE	R(CrCl)	$\angle$(ClCrCl)	ν^c_{bend}	$\nu_{sym-str}$	$\nu_{asym-str}$
$^5\Sigma_g^+$	B3LYP		0.156	2.239	180	69.7	327.7	460.3
	PW91		0.403	2.224	180	53.8	326.5	459.3
	PBE		0.400	2.225	180	52.2	325.6	458.0
	LSDA		0.566	2.181	180	35.6	347.7	488.4
	CCSD(T)		0.145	2.240	180	80.8	333.5	474.8
	UHF		0	2.286	180	91.9	325.0	466.3
	MP2		0.010	2.234	180	86.2	335.8	478.6
	CASPT2		0	2.240	180	-	-	-
	CASSCF[k]		0.276	2.239	180	-	-	-
	B3LYP	[21]	0.200	2.248	180	-	-	-
	BP-VWN	[19]	0.44	2.216	180	-	-	-
	HF	[18]	0	2.315	180	-	-	-
	LSDA	[20]	0.532	2.21	180	65	326	465
$^5\Delta_g$	B3LYP		0.804	2.226	180	49.9	322.5	468.9
	PW91		1.079	2.206	180	$98.8i^l$	327.8	471.9
	PBE		1.090	2.208	180	$104.5i^l$	326.5	470.1
	LSDA		1.239	2.162	180	$191.1i^l$	351.9	502.9
	CCSD(T)		0.765	2.228	180	-	-	-
	UHF		0.735	2.289	180	76.2	309.5	462.2
	MP2		0.653	2.224	180	76.0	325.3	486.2
	CASPT2		0.654	2.229	180	-	-	-
	CASSCF[k]		0.910	2.226	180	-	-	-
	B3LYP	[21]	0.860	2.237	180	-	-	-
	LSDA	[20]	1.039	2.183	180	56	325	459
$^3\Sigma_g^-$	B3LYP		1.636	2.135	180	19.8	352.1	510.0
	PW91		1.626	2.112	180	8.7	362.6	517.2
	PBE		1.640	2.114	180	$4.0i^l$	361.2	514.9
	LSDA		1.409	2.066	180	23.6	393.8	555.2
	CCSD(T)		1.794	2.122	180	-	-	-
	UHF		3.170	2.227	180	50.0	314.1	477.8
	MP2		2.096	2.111	180	46.8	353.7	526.7
	CASPT2		2.319	2.158	180	-	-	-
	BP-VWN	[19]	1.45	2.101	180	-	-	-
	LSDA	[20]	0.899	2.078	180	90	348	540

Table 3.2 *Continued*

State	Method[a]	Ref.[b]	ΔE	R(CrCl)	$\angle$(ClCrCl)	ν^c_{bend}	$\nu_{sym-str}$	$\nu_{asym-str}$
$^1\Sigma_g^+$	B3LYP		5.025	2.144	180	51.7	367.8	508.5
	PW91		4.906	2.126	180	17.1	369.0	512.7
	PBE		4.913	2.128	180	15.8	367.5	510.6
	LSDA		4.489	2.086	180	$19.1i^l$	393.4	546.6
	CCSD(T)		4.284	2.170	180	-	-	-
	CASPT2		3.503	2.138	180	-	-	-
	BP-VWN	[19]	4.65	2.126	180	-	-	-

[a] Unless otherwise mentioned, a CASSCF(4,5) was used. [b] Unless otherwise stated, the data given are from this study. [c] For the linear structures, the bending mode is doubly degenerate. [d] MI-IR (Ar) from Ref. [5]. [e] MI-IR (Ar) from Ref. [9]. [f] Gas-phase IR data from Ref. [8]. [g] MI-IR (Ar) from Ref. [7]. [h] Gas-phase IR value from Ref. [12]. [i] Result from our ED refinement. [j] cc-pVTZ basis set used for Cl. [k] A CASSCF(16,15) was used. [l] Imaginary frequency in the bending mode.

Table 3.3: Relative energies, geometrical parameters, and vibrational frequencies of $CrBr_2$ in different electronic states. Energies in eV, distances in Å, angles in degrees, and frequencies in cm^{-1}.

State	Method[a]	Ref.[b]	ΔE	R(CrBr)	$\angle$(BrCrBr)	ν^c_{bend}	$\nu_{sym-str}$	$\nu_{asym-str}$
	exp.	[8, 11]	-	-	-	-	-	363.0^d, 365^e
$^5B_2$	B3LYP		0	2.342	150.1	33.0	220.5	376.6
	PW91		0	2.322	148.0	32.2	223.8	376.3
	PBE		0	2.324	146.9	33.7	224.4	374.4
	LSDA		0	2.267	140.8	35.6	255.4	403.7
	CCSD(T)		0	2.329	179.8	-	-	-
	UHF		0.167	2.419	180	40.3/73.9	193.8	378.2
	MP2		0	2.327	180	32.3/82.7	206.7	408.3
	CASPT2		0.003	2.346	179.9	-	-	-
	CASSCF[f]		0	2.322	148.0	-	-	-

Table 3.3 *Continued*

State	Method[a]	Ref.[b]	ΔE	R(CrBr)	$\angle$(BrCrBr)	ν^c_{bend}	$\nu_{sym-str}$	$\nu_{asym-str}$
$^5\Pi_g$	B3LYP		0.009	2.347	180	$24.4i/73.9^g$	199.6	384.9
	PW91		0.009	2.330	180	$21.4i/74.3^g$	197.9	382.0
	PBE		0.011	2.333	180	$24.1i/73.4^g$	197.0	380.4
	LSDA		0.053	2.278	180	$33.1i/73.1^g$	214.8	411.9
	CCSD(T)		$1.4\text{x}10^{-4}$	2.329	180	-	-	-
	UHF		0.167	2.419	180	40.3/73.9	193.8	378.2
	MP2		0	2.327	180	32.3/82.7	206.7	408.3
	CASPT2		0.055	2.347	180	-	-	-
	CASSCF[f]		0.015	2.330	180	-	-	-
$^5\Sigma^+_g$	B3LYP		0.192	2.386	180	55.1	200.2	375.9
	PW91		0.449	2.370	180	35.2	199.3	375.4
	PBE		0.444	2.372	180	33.9	198.8	374.6
	LSDA		0.631	2.321	180	$19.0i^g$	211.1	397.6
	CCSD(T)		0.162	2.377	180	-	-	-
	UHF		0	2.436	180	73.2	198.7	378.1
	MP2		0.044	2.370	180	72.4	208.4	397.0
	CASPT2		0	2.384	180	-	-	-
	CASSCF[e]		0.176	2.370	180	-	-	-
$^5\Delta_g$	B3LYP		0.763	2.372	180	36.9	197.0	379.9
	PW91		1.057	2.349	180	150.2	199.8	382.4
	PBE		1.065	2.352	180	138.1	199.1	381.2
	LSDA		1.237	2.300	180	108.1	214.4	408.5
	CCSD(T)		0.678	2.363	180	-	-	-
	UHF		0.615	2.436	180	62.3	191.0	373.9
	MP2		0.589	2.358	180	66.3	203.1	401.5
	CASPT2		0.549	2.372	180	-	-	-
	CASSCF[f]		0.882	2.349	180	-	-	-
$^3\Sigma^-_g$	B3LYP		1.642	2.280	180	30.2	213.5	409.2
	PW91		1.623	2.256	180	27.1	218.5	413.5
	PBE		1.635	2.258	180	26.9	217.7	411.8
	LSDA		1.439	2.202	180	28.8	238.5	446.7
	CCSD(T)		1.761	2.255	180	-	-	-
	UHF		3.108	2.378	180	47.5	193.6	384.5
	MP2		2.128	2.246	180	52.1	217.7	433.2
	CASPT2		2.293	2.302	180	-	-	-

Table 3.3 *Continued*

State	Method[a]	Ref.[b]	ΔE	R(CrBr)	$\angle$(BrCrBr)	ν^c_{bend}	$\nu_{sym-str}$	$\nu_{asym-str}$
$^1\Sigma_g^+$	B3LYP		5.216	2.294	180	36.3	221.0	409.0
	PW91		5.070	2.274	180	$20.0i^g$	221.4	411.5
	PBE		5.075	2.277	180	$19.4i^g$	220.6	410.0
	LSDA		4.676	2.227	180	$34.7i^g$	236.5	439.1
	CCSD(T)		4.347	2.309	180	-	-	-
	UHF		7.698	2.366	180	72.2	213.5	400.2
	MP2		5.487	2.264	180	54.4	230.2	427.3
	CASPT2		3.364	2.302	180	-	-	-

[a] Unless otherwise mentioned, a CASSCF(4,5) was used. [b] Unless otherwise stated, the data given are from this study. [c] For the linear structures, the bending mode is doubly degenerate. [d] MI-IR (Ar) from Ref. [11]. [e] Gas-phase value from Ref. [8]. [f] A CASSCF(16,15) was used. [g] Imaginary frequency in the bending mode.

Table 3.4: Relative energies, geometrical parameters, and vibrational frequencies of CrI_2 in different electronic states. Energies in eV, distances in Å, angles in degrees, and frequencies in cm^{-1}.

State	Method[a]	Ref.[b]	ΔE	R(CrI)	$\angle$(ICrI)	ν^c_{bend}	$\nu_{sym-str}$	$\nu_{asym-str}$
	exp.	[10]	-	-	-	37^d	-	319.7^d
$^5B_2$	B3LYP		0	2.553	155.4	21.6	158.7	328.0
	PW91		0	2.540	174.5	13.0	141.0	328.8
	PBE		0	2.542	172.8	14.4	141.3	327.5
	LSDA		0	2.471	140.2	23.7	197.8	345.7
	CCSD(T)		0	2.530	167.8	-	-	-
	UHF		0.122	2.639	180	39.8/62.1	138.8	324.5
	MP2		0	2.532	180	35.8/70.2	149.3	354.1
	CASPT2		0	2.554	169.9	-	-	-
	CASSCF[e]		0	2.540	174.5	-	-	-

Table 3.4 *Continued*

State	Method[a]	Ref.[b]	ΔE	R(CrI)	$\angle$(ICrI)	ν^c_{bend}	$\nu_{sym-str}$	$\nu_{asym-str}$
$^5\Pi_g$	B3LYP		0.002	2.557	180	$18.1i/58.9^f$	141.2	330.4
	PW91		$3.8\text{x}10^{-4}$	2.540	180	$10.0i/58.1^f$	139.6	327.9
	PBE		$4.4\text{x}10^{-4}$	2.543	180	$12.5i/57.5^f$	139.0	326.4
	LSDA		0.008	2.484	180	$18.1i/58.4^f$	151.7	355.9
	CCSD(T)		0.001	2.531	180	-	-	-
	UHF		0.122	2.639	180	39.8/62.1	138.8	324.5
	MP2		0	2.532	180	35.8/70.2	149.3	354.1
	CASPT2		0.056	2.556	180	-	-	-
	CASSCF[e]		0.033	2.540	180	-	-	-
	LDA	[23]	0	2.499	180	70	148	345
$^5\Sigma^+_g$	B3LYP		0.241	2.593	180	41.0	141.6	324.5
	PW91		0.521	2.573	180	45.2	141.6	326.9
	PBE		0.514	2.575	180	45.1	141.2	325.9
	LSDA		0.645	2.519	180	$68.9i^f$	152.0	352.4
	CCSD(T)		0.208	2.581	180	-	-	-
	UHF		0	2.656	180	61.9	141.5	326.1
	MP2		0.066	2.575	180	62.9	150.3	347.7
	CASPT2		0.021	2.591	180	-	-	-
	CASSCF[e]		0.280	2.573	180	-	-	-
$^5\Delta_g$	B3LYP		0.725	2.575	180	17.2	140.6	328.1
	PW91		1.056	2.548	180	60.1	143.8	334.8
	PBE		1.062	2.551	180	58.3	143.3	333.6
	LSDA		1.182	2.494	180	55.1	155.2	361.4
	CCSD(T)		0.623	2.563	180	-	-	-
	UHF		0.480	2.650	180	54.7	137.2	321.6
	MP2		0.492	2.560	180	59.5	147.7	349.8
	CASPT2		0.443	2.573	180	-	-	-
	CASSCF[e]		0.734	2.548	180	-	-	-
$^3\Sigma^-_g$	B3LYP		1.701	2.488	180	28.1	150.2	348.2
	PW91		1.686	2.461	180	28.1	152.6	351.3
	PBE		1.698	2.464	180	28.5	152.1	350.0
	LSDA		1.482	2.402	180	29.4	166.8	382.7
	CCSD(T)		1.802	2.457	180	-	-	-
	UHF		3.062	2.599	180	44.0	139.0	327.6
	MP2		2.201	2.456	180	48.9	154.4	371.9
	CASPT2		2.308	2.512	180	-	-	-

Table 3.4 *Continued*

State	Method[a]	Ref.[b]	ΔE	R(CrI)	$\angle$(ICrI)	ν^c_{bend}	$\nu_{sym-str}$	$\nu_{asym-str}$
$^1\Sigma_g^+$	B3LYP		5.472	2.510	180	17.5	154.3	349.9
	PW91		5.304	2.484	180	$32.9i^f$	154.4	351.9
	PBE		5.307	2.487	180	$32.2i^f$	153.9	350.7
	LSDA		4.873	2.431	180	$42.5i^f$	164.9	377.1
	CCSD(T)		4.457	2.519	180	-	-	-
	UHF		7.951	2.598	180	59.2	150.4	342.1
	MP2		5.773	2.477	180	43.3	162.2	369.8
	CASPT2		3.373	2.512	180	-	-	-

[a] Unless otherwise mentioned, a CASSCF(4,5) was used. [b] Unless otherwise stated, the data given are from this study. [c] For the linear structures, the bending mode is doubly degenerate. [d] Gas-IR from Ref. [10]. [e] A CASSCF(16,15) was used. [f] Imaginary frequency in the bending mode.

responsible for this deviation.

Because the barrier to inversion of the chromium dihalides is so small, we predict that only a few vibrational states will fall within this energy well. According to our DFT calculations, the harmonic zero-point vibrational energies for the bending mode of the $^5B_2$ state are approximately 60, 25, 16, and 6.5 cm^{-1} for CrF_2, $CrCl_2$, $CrBr_2$, and CrI_2, with their barrier heights to linearity being 637, 161, 73, and 10 cm^{-1}, respectively. Hence, we are only able to fit 5 bending states into the energy well for CrF_2, 3 states for $CrCl_2$, 2 states for $CrBr_2$, and only one state for CrI_2. The ED experiments performed on CrF_2 [4] and $CrCl_2$ [3] were done at 1520 K and 1170 K, respectively. Using the Maxwell-Boltzmann equation for a distribution over 100 states (60–12060 cm^{-1} for CrF_2, 25–5025 cm^{-1} for $CrCl_2$), we calculate that 43% of the CrF_2 monomers and 16% of the $CrCl_2$ monomers will be below the energy barrier for bending at these temperatures. At 1000 K, we predict that only 9% of $CrBr_2$ and 2% of CrI_2 will be below their barriers for bending. It comes as no surprise why the experimental results to date have shown that these molecules are linear, as roughly 57% of CrF_2 and 84% of $CrCl_2$ would have more than enough energy to fluctuate between the bent double-minima. The average structure under these conditions would therefore be linear.

The splitting of the $^5\Pi_g$ electronic state is a typical Renner-Teller effect, characterizing linear molecules in degenerate electronic states. The Renner-Teller effect, similarly to the

better known Jahn-Teller effect, is the result of the coupling between the electronic and vibrational wavefunctions of the molecule (i.e. the breakdown of the Born-Oppenheimer approximation). The difference between the two effects is that the instability of the linear configuration is due to the quadratic or higher order coupling terms, while the Jahn-Teller effect for nonlinear degenerate systems is due to the linear coupling terms [112]. Consider for the moment the CrX_2 molecule in a $^5\Pi_g$ state. The reference configuration for a linear, triatomic molecule would have cylindrical symmetry.

We can introduce the two components of the bending distortion (in the x or y direction) in polar coordinates, $Q_x = \rho\cos\phi$, $Q_y = \rho\sin\phi$, with $\rho^2 = Q_x^2 + Q_y^2$. Accordingly, the quadratic terms of the vibronic coupling between the two electronic terms are equal to $\frac{1}{2}g\rho^2$, with $\frac{1}{2}g$ being the quadratic vibronic coupling constant. The vibronic coupling matrix for this case is:

$$W = \begin{vmatrix} 0 & \frac{1}{2}g\rho^2 \\ \frac{1}{2}g\rho^2 & 0 \end{vmatrix} \tag{3.1}$$

Solving the vibronic coupling secular equation for this type of system and including the elasticity term gives the vibronic coupling energy ($\epsilon_\pm(\rho)$) [113]:

$$\epsilon_\pm(\rho) = \frac{1}{2}(K_o \pm g)\rho^2 \tag{3.2}$$

where K_o is the force constant for bending. The two branches of the adiabatic potential energy surface (APES) are shown in Figure 3.2(a). We see that for weak coupling ($g < K_o$), the APES is just split in two by the bending vibrations. For larger g values, we see that the ϵ_- surface becomes very small and can even take on negative values ($g > K_o$). For a system with strong vibronic coupling, fourth-order coupling terms may be necessary to describe the APES behavior correctly. With the fourth-order terms included, the vibronic coupling energy becomes:

$$\epsilon_\pm(\rho) = \frac{1}{2}(K_o \pm g)\rho^2 + j\rho^4 \tag{3.3}$$

where j is the fourth-order coupling constant. The APES for a strongly coupled system is shown in Figure 3.2(b). We see that the upper surface looks similar to that with weak coupling, with the minimum located at $\rho = 0$. However, the lower surface has a maximum at $\rho = 0$ with minima located at a distance ρ_o from the center.

$$\rho_o = \sqrt{\frac{g - K_o}{4j}} \tag{3.4}$$

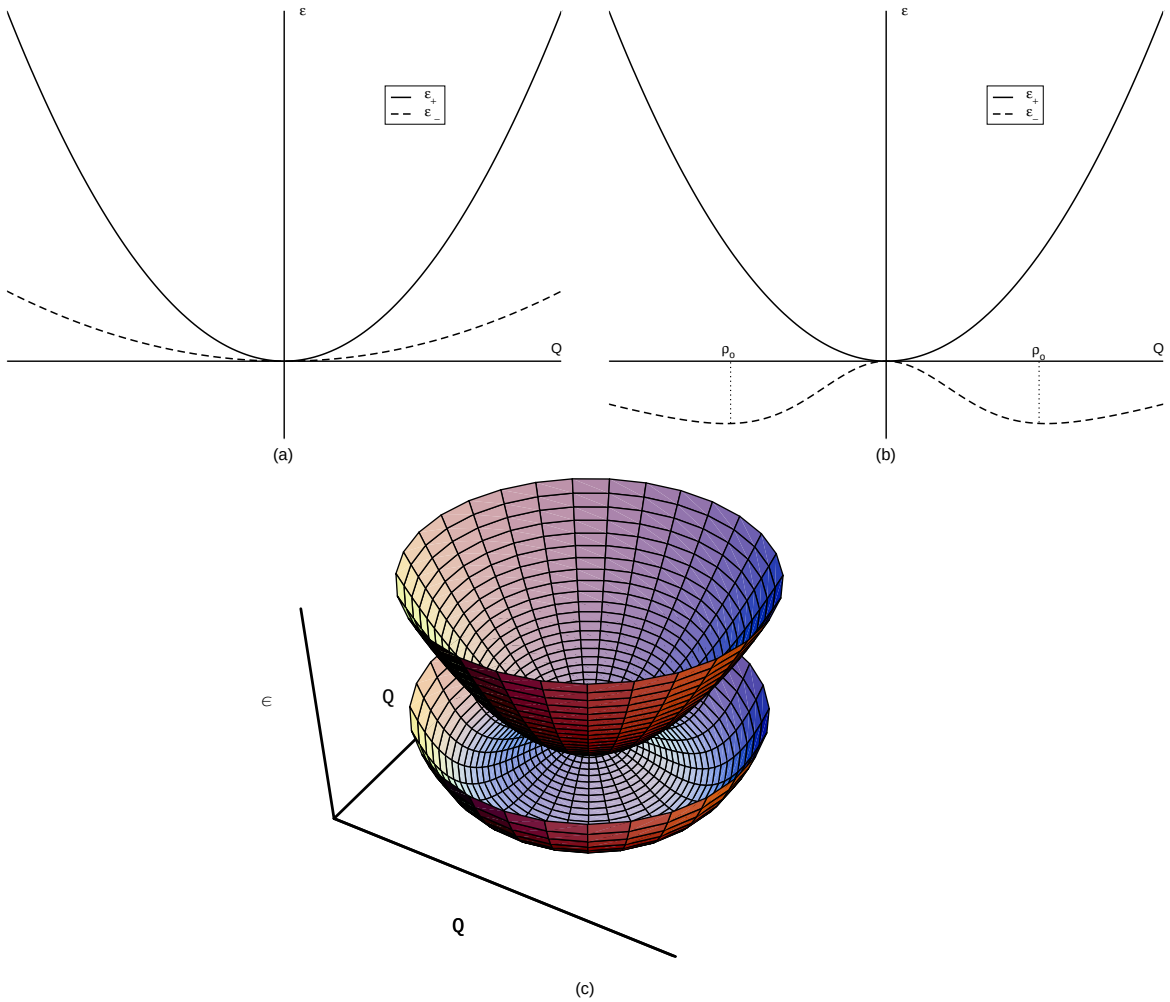

Figure 3.2: APES of a linear molecule in a doubly-degenerate ground state with respect to bending. (a) weak coupling - stable minimum; (b) strong coupling - dynamic instability of the ground state; (c) three-dimensional view of a strongly coupled system.

Figures 3.2(a) and (b) represent only a one-dimensional picture of the APES. A three-dimensional view of the APES for a strongly-coupled system is shown in Figure 3.2(c). We see that the APES is similar to the well-known Mexican hat topology.

Getting back to the CrX_2 molecule in the $^5\Pi_g$ state, we see that the upper APES represents bending into the $^5A_2$ state, and the lower APES represents bending into the $^5B_2$ state. A majority of our HF calculations on the $^5\Pi_g$ state predict weak vibronic coupling, thus leading to two different, real bending frequencies. Our DFT and some of the MP2 calculations show strong vibronic coupling with only one imaginary frequency for bending into the $^5B_2$ state (i.e. lower APES of Figure 3.2(b)), as single-reference methods fail to describe the situation correctly.

A more accurate description of the $^5\Pi_g$ state (and of the $^5\Delta_g$ state as well) is obtained from the state-averaged CASSCF calculations in which the π_g (or δ_g) orbitals possess half occupancies in each orbital. We note that the CASPT2(4,5) geometry optimization produces a structure in very close agreement with our CCSD(T) structures. The results of the CASSCF(16,15) (which lack major dynamic correlation) also predict a $^5B_2$ ground state with the $^5\Pi_g$ state lying slightly higher in energy for all of the chromium dihalides. The next state is the $^5\Sigma_g^+$ state. Both the CCSD(T) and DFT calculations predict that this state lies above the $^5B_2$ state, and the CCSD(T) calculations predict that it increases in energy relative to the $^5B_2$ state going from fluorine ($\Delta E = 0.08$ eV) to iodine ($\Delta E = 0.21$ eV). Our HF calculations predict that this state is the ground state for all of the monomers, thus showing that the inclusion of electron correlation is very important for these systems. There were, however, a few exceptions in the ordering of the $^5\Sigma_g^+$ state with some of the correlated calculations. MP2 predicts a $^5\Sigma_g^+$ ground state for CrF_2, and the CASPT2 calculations predict the same ground state for CrF_2 to $CrBr_2$. However, a limited active space was used in the CASPT2 calculations for the monomer, as these calculations were computationally time intensive; given that all of the CCSD(T) calculations predict a $^5B_2$ ground state, we are certain that this state falls below the $^5\Sigma_g^+$ state. The next state, $^5\Delta_g$, is considerably higher in energy by all methods and cannot be considered as a contestant for the ground state. Also, the lower spin triplet and singlet states of the monomers were both significantly higher in energy than the global minima.

The single-reference CCSD(T) procedure is capable of describing most states rather well, with the exception being the $^3\Sigma_g^-$ and $^1\Sigma_g^+$ states, as both of them exhibit significant multireference character. The major contributions to these two states as well as the state-

averaged $^5\Pi_g$ state are shown in Table 3.5. We see that the original configurations for the $^3\Sigma_g^-$ ($\sigma_g^2\delta_g^\alpha\delta_g^\alpha$) and the $^1\Sigma_g^+$ ($\delta_g^2\delta_g^2$) states contribute between 60–65% of their total wavefunctions. As expected, the $^5\Pi_g$ state consists of roughly a 50/50 mixture of two configurations.

Based on the literature data, the ground state of CrF_2 and $CrCl_2$ is expected to be the $^5B_2$ state arising from the Renner-Teller distorted $^5\Pi_g$ state. The B3LYP results from Jensen [21] show a flat bending potential for the $^5\Pi_g$ state of $CrCl_2$, with the barrier of inversion of only 0.012 eV. Nielsen [22] also mentioned an unusually flat bending potential for $CrCl_2$ and that the $^5B_2$ state was only 0.004 eV below that of the $^5\Pi_g$ state. There is a lack of quantum chemical and experimental data for $CrBr_2$ and CrI_2; however, based on the available data and our calculations, the ground state should be either the $^5\Sigma_g^+$ or $^5B_2$ states. Our B3LYP calculations on the $^5\Pi_g$ and $^5B_2$ states of CrF_2 and $CrCl_2$ agree very well with the experimental and quantum chemical geometries from the literature. The predicted Cr-I length from the LDA calculations of Schiefenhövel et al. [23] is shorter than our calculated values. Based on our calculations for all of the monomers, LSDA always underestimates the bond lengths. They also predicted a $^5\Pi_g$ ground state with identical, doubly degenerate bending frequencies. This result is unusual given that even our HF calculations, which lack electron correlation, predicted different bending frequencies. Calculating identical bending frequencies for this state would be possible with a multireference DFT approach, but the authors did not mention that such an approach was used.

The electronic absorption spectra of $CrCl_2$, reported by DeKock and Gruen [15] contains two transitions located at 5400 cm^{-1} and 9000 cm^{-1}. The oscillator strengths of these two transitions indicate that they arise from Laporte forbidden $d^4 \rightarrow d^4$ transitions. These type of transitions are indicative of a linear geometry which occur between the states of $D_{\infty h}$ symmetry. Based on ligand-field theory, DeKock and Gruen assigned these two transitions to $^5\Sigma_g^+ \rightarrow {}^5\Pi_g$ and $^5\Sigma_g^+ \rightarrow {}^5\Delta_g$, respectively. Because ligand-field theory incorrectly predicts the relative energies of the $3d$ metal orbitals, the assignment of the first transition is incorrect, as the $^5\Pi_g$ state is lower in energy than the $^5\Sigma_g^+$ state. Furthermore, the $^5\Pi_g \rightarrow {}^5\Sigma_g^+$ transition is calculated to be at 911 cm^{-1} at the CCSD(T) level, which is well below both excitation energies. The 5400 cm^{-1} transition is close to our calculated $^5\Pi_g \rightarrow {}^5\Delta_g$ transition, which is at 5912 cm^{-1} at the CCSD(T) level (not including zero-point vibrational effects). None of the transitions studied for $CrCl_2$ came

Table 3.5: Contributions from the major configurations within the active space of the $^3\Sigma_g^-$, $^1\Sigma_g^+$, and $^5\Pi_g$ states from CASPT2(4,5) geometry optimizations.

Molecule	State	Configuration[a]	%	Molecule	State	Configuration[a]	%
CrF_2	$^3\Sigma_g^-$	$\sigma_g^2\delta_g^\alpha\delta_g^\alpha$	65.51	$CrCl_2$	$^3\Sigma_g^-$	$\sigma_g^2\delta_g^\alpha\delta_g^\alpha$	62.54
		$\delta_g^\alpha\delta_g^\alpha\pi_g^2$	10.33			$\delta_g^\alpha\delta_g^\alpha\pi_g^2$	11.87
		$\sigma_g^2\pi_g^\alpha\pi_g^\alpha$	9.18			$\sigma_g^2\pi_g^\alpha\pi_g^\alpha$	10.15
		$\sigma_g^\alpha\delta_g^\alpha\pi_g^2$	7.49			$\sigma_g^\alpha\delta_g^\alpha\pi_g^2$	7.72
		$\sigma_g^\alpha\delta_g^\alpha\pi_g^\alpha\pi_g^\beta$	7.49			$\sigma_g^\alpha\delta_g^\alpha\pi_g^\alpha\pi_g^\beta$	7.72
	$^1\Sigma_g^+$	$\delta_g^2\delta_g^2$	68.08		$^1\Sigma_g^+$	$\delta_g^2\delta_g^2$	66.51
		$\delta_g^2\pi_g^2$	10.32			$\delta_g^2\pi_g^2$	10.38
		$\sigma_g^\alpha\delta_g^\beta\pi_g^2$	5.40			$\sigma_g^\alpha\delta_g^\beta\pi_g^2$	5.78
		$\sigma_g^\beta\delta_g^\alpha\pi_g^2$	5.40			$\sigma_g^\beta\delta_g^\alpha\pi_g^2$	5.78
		$\sigma_g^\alpha\delta_g^\beta\pi_g^\alpha\pi_g^\beta$	5.40			$\sigma_g^\alpha\delta_g^\beta\pi_g^\alpha\pi_g^\beta$	5.78
		$\sigma_g^\beta\delta_g^\alpha\pi_g^\alpha\pi_g^\beta$	5.40			$\sigma_g^\beta\delta_g^\alpha\pi_g^\alpha\pi_g^\beta$	5.78
	$^5\Pi_g$	$\sigma_g^\alpha\delta_g^\alpha\delta_g^\alpha\pi_g^\alpha\pi_g^0$	49.99		$^5\Pi_g$	$\sigma_g^\alpha\delta_g^\alpha\delta_g^\alpha\pi_g^\alpha\pi_g^0$	49.99
		$\sigma_g^\alpha\delta_g^\alpha\delta_g^\alpha\pi_g^0\pi_g^\alpha$	49.99			$\sigma_g^\alpha\delta_g^\alpha\delta_g^\alpha\pi_g^0\pi_g^\alpha$	49.99
$CrBr_2$	$^3\Sigma_g^-$	$\sigma_g^2\delta_g^\alpha\delta_g^\alpha$	61.94	CrI_2	$^3\Sigma_g^-$	$\sigma_g^2\delta_g^\alpha\delta_g^\alpha$	61.16
		$\delta_g^\alpha\delta_g^\alpha\pi_g^2$	12.15			$\delta_g^\alpha\delta_g^\alpha\pi_g^2$	12.43
		$\sigma_g^2\pi_g^\alpha\pi_g^\alpha$	10.40			$\sigma_g^2\pi_g^\alpha\pi_g^\alpha$	10.79
		$\sigma_g^\alpha\delta_g^\alpha\pi_g^2$	7.76			$\sigma_g^\alpha\delta_g^\alpha\pi_g^2$	7.81
		$\sigma_g^\alpha\delta_g^\alpha\pi_g^\alpha\pi_g^\beta$	7.76			$\sigma_g^\alpha\delta_g^\alpha\pi_g^\alpha\pi_g^\beta$	7.81
	$^1\Sigma_g^+$	$\delta_g^2\delta_g^2$	65.44		$^1\Sigma_g^+$	$\delta_g^2\delta_g^2$	64.36
		$\delta_g^2\pi_g^2$	10.57			$\delta_g^2\pi_g^2$	10.60
		$\sigma_g^\alpha\delta_g^\beta\pi_g^2$	6.00			$\sigma_g^\alpha\delta_g^\beta\pi_g^2$	6.26
		$\sigma_g^\beta\delta_g^\alpha\pi_g^2$	6.00			$\sigma_g^\beta\delta_g^\alpha\pi_g^2$	6.26
		$\sigma_g^\alpha\delta_g^\beta\pi_g^\alpha\pi_g^\beta$	6.00			$\sigma_g^\alpha\delta_g^\beta\pi_g^\alpha\pi_g^\beta$	6.26
		$\sigma_g^\beta\delta_g^\alpha\pi_g^\alpha\pi_g^\beta$	6.00			$\sigma_g^\beta\delta_g^\alpha\pi_g^\alpha\pi_g^\beta$	6.26
	$^5\Pi_g$	$\sigma_g^\alpha\delta_g^\alpha\delta_g^\alpha\pi_g^\alpha\pi_g^0$	49.97		$^5\Pi_g$	$\sigma_g^\alpha\delta_g^\alpha\delta_g^\alpha\pi_g^\alpha\pi_g^0$	49.96
		$\sigma_g^\alpha\delta_g^\alpha\delta_g^\alpha\pi_g^0\pi_g^\alpha$	49.97			$\sigma_g^\alpha\delta_g^\alpha\delta_g^\alpha\pi_g^0\pi_g^\alpha$	49.96

[a] Configurations with the |CI-coefficient| > 0.05.

close to the 9000 cm^{-1} transition, and it was predicted that this band could have arisen from transitions between rotational-vibrational levels of the $^5\Pi_g$ and $^5\Delta_g$ states [21]. This is rather unlikely according to our results, but multi-reference configuration interaction

calculations are needed to identify these bands, as done recently for example for CrO_2 [114].

Mulliken analyses were also carried out for the different monomer spin states, and the results are given in Table 3.6. Most of the spin density is located on the Cr atom with a small amount of spin density on the halide atoms. As expected, the interactions between the Cr and halide atoms become more covalent and less electrostatic going down the periodic table. For $CrBr_2$ and CrI_2, the Cr atom even takes on a partial negative charge. It is misleading to characterize these molecules as purely ionic.

3.1.1 Infrared Analysis

Examining the IR data for CrF_2, we see that our bending frequency calculated by B3LYP is lower than the argon matrix IR result from Hastie et al. [6] as well as the estimated value from Zasorin et al. [4]. The other DFT methods are in better aggreement with the bending frequencies. Our $\nu_{asym-str}$ values are in good agreement with the estimated gas-phase values by Hargittai [2] and from Hastie and coworkers. However, these values are significantly (60 cm^{-1}) higher than Hastie's MI-IR (Ar) result and are more than likely attributed to matrix effects.

For $CrCl_2$, the most intense IR band for the monomer arises from the asymmetric Cr-Cl stretching mode. The two DFT calculations predict this mode to occur at 473 and 477 cm^{-1}, respectively; while MP2 and CCSD(T) calculations give 497 and 493 cm^{-1}, respectively. The experimental information for this mode is rather confusing. Kobra assigned 475 cm^{-1} to the asymmetric stretching frequency in a gas-phase IR experiment [8]. From the three available argon matrix IR measurements, two groups assigned this mode similarly, at 458 cm^{-1} [7] and 457 cm^{-1} [9], while the third group assigned a value that is 40 cm^{-1} higher, 494 cm^{-1} [5]. To make the picture more complicated, Hastie et al. [7] measured $CrCl_2$ in a neon matrix and found the mode at 493 cm^{-1}. Even taking into account matrix shifts, the 40 cm^{-1} difference between the different matrices is too large – not to mention the difference between groups referring to the same matrix. The picture is further complicated by a relatively new gas-phase measurement that suggested a 422 cm^{-1} value for the asymmetric stretching frequency of $CrCl_2$ [10].

Beside the obvious problems of both high-temperature gas-phase and matrix isolation IR experiments, including an uncertain amount of dimeric or other polymeric species, there are also other uncertainties in the experiments. For example, in two of them [9, 10]

Table 3.6: Mulliken atomic charges and spin densities for the chromium dihalides. Positive or negative spins represent an excess of alpha or beta spin density, respectively.

Molecule	State	Atom	Charge	Spin	Molecule	State	Atom	Charge	Spin
CrF_2	$^5B_2$	Cr	1.106	4.081	$CrCl_2$	$^5B_2$	Cr	0.427	4.084
		F	-0.553	-0.040			Cl	-0.213	-0.042
	$^5\Pi_g$	Cr	1.168	4.099		$^5\Pi_g$	Cr	0.435	4.132
		F	-0.584	-0.049			Cl	-0.217	-0.066
	$^5\Sigma_g^+$	Cr	1.296	3.933		$^5\Sigma_g^+$	Cr	0.561	3.964
		F	-0.648	0.034			Cl	-0.280	0.018
	$^5\Delta_g$	Cr	1.156	3.960		$^5\Delta_g$	Cr	0.470	3.925
		F	-0.578	0.020			Cl	-0.235	0.037
	$^3\Sigma_g^-$	Cr	1.057	2.098		$^3\Sigma_g^-$	Cr	0.393	2.228
		F	-0.528	-0.049			Cl	-0.196	-0.114
	$^1\Sigma_g^+$	Cr	1.295	0		$^1\Sigma_g^+$	Cr	0.315	0
		F	-0.647	0			Cl	-0.157	0
$CrBr_2$	$^5B_2$	Cr	0.016	4.258	CrI_2	$^5B_2$	Cr	-0.260	4.513
		Br	-0.008	-0.129			I	0.130	-0.256
	$^5\Pi_g$	Cr	0.047	4.352		$^5\Pi_g$	Cr	-0.261	4.517
		Br	-0.024	-0.176			I	0.131	-0.258
	$^5\Sigma_g^+$	Cr	0.187	4.000		$^5\Sigma_g^+$	Cr	-0.146	4.042
		Br	-0.093	0			I	0.073	-0.021
	$^5\Delta_g$	Cr	0.082	3.895		$^5\Delta_g$	Cr	-0.251	3.902
		Br	-0.041	0.052			I	0.125	0.049
	$^3\Sigma_g^-$	Cr	-0.018	2.436		$^3\Sigma_g^-$	Cr	-0.320	2.456
		Br	0.009	-0.218			I	0.160	-0.228
	$^1\Sigma_g^+$	Cr	-0.025	0		$^1\Sigma_g^+$	Cr	-0.430	0
		Br	0.012	0			I	0.215	0

$CrCl_3$ was evaporated, not $CrCl_2$ and thus the vapor composition was, possibly, even more complicated. In another experiment [5] metallic chromium was reacted with chlorine gas at high temperature in argon atmosphere and the vapor composition was not checked.

For $CrBr_2$, our $\nu_{asym-str}$ value from the PW91 calculations on the $^5B_2$ state are in good agreement with the argon MI-IR of Gregory et al. [11] as well as the gas-phase IR value from Kobra [8]. Our PW91 results for the ν_{bend} and $\nu_{asym-str}$ frequencies for the $^5B_2$ state of CrI_2 agree very well with the gas-phase IR data from Konings and coworkers [10].

3.2 Clusters

3.2.1 Dimers

In order to ascertain the most likely representation of the global minima for all of the clusters, two important properties need to be considered. The first is symmetry and geometry, and several different trial geometries were explored to determine a likely structure for each cluster. Pictoral representations of these structures which were used for the dimers are given in Figure 3.3. Second, we have to consider the spin of the clusters. The chromium dihalide monomers can have three possible spin states (quintet, triplet, singlet), and all three of these must be considered for the clusters. This leads to a total of five possible states for the dimers (nonet, septet, quintet, triplet, singlet).

In the preliminary PW91/LanL2DZ geometry optimizations, all of the structures given in Figure 3.3 were optimized. Frequency calculations were performed on the converged structures to determine if it represented a local minimum or a saddle point. If a structure optimized to a saddle point, we reoptimized it along the imaginary frequency modes, which in almost all cases required the molecule to be of lower symmetry. If necessary, the geometry of the molecule was manually adjusted to facilitate convergence into the new geometry. One more important caveat needs to be considered. Because we are using an UKS approach in describing transition metal complexes, we need to be certain that the low-spin states are of broken symmetry because spin-symmetric representations for these states can produce unusually high energies and short metal-metal distances. To determine if the UKS orbitals represented a BS solution for the low-spin states, the orbitals were examined with the focus being on the nonbonding $3d$ orbitals of Cr. A BS solution would exhibit spin polarization on the two Cr atoms. For example, the BS solution for a singlet state would have four α electrons within the $3d$ orbitals on one Cr atom and four β electrons in *different* $3d$ orbitals on the other Cr atom (S=2 at each Cr atom). For clusters with low symmetry, the UKS approach typically converged to a BS solution. For the other clusters, the wavefunction symmetry was lowered slightly to allow for symmetry breaking. If this method did not produce a BS result, then spin contamination was introduced by manually shifting the occupied α and β $3d$ orbitals on the Cr atoms so that they were different. The orbitals were then re-examined and adjusted, if necessary, to ensure that the $3d$ α and β orbitals were not the same. The BS-DFT produced unreasonable $\langle S^2 \rangle$ values, which is a well-known (and disregarded) fact [52–55].

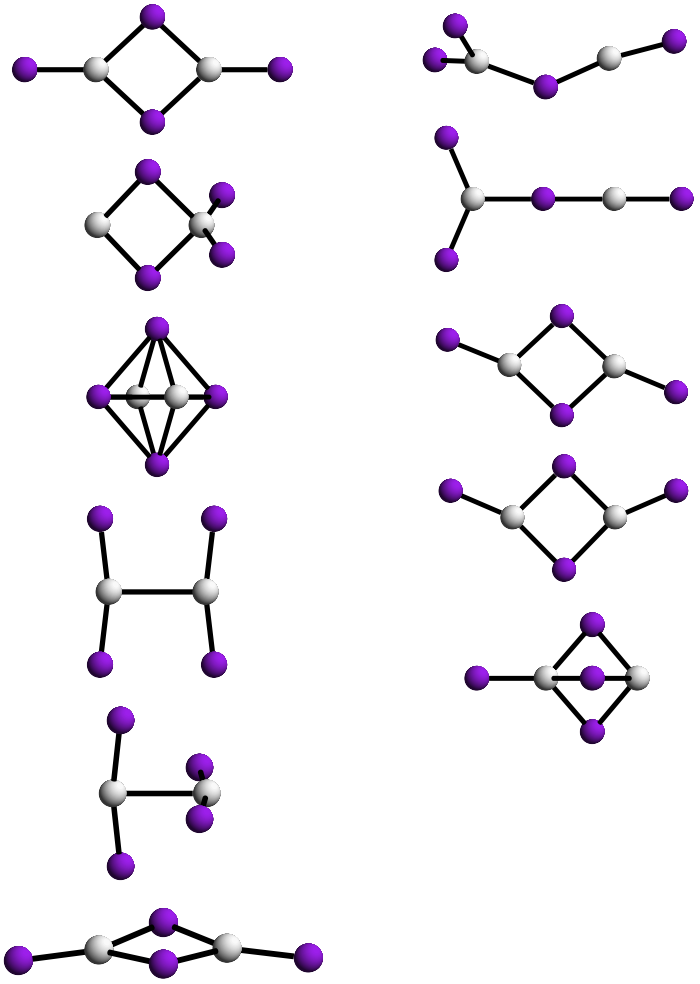

Figure 3.3: Initial dimer structures used in the preliminary analysis.

Figure 3.4 depicts the lowest energy minima from each spin state from our geometry optimizations. A comparison of their energies is given in Table 3.7. We see that our preliminary results (PW91/LanL2DZ column) show that the global minima consist of the singlet states of the planar structures with either C_{2v} or C_{2h} symmetry (D1) or (D2), respectively. The high-spin nonet states lie very close in energy to the singlet states. All of the other spin states were significantly higher in energy.

We included all minima within 1 eV of the global minima for further refinement with the larger basis sets. A comparison of their energies from different levels of theory are given in Table 3.7. According to our intensive analysis, we see that the global minima consist of the low-spin (singlet) states of structures (D1) or (D2) for the dimers. There

is one exception in which the global minimum of the CrI_2 dimer is the nonet state of (D1). Our results are surprising, considering that according to Hund's rule, one would expect the nonet states being more stable than the singlet states (vide infra). The most symmetrical planar structure (D_{2h}-symmetry) represented a second-order saddle-point with two imaginary frequencies for bending the terminal halide atoms within the plane of the molecule toward the *cis*-(D1) or *trans*-(D2) structures. This is again surprising because the D_{2h}-symmetry bridged structures are common for metal dihalide dimers [2]. The dimers in the septet, quintet, and triplet states are all considerably higher in energy, leading us to conclude that the dimers (and larger clusters) only consist of monomers which are in the quintet state.

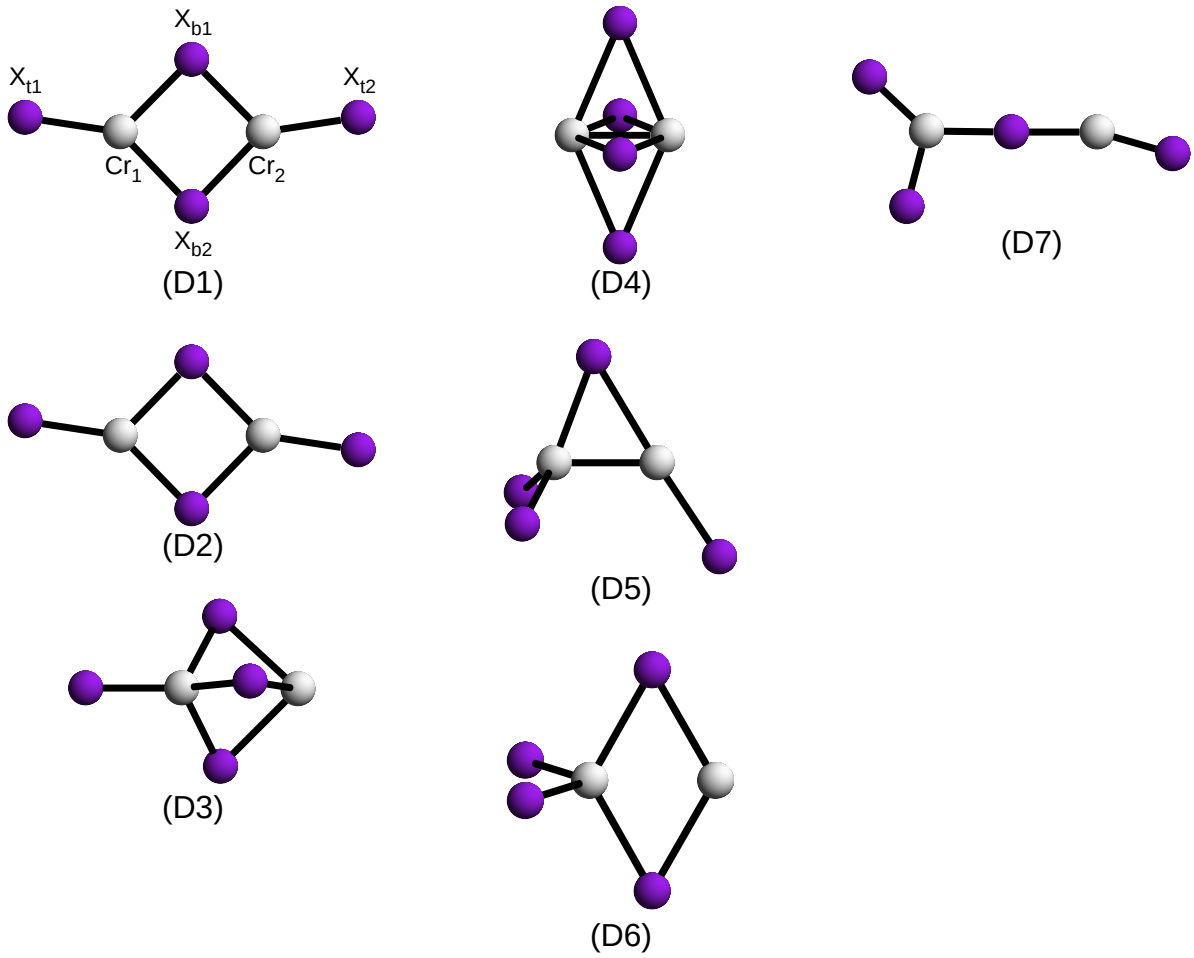

Figure 3.4: Representations of the low-energy minima for the dimers.

Looking again at the C_{2h} and C_{2v} structures, we can conceptualize that the C_{2h} structure could possibly be formed from two linear monomers. This type of symmetry can be extended to form a two-dimensional, chain-like structure by the addition of linear monomers. Interestingly, this sort of of chain-like structure is present in the solid-state of all of the chromium dihalides [115–120]. The C_{2v} structure can only be formed by having at least one bent monomer unit, and the D_{2h} structure must have both monomers being bent.

Table 3.7: Relative energies among the dimer minima from various geometry optimizations.

Molecule	Structure	State	ΔE (eV)	ΔE (eV)	ΔE (eV)	ΔE (eV)	ΔE (eV)	
Method[a]			PW91/LanL2DZ	B3LYP	HF	CASSCF(8,10)	CASPT2(8,10)	
Cr_2F_4	D1	$^9A_1$	0.021	0.015				
	D1	$^7B_1$	1.151					
	D1	$^5A_2$	1.507					
	D1	$^3B_1$	1.149					
	D1	$^1A_1$	0	0.001				
	D2	^9A_g	0.021	0.011	0	0	0.006	
	D2	^1A_g	0.010	0	21.115	0.042	0	
	D7	$^9A'$	0.857	[b]				
Method[a]			PW91/LanL2DZ	B3LYP	B3PW91	HF	CASSCF(8,10)	CASPT2(8,10)
Cr_2Cl_4	D1	$^9A_1$	0.024	0.054	0.050	0	0	0
	D1	$^7B_1$	1.228					
	D1	$^1A_1$	0	0	0	8.498	0.089	0.024
	D2	^9A_g	0.025	0.058	0.059			
	D2	^1A_g	0.001	0.001	0.004			
	D3	^9A	0.519	[b]				
	D3	^5A	1.486					
	D3	^3A	0.789	1.557				
Method[a]			PW91/LanL2DZ	PW91	HF	CASSCF(8,10)	CASPT2(8,10)	
Cr_2Br_4	D1	$^9A_1$	0.002	0.100	0	0	0	
	D1	$^5A_1$	1.540					
	D1	$^1A_1$	0	0	13.692	0.069	0.018	
	D2	^9A_g	0.047	0.102				
	D2	^1A_g	0.010	0.001				
	D3	^7A	1.135					
	D3	$^3A''$	0.639	0.768				
Method[a]			PW91/LanL2DZ	PW91	HF	CASSCF(8,10)	CASPT2(8,10)	
Cr_2I_4	D1	$^9A_1$	0.021	0	0	0	0	
	D1	$^1A_1$	0	0.001	20.263	0.095	0.033	
	D2	^9A_g	0.050	[b]				
	D2	^1A_g	0.020	0.004				
	D3	$^7A_1$	0.921	1.013				
	D4	$^1A_1$	0.800	[b]				
	D5	$^3A''$	0.910	0.985				
	D6	^5B	1.376					
	D6	^3B	0.657	0.862				

[a] See computational details for applied basis sets. [b] Optimized to (D1).

The nonet and singlet states are very close in energy, and they also have similar geometries. A comparison of the geometry between the lowest energy singlet and nonet states for all of the dimers can be seen in Table 3.8 with the atomic labeling scheme given in Figure 3.4. We see that the Cr-X_{t1} distance changes very little between the two different spin states. Most of the differences in bond length between the singlet and nonet states come from the Cr-X_b and Cr-Cr distances. The Cr-Cr distance for the nonet states are between 0.03–0.1 Å longer than in the singlet states, and these differences increase going from F to Br. The exception to this trend is the nonet state of the CrI_2 dimer, whose Cr-Cr distance is *shorter* than the singlet state and comparable to the Cr-Cr distance in Cr_2F_4. The overall trend is that the geometry of the two spin states is almost identical for Cr_2F_4 and become less similar going down the halide group. All of the C_{2v} structures are fully planar with a ring puckering angle of zero degrees. The B3PW91 structures for Cr_2Cl_4 along with the larger cc-pVTZ basis sets for Cl are very similar to the B3LYP structures and will not be mentioned here.

Schiefenhövel et al. [23] calculated the geometry of the CrI_2 dimer with LDA. They determined that the global minimum of Cr_2I_4 has C_{2v} symmetry with a $^9B_2$ ground state. Their structure was not planar and had a ring puckering angle of 10.2°. They also calculated that the Cr-Cr, Cr-I_t, and Cr-I_b distances were 3.000 Å, 2.493 Å, and 2.594 Å, respectively. Their values for $\angle$(I_t-Cr-I_b) and $\angle$(I_b-Cr-I_b) were 125.5°, and 108.5°, respectively. We see that their calculated global minimum is qualitatively similar to ours (i.e. high-spin ground state with C_{2v} symmetry), but their bond lengths are all significantly shorter than our values. This result is to be expected, as LDA tends to underestimate bond lengths, which was indeed observed in our geometry optimizations for the monomers.

The general trend for the Mulliken spin densities is that most of the spin is located on the chromium atoms with only a small amount of spin present on the halides (Table 3.9). The magnitude of spin present on the Cr atoms also increases going down the halide group. All of the singlet states represent broken-symmetry structures, as there is a significant amount of spin polarization present on the chromium atoms, with one chromium atom having an excess of roughly four α electrons, and the other chromium atom having a concomitant excess of β electrons. The orbitals responsible for the spin polarization come from the $3d$ orbitals of Cr, in which all of the α and β electrons are occupied within different orbitals. There is even a slight amount of spin polarization present on the terminal halide atoms, with the signs of their spin being the same as those

Table 3.8: Geometrical parameters for the lowest energy singlet and nonet dimers obtained from intensive geometry optimizations.

Molecule	State	Parameter	Value[a]	Molecule	State	Parameter	Value[a]
Cr_2F_4	^9A_g	R(Cr_1-Cr_2)	3.045	Cr_2Br_4	$^9A_1$	R(Cr_1-Cr_2)	3.388
		R(Cr_1-F_{t1})	1.805			R(Cr_1-Br_{t1})	2.337
		R(Cr_1-F_{b1})	1.950			R(Cr_1-Br_{b1})	2.447
		R(Cr_1-F_{b2})	1.982			R(Cr_1-Br_{b2})	2.526
		∠(F_{t1}-Cr_1-F_{b1})	123.0			∠(Br_{t1}-Cr_1-Br_{b1})	116.0
		∠(F_{t1}-Cr_1-F_{b2})	158.5			∠(Br_{t1}-Cr_1-Br_{b2})	149.9
		∠(F_{b1}-Cr_1-F_{b2})	78.5			∠(Br_{b1}-Cr_1-Br_{b2})	94.1
	^1A_g	R(Cr_1-Cr_2)	3.016		$^1A_1$	R(Cr_1-Cr_2)	3.284
		R(Cr_1-F_{t1})	1.804			R(Cr_1-Br_{t1})	2.331
		R(Cr_1-F_{b1})	1.948			R(Cr_1-Br_{b1})	2.467
		R(Cr_1-F_{b2})	1.981			R(Cr_1-Br_{b2})	2.467
		∠(F_{t1}-Cr_1-F_{b1})	123.6			∠(Br_{t1}-Cr_1-Br_{b1})	131.7
		∠(F_{t1}-Cr_1-F_{b2})	156.8			∠(Br_{t1}-Cr_1-Br_{b2})	131.8
		∠(F_{b1}-Cr_1-F_{b2})	79.7			∠(Br_{b1}-Cr_1-Br_{b2})	96.6
Cr_2Cl_4[b]	$^9A_1$	R(Cr_1-Cr_2)	3.384	Cr_2I_4	$^9A_1$	R(Cr_1-Cr_2)	3.078
		R(Cr_1-Cl_{t1})	2.211			R(Cr_1-I_{t1})	2.543
		R(Cr_1-Cl_{b1})	2.355			R(Cr_1-I_{b1})	2.651
		R(Cr_1-Cl_{b2})	2.389			R(Cr_1-I_{b2})	2.651
		∠(Cl_{t1}-Cr_1-Cl_{b1})	122.9			∠(I_{t1}-Cr_1-I_{b1})	125.5
		∠(Cl_{t1}-Cr_1-Cl_{b2})	148.1			∠(I_{t1}-Cr_1-I_{b2})	125.5
		∠(Cl_{b1}-Cr_1-Cl_{b2})	89.0			∠(I_{b1}-Cr_1-I_{b2})	109.0
	$^1A_1$	R(Cr_1-Cr_2)	3.307		$^1A_1$	R(Cr_1-Cr_2)	3.437
		R(Cr_1-Cl_{t1})	2.210			R(Cr_1-I_{t1})	2.537
		R(Cr_1-Cl_{b1})	2.354			R(Cr_1-I_{b1})	2.654
		R(Cr_1-Cl_{b2})	2.373			R(Cr_1-I_{b2})	2.676
		∠(Cl_{t1}-Cr_1-Cl_{b1})	125.9			∠(I_{t1}-Cr_1-I_{b1})	121.5
		∠(Cl_{t1}-Cr_1-Cl_{b2})	142.9			∠(I_{t1}-Cr_1-I_{b2})	138.8
		∠(Cl_{b1}-Cr_1-Cl_{b2})	91.2			∠(I_{b1}-Cr_1-I_{b2})	99.7

[a] All bond lengths in Å and all bond angles in degrees. [b] B3LYP structures.

Table 3.9: Mulliken charges and spin densities for the lowest energy singlet and nonet dimers obtained from the intensive geometry optimizations. Positive or negative spin represents an excess of alpha or beta electrons, respectively.

Molecule	State	Atom	Charge	Spin	Molecule	State	Atom	Charge	Spin
Cr_2F_4	^9A_g	Cr_1	1.12	4.05	Cr_2Br_4	$^9A_1$	Cr_1	-0.16	4.25
		Cr_2	1.12	4.05			Cr_2	-0.16	4.25
		F_{t1}	-0.63	-0.01			Br_t	-0.07	-0.09
		F_{b1}	-0.49	0.05			Br_{b1}	0.11	-0.11
	^1A_g	Cr_1	1.12	3.97			Br_{b2}	0.34	-0.21
		Cr_2	1.12	-3.97		$^1A_1$	Cr_1	-0.18	4.11
		F_{t1}	-0.63	0.01			Cr_2	-0.18	-4.11
		F_{t2}	-0.63	-0.01			Br_{t1}	-0.06	0.09
		F_{b1}	-0.49	0			Br_{t2}	-0.06	-0.09
							Br_{b1}	0.24	0
							Br_{b2}	0.25	0
Cr_2Cl_4[a]	$^9A_1$	Cr_1	0.41	4.08	Cr_2I_4	$^9A_1$	Cr_1	-0.44	4.36
		Cr_2	0.41	4.08			Cr_2	-0.44	4.36
		Cl_t	-0.31	-0.01			I_t	0.10	-0.16
		Cl_{b1}	-0.05	-0.08			I_{b1}	0.34	-0.20
		Cl_{b2}	-0.14	-0.06			I_{b2}	0.34	-0.20
	$^1A_1$	Cr_1	0.40	4.06		$^1A_1$	Cr_1	-0.42	4.20
		Cr_2	0.40	-4.06			Cr_2	-0.42	-4.20
		Cl_{t1}	-0.31	0.01			I_{t1}	0.09	0.17
		Cl_{t2}	-0.31	-0.01			I_{t2}	0.09	-0.17
		Cl_{b1}	-0.06	0			I_{b1}	0.27	0
		Cl_{b2}	-0.11	0			I_{b2}	0.38	0

[a] B3LYP structures.

of the nearest Cr atoms. An examination of the orbitals reveals that there is slightly more electron density (either α or β) present on the p orbitals of the terminal halide atoms. The lower energy s orbitals do not appear to be spin polarized. Also, the lower energy $3s$ and $3p$ orbitals on Cr are not spin polarized. Looking at the Mulliken charges, we see that these clusters are quite covalent in character.

The primary disadvantage of BS-DFT is that the exchange coupling between the metal

centers is overestimated, and the coupled-spin states are overstabilized [53]. Not only this, but we obtained $S \cong 3$ ($\langle S^2 \rangle = 12.09$, 12.20, 12.38, and 12.77) for the singlet states of Cr_2F_4, Cr_2Cl_4, Cr_2Br_4, and Cr_2I_4, respectively. We see that these values are close to those of a septet state and indicate a significant amount of spin contamination, as they should be zero. In light of the BS solutions for the low-spin states of the dimers, CASPT2(8,10) calculations were performed on the lowest energy singlet and nonet structures with their geometry fixed at those obtained from the intensive geometry optimizations. These results are also given in Table 3.7. Not surprisingly, the RHF calculations predict a nonet ground state with the singlet state lying very high in energy. The singlet state's energy drops substantially after the CASSCF(8,10) calculation and lies less than 0.095 eV above the nonet state for all of the dimers. The energy of the singlet state decreases further relative to the nonet state after the CASPT2 calculation and even becomes the minimum for the CrF_2 dimer. We see that the CASPT2 calculations show that the nonet state becomes increasingly more stable going from F to I, which is reflected by the increase in the CASPT2 energy of the singlet state relative to the nonet. This trend is completely the opposite to that obtained from the DFT calculations for Cr_2F_4 to Cr_2Br_4 (see Table 3.7). The nonet states are described reasonably well by a single determinant, as none of them exhibit any multireference behavior. This is not the case for the singlet states. The singlet states for all of the dimers have significant multireference character, and they all consist of greater than 100 major configurations (i.e. |CI-coefficient| > 0.05). It is also apparent that the better the description of the singlet state, the lower in energy it becomes. The CASPT2 calculations predict high-spin ground states for Cr_2Cl_4, Cr_2Br_4, and Cr_2I_4. However, these calculations have been performed at the B3LYP or PW91 optimized distance as they are computationally demanding, and a proper geometry optimization could easily favor the singlet over the nonet state.

3.2.2 Trimers

The next series of clusters which were examined are the trimers. Like the dimers, we followed a similar procedure to locate their global minima. We first began by looking at several possible structures, which are depicted in Figure 3.5. Many of these structures were not chosen randomly, as we took into consideration the geometry of the global minima of the dimers to try to limit the possible structures we need to consider.

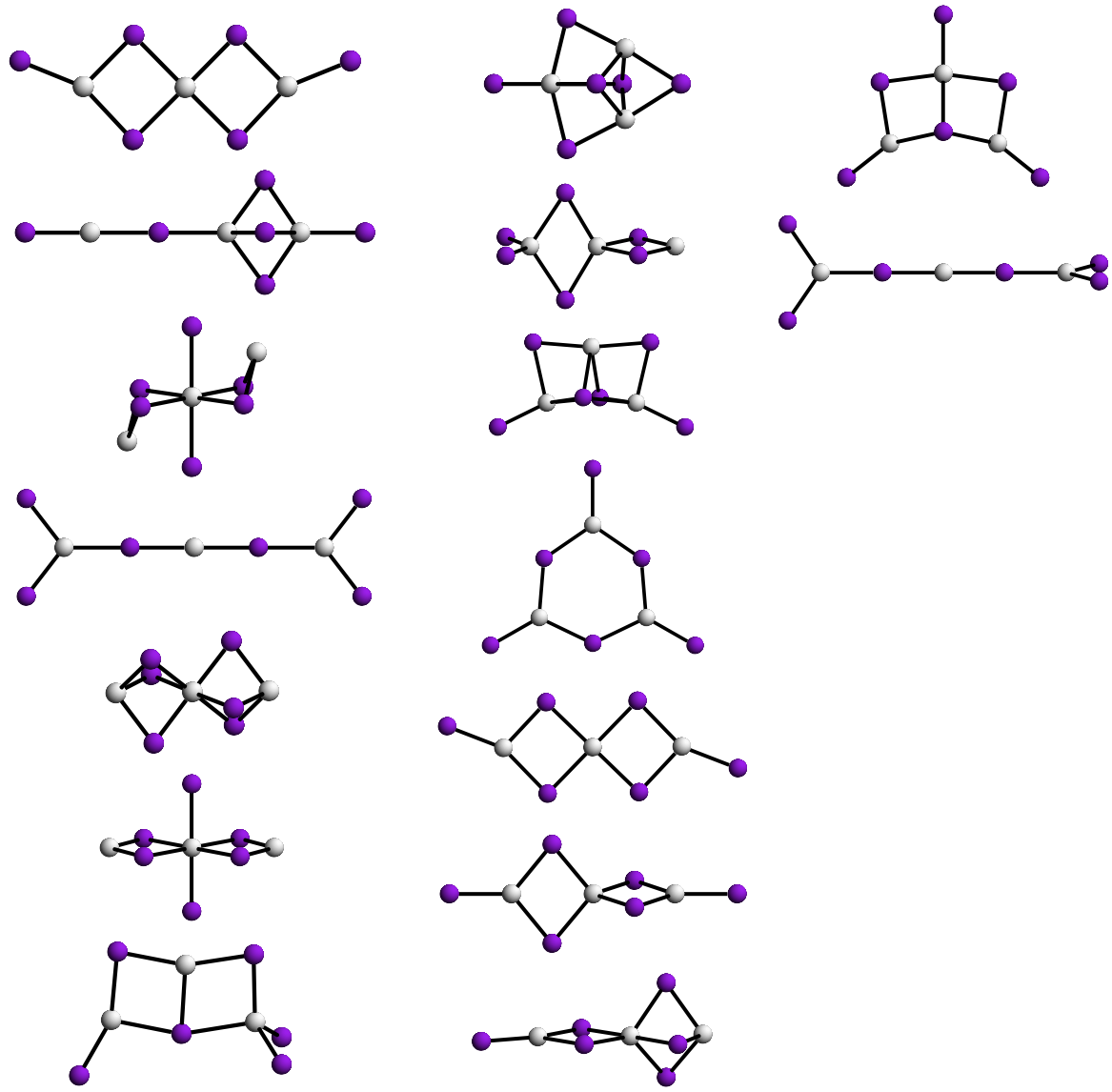

Figure 3.5: Initial trimer structures used in the preliminary analysis.

The trimers can have a total of seven possible spin states: tridecet, undecet, nonet, septet, quintet, triplet, and singlet. However, our findings on the low-energy spin states of the dimers allows us to greatly reduce the number of states we need to consider for any cluster size. We found that the clusters can only consist of high-spin (quintet) monomers. Only the high-spin and low-spin states of the dimers were found to have the lowest energies. All of the intermediate spin states (ones which require at least one monomer to be

in a triplet or singlet state) are much higher in energy and do not pose as candidates for the global minima. These low-energy, high-spin and low-spin states are not just observed in our gas-phase clusters. Similar results were found in the solid state of α-$CrCl_2$ [30], in which the chains along the crystallographic c-axis comprise of high-spin, quintet $CrCl_2$ monomers coupled either anti-ferromagnetically (AFM) or ferromagnetically (FM). Our results allow us to predict the low-energy spin states for *any* cluster size. Therefore, we only need to examine the tridecet and quintet states for the trimer; for the tetramer, we only need to look at the septendecet, nonet, and singlet states.

The resulting structures from our preliminary and intensive geometry optimizations are shown in Figure 3.6, and a comparison of their energies is given in Table 3.10. According to our preliminary analysis, we see that the quintet states for all of the trimers represent the global minima, and the tridecet states all lie slightly higher in energy. For the CrF_2, $CrCl_2$, and $CrBr_2$ trimers, the global minima consist of the quintet state of structure (T1). The situation is different for the CrI_2 trimer, for which the global minimum is the quintet state of (T2). Interestingly, the lowest energy tridecet state for the CrI_2 trimer is structure (T1).

Looking at our intensive geometry optimizations, we see that the global minima for all of the trimers are in the low-spin quintet state, in agreement with our preliminary analysis. There are, again, two major geometries for the global minima. For Cr_3F_6 and Cr_3Cl_6, the global minima consist of the the quintet state of (T1). The quintet state of (T2) is lowest in energy for Cr_3Br_6 and Cr_3I_6, and we observe that this structure becomes more stable going down the halide group. Taking a closer look at the geometry of (T2), we see that this structure consists of three Cr atoms arranged within a trianglular plane and not in a linear fashion like (T1). Within this structure are three monohalide bridges (X_2, X_3, X_4) linking the three Cr atoms (see Figure 3.6). These three halides are not within the plane of the Cr atoms. There are two additional halides (X_5 and X_6) which cap the molecule above and below the plane of the Cr atoms. Interestingly, these two halides are bonded to all three of the Cr atoms and are closer to Cr_2 and Cr_3 than to Cr_1. Lastly, there is a 'terminal' halide (X_1) attached to Cr_1. The tridecet states for all of the C_{2h} structures (T1) lie less than 0.07 eV higher in energy than their quintet states; however, the tridecet states of (T2) are much higher in energy than their quintet states, indicating stronger spin-spin interactions. We also see that the quintet state of (T1) is very close in energy with the global minimum for the $CrBr_2$ trimer.

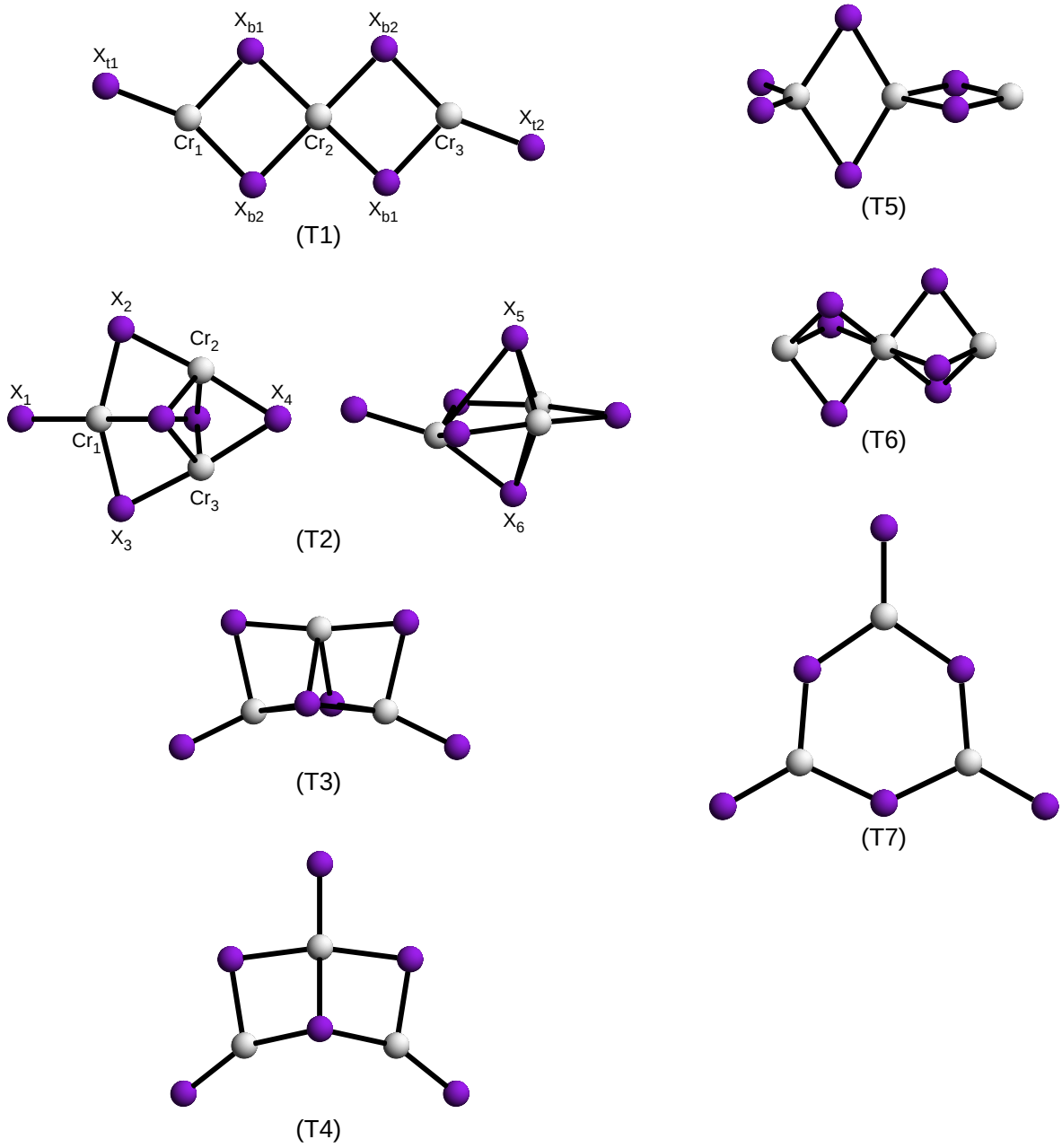

Figure 3.6: Representations of the low-energy minima for the trimers.

Table 3.10: Relative energies among the low energy trimers from various geometry optimizations.

Molecule	Structure	State	ΔE (eV)	ΔE (eV)	ΔE (eV)
Method[a]			PW91/LanL2DZ	B3LYP	
Cr_3F_6	T1	$^{13}A_g$	0.029	0.022	
	T1	$^{5}A_g$	0	0	
	T2	$^{13}A'$	0.900	1.212	
	T2[b]	^{5}A	0.885	1.174	
Method[a]			PW91/LanL2DZ	B3LYP	B3PW91
Cr_3Cl_6	T1	$^{13}A_g$	0.030	0.045	0.045
	T1	$^{5}A_g$	0	0	0
	T2	$^{13}A'$	0.372	0.906	
	T2[b]	^{5}A	0.184	0.741	
	T3	^{13}A	0.540	[c]	
	T3	^{5}A	0.445	[c]	
	T4	^{13}A	0.772	0.945	
	T4	^{5}A	0.768	0.697	
	T7	$^{13}A''$	0.852	0.976	
Method[a]			PW91/LanL2DZ	PW91	
Cr_3Br_6	T1	$^{13}A_g$	0.037	0.150	
	T2	$^{5}A_g$	0	0.084	
	T2	$^{13}A'$	0.241	0.463	
	T2[b]	^{5}A	0.004	0	
	T3	^{13}A	0.448	0.664	
	T3	^{5}A	0.400	[d]	
	T4	^{13}A	0.701	0.801	
	T4	^{5}A	[c]	0.241	
Method[a]			PW91/LanL2DZ	PW91	
Cr_3I_6	T1	$^{13}A_g$	0.081	0.356	
	T1	$^{5}A_g$	0.064	0.308	
	T2	$^{13}A'$	0.087	0.419	
	T2[b]	^{5}A	0	0	
	T3	^{13}A	0.286	0.461	
	T3	^{5}A	0.231	0.494	
	T4	^{13}A	0.629	0.875	
	T4	^{5}A	0.606	0.494	
	T5	^{13}A	0.810	1.209	
	T5	^{5}A	0.966	[d]	
	T6	^{5}A	0.623	[c]	

[a] See computational details for applied basis sets. [b] Slightly distorted structure due to BS-DFT (see text). [c] Optimized to (T1). [d] Optimized to (T2).

Selected geometrical parameters for the trimer global minima are given in Table 3.11. Figure 3.6 shows the atomic labeling schemes used. The geometries of Cr_3F_6 and Cr_3Cl_6 (T1) are very similar to their dimer geometries (see Table 3.8). For Cr_3F_6, the Cr_1-Cr_2 distance is only 0.001 Å shorter than the Cr-Cr distance in the singlet dimer. The Cr_1-Cr_2 distance in Cr_3Cl_6 is closer to that of the nonet dimer rather to that of the singlet. The remaining Cr-X bond lengths within these two trimers are very close to those of the dimers.

There are three different Cr-Cr distances in the Cr_3Br_6 and Cr_3I_6 global minima (T2). The Cr_1-Cr_2 and Cr_1-Cr_3 distances are somewhat similar, with the former being slightly longer. The Cr_2-Cr_3 distances are significantly shorter than any of the Cr-Cr distances calculated so far, 2.462 Å and 2.500 Å for Cr_3Br_6 and Cr_3I_6, respectively. These short distances are indicative of a possible metal-metal bond between the two Cr atoms. We examined the $3d$ orbitals on Cr_2 and Cr_3 and found that there is significant overlap between the orbitals of d_{z^2} symmetry, forming what appears to be a sigma bond. Not only this, but the Wiberg bond indices for Cr_2-Cr_3 are 0.43 and 0.47 for Cr_3Br_6 and Cr_3I_6, respectively. A picture of this orbital overlap from the PW91 calculations for the tridecet state of Cr_3Br_6 is shown in Figure 3.7. Looking at the Cr-X bond lengths within the six-membered ring of (T2), we see that they range from about 2.45–2.57 Å in Cr_3Br_6 and from 2.66–2.77 Å in Cr_3I_6. The Cr_1-X_5 distance is very large (greater than 3.66 Å) for both trimers, and it is significantly longer than Cr_2-X_5 and Cr_3-X_5. The Cr_1-X_6 and Cr_2-X_6 bond lengths are about the same for both trimers, and the Cr_3-X_6 length is somewhat shorter. Interestingly, the Cr_1-X_1 bond length is the shortest of all of the metal-halide bonds within (T2) and is similar in length to the $CrBr_2$ and CrI_2 monomers. We note that looking at the overall structure of (T2), we see that it could consist of one of two possible dimers. The more likely dimer consists of a distorted (D2) structure (i.e. Cr_1, Cr_2, X_1, X_2, X_4, X_6). The other dimer consists of a distorted (D3) structure (i.e. Cr_2, Cr_3, X_2, X_4, X_5, X_6). Structure (D3) was shown to have significantly higher energy than (D2), hence the possibility that (T2) is formed from (D3) is less likely than it being formed from (D2). Both of the quintet trimers are close to C_s symmetry, but there is a slight asymmetry arising from the different Cr_1-Cr_2 and Cr_1-Cr_3 distances, which we will see later that it arises from the BS representation of the quintet spin state. The high-spin tridecet states for (T2) have C_s symmetry for all of the trimers (Table 3.10).

Table 3.11: Geometrical parameters for the trimer global minima obtained from intensive geometry optimizations.

Molecule	State	Parameter	Value[a]	Molecule	State	Parameter	Value[a]
Cr_3F_6	^5A_g	R(Cr_1-Cr_2)	3.015	Cr_3Cl_6[b]	^5A_g	R(Cr_1-Cr_2)	3.390
(T1)		R(Cr_1-F_{t1})	1.806	(T1)		R(Cr_1-Cl_{t1})	2.214
		R(Cr_1-F_{b1})	1.947			R(Cr_1-Cl_{b1})	2.347
		R(Cr_1-F_{b2})	1.974			R(Cr_1-Cl_{b2})	2.366
		R(Cr_2-F_{b1})	1.969			R(Cr_2-Cl_{b1})	2.391
		R(Cr_2-F_{b2})	1.965			R(Cr_2-Cl_{b2})	2.391
		∠(F_{t1}-Cr_1-F_{b1})	124.8			∠(Cl_{t1}-Cr_1-Cl_{b1})	126.6
		∠(F_{t1}-Cr_1-F_{b2})	155.3			∠(Cl_{t1}-Cr_1-Cl_{b2})	143.8
		∠(F_{b1}-Cr_1-F_{b2})	79.9			∠(Cl_{b1}-Cr_1-Cl_{b2})	89.7
		∠(F_{b1}-Cr_2-F_{b2})	79.5			∠(Cl_{b1}-Cr_2-Cl_{b2})	88.1
Cr_3Br_6	^5A	R(Cr_1-Cr_2)	3.091	Cr_3I_6	^5A	R(Cr_1-Cr_2)	3.159
(T2)		R(Cr_1-Cr_3)	2.939	(T2)		R(Cr_1-Cr_3)	3.034
		R(Cr_2-Cr_3)	2.462			R(Cr_1-Cr_3)	2.500
		R(Cr_1-Br_1)	2.365			R(Cr_1-I_1)	2.583
		R(Cr_1-Br_2)	2.573			R(Cr_1-I_2)	2.768
		R(Cr_1-Br_3)	2.547			R(Cr_1-I_3)	2.746
		R(Cr_1-Br_5)	3.664			R(Cr_1-I_5)	3.827
		R(Cr_1-Br_6)	2.603			R(Cr_1-I_6)	2.805
		R(Cr_2-Br_2)	2.450			R(Cr_2-I_2)	2.658
		R(Cr_2-Br_4)	2.511			R(Cr_2-I_4)	2.714
		R(Cr_2-Br_5)	2.519			R(Cr_2-I_5)	2.724
		R(Cr_2-Br_6)	2.715			R(Cr_2-I_6)	2.862
		R(Cr_3-Br_3)	2.451			R(Cr_3-I_3)	2.655
		R(Cr_3-Br_4)	2.520			R(Cr_3-I_4)	2.722
		R(Cr_3-Br_5)	2.520			R(Cr_3-I_5)	2.715
		R(Cr_3-Br_6)	2.589			R(Cr_3-I_6)	2.783
		∠(Cr_1-Br_2-Cr_2)	75.9			∠(Cr_1-I_2-Cr_2)	71.2
		∠(Cr_1-Br_3-Cr_3)	72.0			∠(Cr_1-I_3-Cr_3)	68.3
		∠(Cr_2-Br_4-Cr_3)	58.6			∠(Cr_2-I_4-Cr_3)	54.8

[a] All bond lengths in Å and all bond angles in degrees. [b] B3LYP structure.

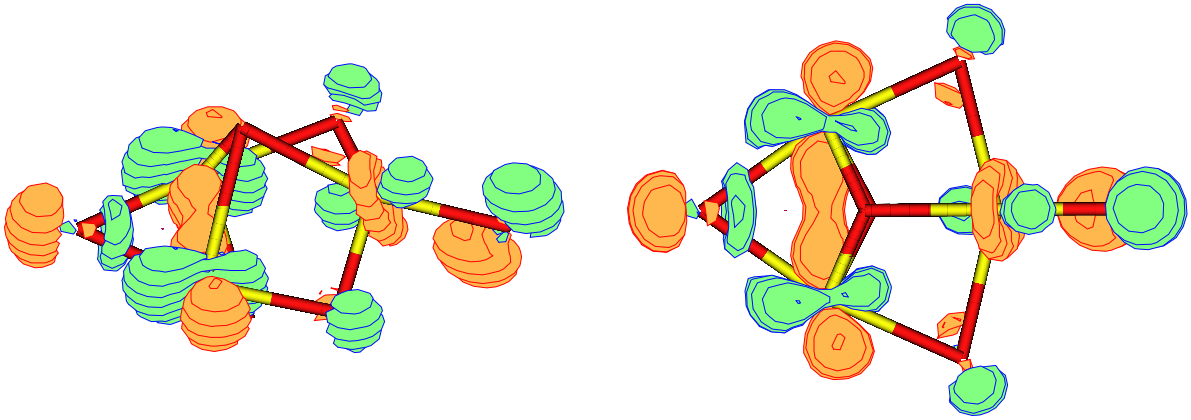

Figure 3.7: Side and top views of the overlap between the d_{z^2} orbitals from Cr_2 and Cr_3 in the tridecet state of Cr_3Br_6.

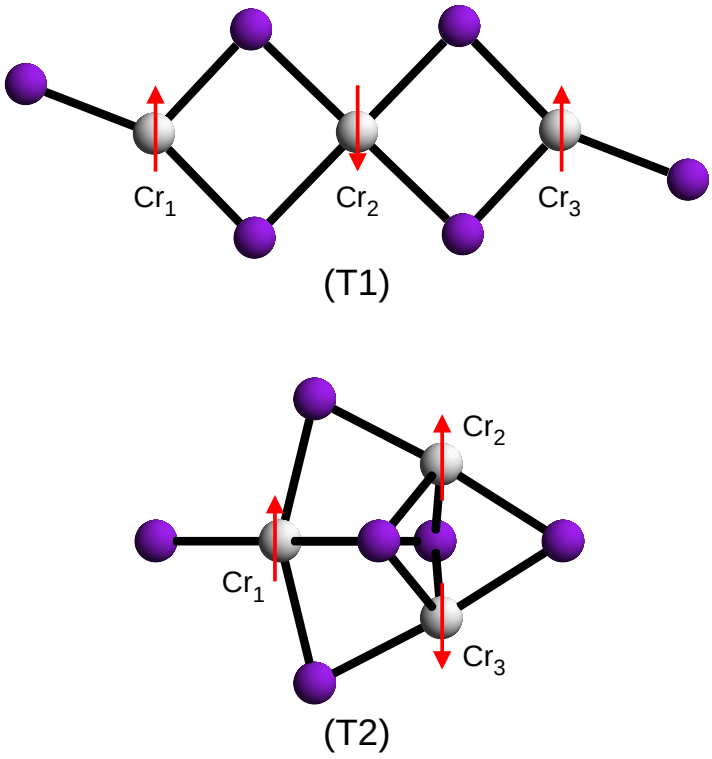

Figure 3.8: BS spin-coupling patterns for the trimer global minima. Each arrow represents four unpaired electrons (S=2).

The BS spin patterns for the quintet global minima of (T1) and (T2) are depicted in Figure 3.8. Starting with (T1), we see that the BS scheme has inversion symmetry. The spins of ($Cr_1Cr_2Cr_3$) consist of a ($4\alpha4\beta4\alpha$) pattern. Trivially, the ($4\beta4\alpha4\beta$) produces the same energy.

The spin pattern for (T2) is slightly more complex as compared to (T1). We see that the BS spin scheme for ($Cr_1Cr_2Cr_3$) is ($4\alpha4\alpha4\beta$). The spin-spin interactions between Cr_1-Cr_2 and Cr_1-Cr_3 are different. A consequence of this is different Cr_1-Cr_2 and Cr_1-Cr_3 bond lengths. To test if the asymmetry is due to the BS representation of the quintet state, we altered the spins such that we had a pattern for ($Cr_1Cr_2Cr_3$) being ($4\beta4\alpha4\beta$). We observed that the energy of the molecule with this new spin pattern was the same as the previous pattern after we reoptimized the structure. After the molecule was reoptimized, the Cr_1-Cr_2 and Cr_1-Cr_3 distances were the opposite to those of the first structure, as one expects (i.e. the Cr_1-Cr_2 and Cr_1-Cr_3 distances in Cr_3Br_6 are 2.94 Å and 3.09 Å in the new structure). More interestingly, we decided to study the spin-spin interactions between Cr_2 and Cr_3. To accomplish this, we changed the spin pattern to ($4\alpha4\beta4\beta$). The energy of this state is now higher by 0.393 and 0.317 eV for Cr_3Br_6 and Cr_3I_6, respectively. We see that these energies are between that of the quintet and tridecet states. These results clearly demonstrate that there are greater spin-spin interactions between the Cr_2 and Cr_3 atoms in (T2) compared to the Cr-Cr interactions in the planar ribbons of (T1).

3.2.3 Tetramers

The final series of clusters examined are the tetramers. Representations of the starting geometries we used are given in Figure 3.9. Of the nine possible spin states for the tetramers, only the septendecet, nonet, and singlet states were examined, as these arise from quintet monomers. In order to keep the number of plausible structures of the tetramers within a manageable limit, many of the starting geometries included dimeric or trimeric minima, as these were shown to be significantly lower in energy than any of the other possible geometries considered for those clusters.

The results of our preliminary and intensive geometry optimizations are given in Table 3.12, and the lowest energy structures are shown in Figure 3.10. According to our preliminary analysis, we see that the global minimum of the CrF_2, $CrCl_2$, and $CrBr_2$ tetramers is the singlet state of (Q1). The nonet state of (Q4) is calculated to be lowest in energy for the CrI_2 tetramer.

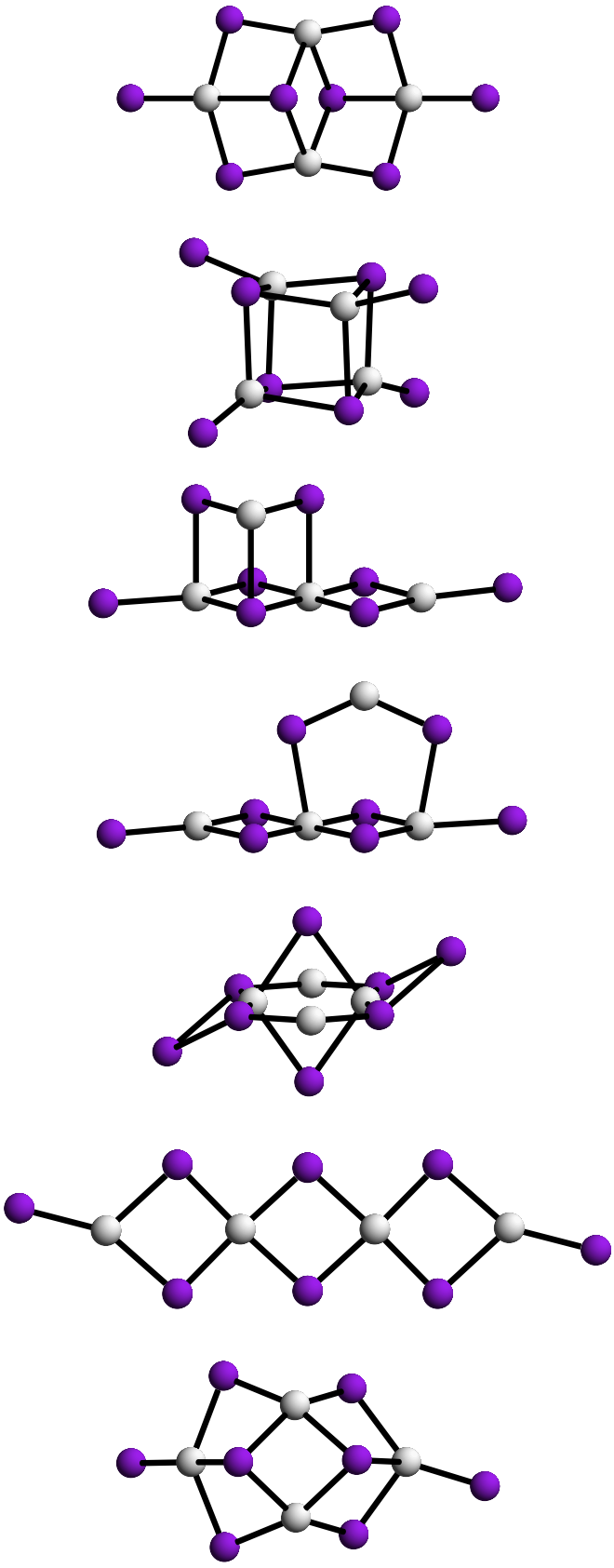

Figure 3.9: Initial tetramer structures used in the preliminary analysis.

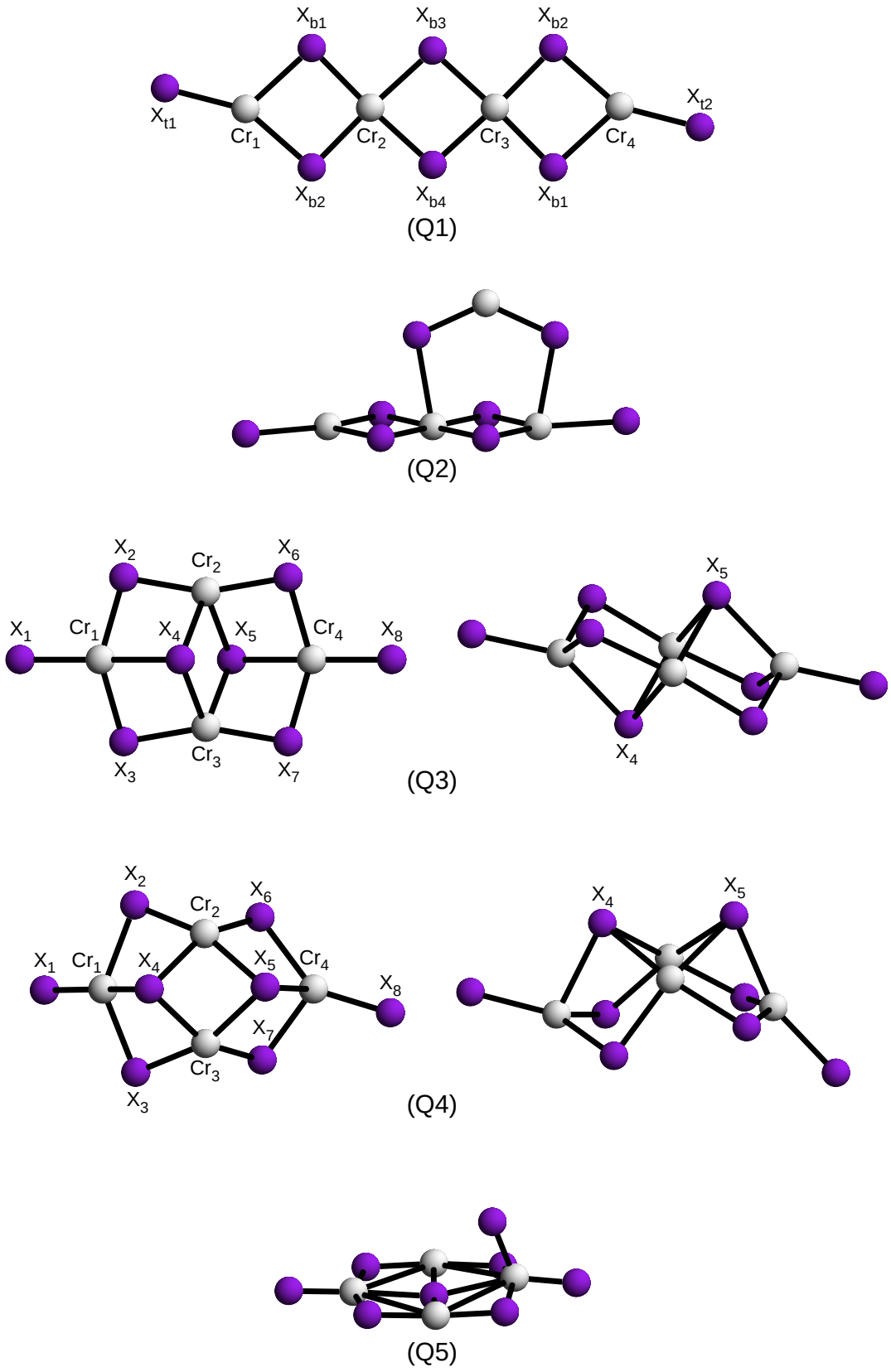

Figure 3.10: Representations of the low-energy minima for the tetramers.

Table 3.12: Relative energies among the low energy tetramers from various geometry optimizations.

Molecule	Structure	State	ΔE (eV)	ΔE (eV)
Method[a]			PW91/LanL2DZ	B3LYP
Cr_4F_8	Q1	$^{17}A_g$	0.059	0.022
	Q1	$^{9}A_g$	0.023	0.015
	Q1	$^{1}A_g$	0	0
	Q3	$^{17}A_g$	0.429	0.926
	Q3[b]	^{9}A	0.331	
	Q4	^{17}A	0.787	1.206
	Q4	^{9}A	0.424	
	Q4	^{1}A	0.618	
	Q5	^{17}A	0.944	2.053
	Q5	^{9}A	0.772	
Method[a]			PW91/LanL2DZ	B3LYP
Cr_4Cl_8	Q1	$^{17}A_g$	0.036	0.048
	Q1	$^{9}A_g$	0.020	0.019
	Q1	$^{1}A_g$	0	0
	Q2	^{17}A	0.611	0.934
	Q2	^{9}A	0.561	
	Q2	^{1}A	0.584	
	Q3	$^{17}A_g$	0.398	0.864
	Q3	$^{1}A_g$	0.327	
	Q4	^{17}A	0.421	0.852
	Q4	^{9}A	0.180	
	Q4	^{1}A	0.284	
Method[a]			PW91/LanL2DZ	PW91
Cr_4Br_8	Q1	$^{17}A_g$	0.028	0.228
	Q1	$^{9}A_g$	0.014	0.166
	Q1	$^{1}A_g$	0	0.124
	Q2	^{17}A	0.508	0.798
	Q2	^{9}A	0.495	
	Q2	^{1}A	0.462	
	Q3	$^{17}A_g$	0.361	0.650
	Q3[b]	^{9}A	0.378	
	Q3	$^{1}A_g$	0.351	
	Q4	^{17}A	0.270	0.454
	Q4	^{9}A	0.207	0
	Q4	^{1}A	0.211	0.131
Method[a]			PW91/LanL2DZ	PW91
Cr_4I_8	Q1	$^{17}A_g$	0.216	0.389
	Q1	$^{9}A_g$	0.205	0.354
	Q1	$^{1}A_g$	0.189	0.332
	Q2	^{17}A	0.469	0.705
	Q2	^{9}A	0.387	0.580
	Q2	^{1}A	0.423	0.662
	Q3	$^{17}A_g$	0.279	0.516
	Q3[b]	^{9}A	0.252	0.024
	Q3	$^{1}A_g$	0.209	0
	Q4	^{17}A	0.214	0.397
	Q4	^{9}A	0	0.161
	Q4	^{1}A	0.098	0.286

[a] See computational details for applied basis sets. [b] Slightly distorted structure due to BS-DFT (see text).

From our more intensive analysis, we obtain three major structures for the global minima. For Cr_4F_8 and Cr_4Cl_8, the lowest energy structure is a continuation of the anti-ferromagnetically coupled planar structure (Q1). The global minimum for Cr_4Br_8 now consists of the nonet state of (Q4), and for Cr_4I_8, the singlet state of (Q3) is now the global minimum. Looking at (Q1) for the CrF_2 and $CrCl_2$ tetramers, we find that the singlet, nonet, and septendecet states are all very close in energy, with the nonet state lying between the singlet and septendecet states in energy. It is interesting to note that the energy difference between the high and low spin states of (D1), (D2), (T1), and (Q1) is almost constant for each dihalide (0.02, 0.05, 0.10, and 0.05 eV for CrF_2, $CrCl_2$, $CrBr_2$, and CrI_2, respectively). The only exception to this pattern is (D1) of Cr_2I_4, in which the singlet and nonet states were only 0.001 eV apart in energy. The apparent convergence between the high and low-spin states' energies for these chains could prove useful in determining the magnetic properties for the solid-state of all of the chromium dihalides, as they all possess these chain-like structures in their crystals. We mention that in our solid-state calculations for α-$CrCl_2$, the energy difference between the FM and AFM states is only 0.016 eV. The resulting spin state for the Cr_4Br_8 global minimum is surprising, as we have predicted singlet global minima for all of the other tetramers, yet the singlet state of (Q4) is 0.131 eV higher in energy than the nonet state. The high-spin state for this structure is 0.454 eV higher in energy. The nonet and septendecet states for (Q3) of Cr_4I_8 are 0.024 and 0.516 eV higher in energy than the global minimum, respectively. Structures (Q3) and (Q4) become more stable going down the halide group.

Taking a closer look at (Q3) and (Q4), we see that neither of them are planar (Figure 3.10). The high-spin and low-spin states of (Q3) have C_i symmetry, and the nonet state has C_1 symmetry but is close to C_i symmetry. We believe that both of these structures come from the (T2) trimer, as there is a strong resemblance between these two tetramers and (T2), Figure 3.6. The primary structural difference between these tetramers is that in (Q3), atoms X_4 and X_5 are *trans* to one another, and in (Q4), they are *cis*.

Selected geometrical parameters for the tetramer global minima are given in Table 3.13. Looking at the Cr_4F_8 and Cr_4Cl_8 global minima, (Q1), we see that we have two different Cr-Cr distances. For both tetramers, Cr_1-Cr_2 is shorter than Cr_2-Cr_3. The difference between the two Cr-Cr distances is small for Cr_4F_8, but for Cr_4Cl_8, the difference is significant (roughly 0.1 Å). In fact, the Cr_2-Cr_3 is longer than any of those for the $CrCl_2$ oligomers.

Table 3.13: Selected geometrical parameters for the tetramer global minima obtained from intensive geometry optimizations.

Molecule	State	Parameter	Value[a]	Molecule	State	Parameter	Value[a]
Cr_4F_8	^1A_g	R(Cr_1-Cr_2)	3.017	Cr_4Cl_8[b]	^1A_g	R(Cr_1-Cr_2)	3.383
(Q1)		R(Cr_2-Cr_3)	3.030	(Q1)		R(Cr_2-Cr_3)	3.480
		R(Cr_1-F_{t1})	1.807			R(Cr_1-Cl_{t1})	2.215
		R(Cr_1-F_{b1})	1.946			R(Cr_1-Cl_{b1})	2.348
		R(Cr_1-F_{b2})	1.972			R(Cr_1-Cl_{b2})	2.364
		∠(F_{t1}-Cr_1-F_{b1})	125.3			∠(Cl_{t1}-Cr_1-Cl_{b1})	126.9
		∠(F_{b1}-Cr_1-F_{b2})	79.9			∠(Cl_{b1}-Cr_1-Cl_{b2})	90.0
Cr_4Br_8	^9A	R(Cr_1-Cr_2)	2.910	Cr_4I_8	^1A_g	R(Cr_1-Cr_2)	2.943
(Q4)		R(Cr_1-Cr_3)	3.097	(Q3)		R(Cr_1-Cr_3)	2.932
		R(Cr_2-Cr_3)	2.592			R(Cr_2-Cr_3)	2.512
		R(Cr_2-Cr_4)	3.533			R(Cr_1-I_1)	2.570
		R(Cr_3-Cr_4)	3.494			R(Cr_1-I_4)	2.725
		R(Cr_1-Br_1)	2.361			R(Cr_2-I_4)	2.780
		R(Cr_4-Br_8)	2.349			R(Cr_3-I_4)	2.742
		R(Cr_1-Br_4)	2.625			R(Cr_2-I_6)	2.653
		R(Cr_2-Br_4)	2.562			R(Cr_3-I_7)	2.686
		R(Cr_3-Br_4)	2.616				
		R(Cr_2-Br_5)	2.545				
		R(Cr_3-Br_5)	2.563				
		R(Cr_4-Br_5)	2.826				
		R(Cr_2-Br_6)	2.465				
		R(Cr_3-Br_7)	2.470				

[a] All bond lengths in Å and all bond angles in degrees. [b] B3LYP result.

We find that with the continuation of the chain-like structure for these two systems, the Cr-X distances among the different oligomers changes very little. Looking at the $CrBr_2$ and CrI_2 tetramer global minima, we find that the Cr_1-Cr_2 and Cr_1-Cr_3 distances between these molecules are similar (around 3 Å). Both of these tetramers contain a metal-metal bond between Cr_2 and Cr_3, given that their distances are 2.592 and 2.512 Å for Cr_4Br_8 and Cr_4I_8, respectively. In the $CrBr_2$ tetramer, Br_4 is bonded to Cr_1, Cr_2, and Cr_3 with

their bond lengths ranging between 2.56–2.63 Å. However, Br_5 is significantly further away from Cr_4, given a bond length of 2.83 Å. In Cr_4I_8, we see that the three Cr-I_4 (and consequently the three Cr-I_5) distances are similar and between 2.72 and 2.78 Å. We note that the Cr_1-X_1 and Cr_4-X_8 bond lengths are the shortest of all of the Cr-X distances for Cr_4Br_8 and Cr_4I_8, and they are similar to their monomers in length.

The BS spin-coupling patterns for the tetramer global minima are shown in Figure 3.11. For the CrF_2 and $CrCl_2$ tetramers, the pattern for ($Cr_1Cr_2Cr_3Cr_4$) consists of ($4\alpha 4\beta 4\beta 4\alpha$). This spin-coupling pattern is very similar to the AFM-II intra-chain spin-coupling scheme we calculated for the solid-state of α-$CrCl_2$ [30]. According to our solid-state calculations on α-$CrCl_2$, we found that this spin-coupling pattern did not produce the lowest energy, as the AFM-I scheme ($4\alpha 4\beta 4\alpha 4\beta \ldots$) produced the lowest energy. We were unable to reproduce the AFM-I scheme for our (Q1) tetramer after several attempts at manipulating the orbitals. A consequence of this spin-coupling scheme is that the Cr_2-Cr_3 distance is longer than Cr_1-Cr_2 or Cr_3-Cr_4 (see Table 3.13).

In the solid-state of α-$CrCl_2$, the spins of the Cr 3*d*-electrons are found to be coupled anti-ferromagnetically with four parallel spins sitting almost exclusively in the *d*-bands of Cr along these chains [121, 122]. However, the energy difference between the anti-ferromagnetic (AFM) and the ferromagnetic phase (FM) is very small with only 0.016 eV [30]. We therefore expect that the low and high spin states are close in energy for the clusters. According to Hund's rule, one expects the high-spin states being more stable than the low-spin states. However, in the solid the AFM state is the ground state [30], which predicts a low-spin singlet state for the dimer and the tetramer, and a quintet state for the trimer. This is indeed the case for our $CrCl_2$ clusters. According to our B3LYP calculations, the global minima consist of the singlet (D1) structure of the dimer, the quintet state of (T1) for the trimer, and the singlet state of (Q1) of the tetramer.

The spin-coupling pattern for the nonet state of Cr_4Br_8 (Q4) is also shown in Figure 3.11. We see that the BS scheme for the nonet state consists of a ($4\alpha 4\alpha 4\beta 4\alpha$) for ($Cr_1Cr_2Cr_3Cr_4$). The spin-coupling pattern for the singlet state of (Q4) is slightly different than that of the nonet. In this state, we have a ($4\alpha 4\beta 4\beta 4\alpha$) pattern for ($Cr_1Cr_2Cr_3Cr_4$). Both the nonet and singlet states of (Q4) have similar geometries, and we believe that the added instability of the singlet state is based on the spin-spin interactions between Cr_2 and Cr_3. To prove this, we look at the septendecet state of (Q4). The septendecet state is 0.454 eV higher in energy than the nonet. The only difference in the spin pattern

between these two states is that in the septendecet state, Cr_3 has 4α spin. Hence, the spin-spin interactions between Cr_2 and Cr_3 is significant, which provides an explanation as to why the singlet state is higher in energy than the nonet state for (Q4).

Looking at the singlet state of the CrI_2 tetramer (Q3), we see that the coupling scheme does not follow the symmetry of the point group (C_i). We have a ($4\alpha4\beta4\alpha4\beta$) pattern for ($Cr_1Cr_2Cr_3Cr_4$). It is interesting to note that the nonet state of (Q3) is only 0.024 eV higher in energy than the singlet. The spin-coupling scheme for the nonet state is ($4\alpha4\beta4\alpha4\alpha$) for ($Cr_1Cr_2Cr_3Cr_4$). Like (Q4), the spin-spin interactions between Cr_2 and Cr_3 is significant, as the septendecet state for (Q3) is 0.516 eV higher in energy than the singlet state.

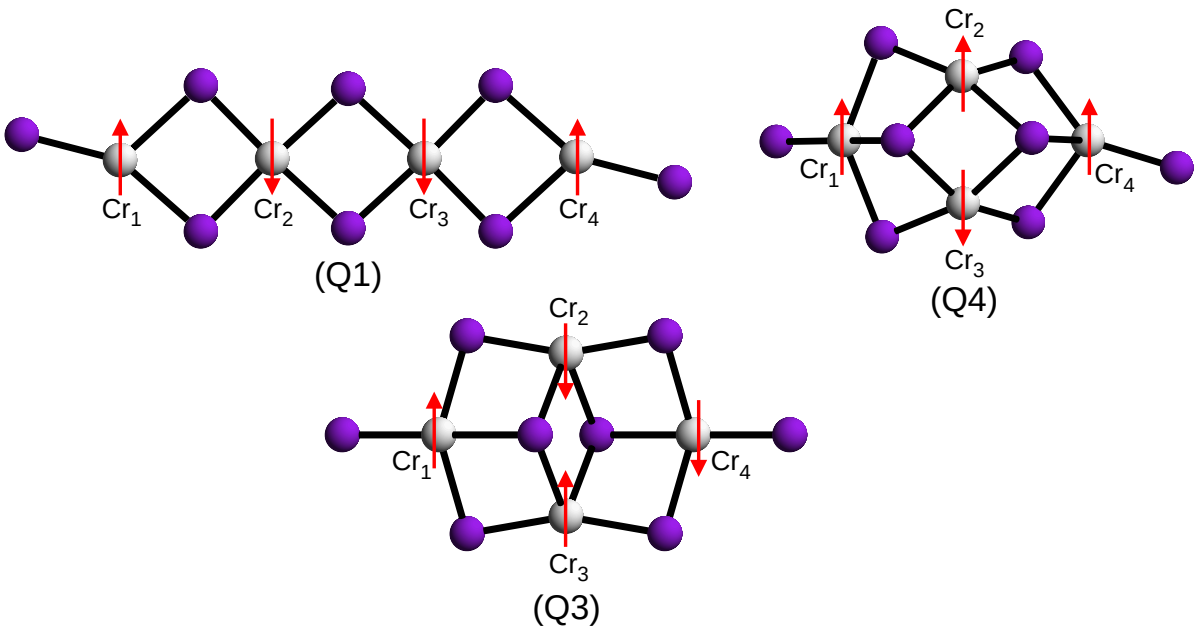

Figure 3.11: BS spin-coupling patterns for the tetramer global minima.

3.2.4 Basis Set Superposition Errors

The basis set superposition errors (BSSE) for all of the global minima were estimated using the counterpoise technique and only including two-body terms. The choice of the two molecules (i.e. monomer and dimer, or monomer and trimer) for which to calculate the BSSE for the planar ribbons was trivial. However, there are several different possibilities in the selection of these two molecules for assessing the BSSE for structures (T2), (Q3),

and (Q4), and all of them must be considered in order to ascertain which produces the largest error. There are also two possible ways to form the tetramers. One of these consists of adding a monomer to the trimer, and the other involves the combination of two dimers. Both of these schemes were considered in our estimation of the BSSE for the tetramers. The results of our BSSE calculations are shown in Table 3.14. We see that for both CrF_2 and $CrCl_2$, the amount of the BSSE is relatively constant for the different oligomers, with their values being between 0.06 and 0.07 eV. The BSSE for the $CrBr_2$ and CrI_2 dimers are also relatively low and comparable with those of the other dimers. Looking at the trimers and tetramers of $CrBr_2$ and CrI_2, we see that the amount of BSSE is slightly higher than their dimers and between 0.1–0.2 eV.

To assess the quality of our basis sets, we need to compare the binding energies of the clusters with our calculated values of the BSSE. The binding energies of the clusters are calculated from the single-point energies of each species in conjunction with the following equations:

$$B_d = E_d - 2E_m \tag{3.5}$$

$$B_{tr} = E_{tr} - E_d - E_m \tag{3.6}$$

$$B_{tet} = E_{tet} - E_{tr} - E_m \tag{3.7}$$

$$B'_{tet} = E_{tet} - 2E_d \tag{3.8}$$

where B is the binding energy, and E_m, E_d, E_{tr}, E_{tet} are the energies of the monomer, dimer, trimer, and tetramer, respectively. A comparison of the BSSE and binding energies is also shown in Table 3.14. We see that, with a couple of exceptions, the binding energies tend to decrease going down the halide group as well as decrease with increasing cluster size. For all of the clusters, the relative amount of the BSSE is quite small and less than 6% of the binding energies. The exception to this is for the tetramer of $CrBr_2$, for which the value approaches 10% when considering the tetramer coming from two dimers.

As mentioned in Chapter 2, the BSSE is responsible for an overestimation of the binding energies due to basis set incompleteness. Hence, we need to apply corrections to the binding energies by adding the calculated BSSE to them, which gives us the counterpoise-corrected energies:

$$E_{cc} = B + E_{BSSE} \tag{3.9}$$

where E_{cc} is the counterpoise-corrected energy, B is the binding energy, and E_{BSSE} is the BSSE energy.

Table 3.14: Calculated BSSE for the oligomer global minima[a].

Molecule	BSSE (eV)	Binding Energy (eV)	% BSSE
Cr_2F_4	0.057	-2.269	2.5
Cr_2Cl_4	0.069	-2.019	3.4
Cr_2Br_4	0.072	-2.011	3.6
Cr_2I_4	0.070	-1.911	3.7
Cr_3F_6	0.057	-2.398	2.4
Cr_3Cl_6	0.069	-1.917	3.6
Cr_3Br_6	0.080	-1.927	4.2
Cr_3I_6	0.097	-2.020	4.8
Cr_4F_8	0.058/0.058	-2.386/-2.515	2.4/2.3
Cr_4Cl_8	0.070/0.069	-1.920/-1.818	3.6/3.8
Cr_4Br_8	0.117/0.177	-1.969/-1.885	5.9/9.4
Cr_4I_8	0.103/0.112	-1.800/-1.909	5.7/5.9

[a] Largest BSSE value listed. For the tetramers, the second value listed is for the combination of two dimers.

We see that the values of E_{cc} will always be slightly more positive than B. Although the contribution of E_{BSSE} to E_{cc} is small, the actual magnitude of E_{BSSE} is comparable to the energy differences between some of the low-energy oligomers, and in several cases, the errors exceed these energy differences (see Tables 3.7, 3.10, 3.12). Therefore, we need to calculate the BSSE for all of the low-lying states which lie within the uncertainty of our global minima. The reasoning behind this can be seen in the following example. The energy difference between the singlet and nonet states of (D1) for Cr_2Cl_4 is 0.054 eV, with their binding energies being -2.019 and -1.965 eV, respectively. After applying the counterpoise-correction, the binding energy of the singlet state increases to -1.950 eV. If the calculated BSSE for the nonet state is less than 0.015 eV, then we cannot say with certainty that the singlet state is indeed the global minimum for Cr_2Cl_4.

Table 3.15 compares the counterpoise-corrected binding energies (E_{cc}) of the low-lying states with our global minima. For the dimers, we do not examine the BSSE between the C_{2v} and C_{2h} structures with the same spin, as their geometries and energies are almost identical. We see that our calculated global minima from the DFT calculations are still lowest in energy after considering the BSSE for the low-energy states. There is

one exception; the nonet state of (D1) for Cr_2I_4 is no longer lowest in energy. The energy difference between the singet and nonet states of Cr_2I_4 from the DFT calculations (0.001 eV) is just too small to ascertain which is lower in energy.

Table 3.15: Comparison of the counterpoise-corrected binding energies of the global minima with other low-lying states.

Molecule	Structure	State	E_{cc} (eV)[a]
Cr_2F_4	D2	^9A_g	-2.203
	D2*	^1A_g	-2.212
Cr_2Cl_4	D1	$^9A_1$	-1.899
	D1*	$^1A_1$	-1.950
Cr_2I_4	D1*	$^9A_1$	-1.841
	D1	$^1A_1$	-1.848
Cr_3F_6	T1	$^{13}A_g$	-2.318
	T1*	^5A_g	-2.341
Cr_3Cl_6	T1	$^{13}A_g$	-1.815
	T1*	^5A_g	-1.848
Cr_4F_8	Q1	$^{17}A_g$	-2.309/-2.437
	Q1	^9A_g	-2.315/-2.444
	Q1*	^1A_g	-2.328/-2.457
Cr_4Cl_8	Q1	$^{17}A_g$	-1.812/-1.704
	Q1	^9A_g	-1.834/-1.734
	Q1*	^1A_g	-1.850/-1.749
Cr_4Br_8	Q1	^9A_g	-1.734/-1.666
	Q1	^1A_g	-1.776/-1.694
	Q4*	^9A	-1.852/-1.708
	Q4	^1A	-1.737/-1.573
Cr_4I_8	Q3	^9A	-1.678/-1.785
	Q3*	^1A_g	-1.697/-1.797

[a] For the tetramers, the second value listed is for the combination of two dimers. * Global minimum from our DFT calculations.

3.2.5 Thermodynamics

CrF_2

Vibrational analyses on the low-energy CrX_2 species were carried out to determine various thermodynamic properties. The calculated dissociation energies at the PW91/LanL2DZ and B3LYP levels of theory for CrF_2 are shown in Table 3.16. The results clearly show that the addition of each CrF_2 unit to the CrF_2 chain brings an almost constant value in energy of about 55 kcal/mol. Somewhat higher energies are obtained with the CASPT2 calculations, as the dissociation for structure (D2) was calculated to be 62.8 kcal/mol. We assume that our dissociation energies are underestimated by our DFT methods by roughly 8 kcal/mol.

Table 3.16: Dissociation energies for the global minima of the (D1), (D2), (T1) and (Q1) CrF_2 clusters for each spin state.

		D1		D2		T1		Q1		
Property[a]	Method	$^1A_1$	$^9A_1$	^1A_g	^9A_g	^5A_g	$^{13}A_g$	^1A_g	^9A_g	$^{17}A_g$
D_e	PW91[b]	52.9	52.4	52.6	52.4	109.5	108.8	165.6	165.1	164.3
	B3LYP	52.3	52.0	52.3	52.1	107.6	107.1	162.6	162.3	162.1
$D_e + ZPVE$	B3LYP	51.8	50.7	51.0	50.8	105.0	104.3	158.6	158.2	158.0

[a] Dissociation energies in kcal/mol. [b] PW91 calculations using the LanL2DZ basis set.

We calculated the values of ΔH, ΔG, and ΔS on the global minima from statistical thermodynamics for the following reactions:

(1) $2CrX_2 \rightarrow Cr_2X_4$
(2) $Cr_2X_4 + CrX_2 \rightarrow Cr_3X_6$
(3) $Cr_3X_6 + CrX_2 \rightarrow Cr_4X_8$
(4) $2Cr_2X_4 \rightarrow Cr_4X_8$

at 298.15 K and from 1000–2000 K. Table 3.17 lists these values at selected temperatures. Our results show that all three thermodynamic properties become more positive with increasing temperature. At 298 K, we see that tetramerization by reaction (4) is the most thermodynamically favored, as its ΔG value is the most negative. At higher temperatures,

the values of ΔG for reactions (1) and (2) are similar, as are the values for reactions (3) and (4). We see that all of the reactions are exothermic, with dimerization being the least and tetramerization via (4) being the most. Interestingly, the ΔH values for (2) and (3) are almost the same at all temperatures studied.

Zasorin et al. performed an ED experiment on CrF_2 at 1520 K [4]. At 1500 K, the values of ΔG for reactions (1)–(4) were 4.3, 4.1, 15.0, and 14.9 kcal/mol, respectively. We used Eq. 2.91 to estimate the equilibrium vapor-phase composition at this temperature, and we calculated that it should consist of approximately 81.1% monomer, 15.7% dimer, and 3.2% trimer.

Table 3.17: Thermodynamic properties for the CrF_2 nucleation according to reactions (1) – (4) in the text.[a]

	Temperature (K)				
Property	298.15	1000	1200	1500	2000
$\Delta H(1)$	-51.1	-48.4	-47.6	-46.4	-44.4
$\Delta G(1)$	-38.7	-13.0	-6.0	4.3	20.9
$\Delta S(1)$	-40.2	-34.4	-34.7	-33.8	-32.6
$\Delta H(2)$	-54.0	-51.3	-50.5	-49.3	-47.3
$\Delta G(2)$	-42.0	-14.1	-6.7	4.1	21.7
$\Delta S(2)$	-41.9	-37.4	-36.5	-35.6	-34.5
$\Delta H(3)$	-53.7	-51.2	-50.3	-49.1	-47.1
$\Delta G(3)$	-39.9	-6.7	2.1	15.0	36.1
$\Delta S(3)$	-46.3	-44.5	-43.7	-42.8	-41.6
$\Delta H(4)$	-56.6	-54.1	-53.3	-52.1	-50.1
$\Delta G(4)$	-43.3	-7.8	1.4	14.9	36.9
$\Delta S(4)$	-48.0	-46.3	-45.6	-44.7	-43.5

[a] ΔH and ΔG in kcal/mol, ΔS in cal/ mol K.

$CrCl_2$

Vibrational analyses were performed on the low-lying $CrCl_2$ states within the same temperature range as CrF_2. The results of our calculated dissociation energies at the

PW91/LanL2DZ, B3LYP, and B3PW91 levels of theory along with the PAW calculations for the infinite chain are shown in Table 3.18. We see that the addition of each $CrCl_2$ unit to the chain brings almost a constant value in energy of about 45 kcal/mol. This is also supported from our PAW calculations where we obtain a cohesive energy of 42.9 kcal/mol per $CrCl_2$ unit for the AFM infinite chain. This compares to 46.4 kcal/mol per unit for the solid, which includes interactions between the $CrCl_2$ chains. Somewhat higher energies are obtained with wavefunction based methods. At the unrestricted (single-reference) MP2 level of theory, we calculate a dissociation energy for structure (D1) of 57.4 kcal/mol for the nonet state. In comparison, at the CASPT2 level we get 54.0 kcal/mol. Hence we assume that the dissociation energies are, again, underestimated by our DFT methods.

Table 3.18: Dissociation energies for the global minima of the (D1), (D2), (T1) and (Q1) $CrCl_2$ clusters for each spin state.

		D1		D2		T1		Q1		
Property	Method	$^1A_1$	$^9A_1$	^1A_g	^9A_g	^5A_g	$^{13}A_g$	^1A_g	^9A_g	$^{17}A_g$
D_e	PW91[b]	47.8	47.2	47.8	47.2	96.1	95.4	143.9	143.4	143.0
	PW91[c]	45.4	45.1	45.6	45.1	87.8	84.2	131.9	-	127.1
	B3LYP	46.6	45.3	46.5	45.2	90.8	89.7	135.0	134.6	133.9
	B3PW91[d]	47.1	46.0	47.0	45.8	92.6	91.6	138.3	137.5	137.1
$D_e + ZPVE$	B3LYP	45.6	44.4	45.6	44.3	88.9	87.8	132.2	131.7	131.1
	B3PW91[d]	46.1	45.0	46.1	44.8	90.7	89.6	135.4	134.6	134.2

[a] Dissociation energies D_e in kcal/mol. [b] PW91 calculations using the LanL2DZ basis set. [c] PW91 calculations using PAW method and plane wave basis sets. [d] cc-pVTZ basis set used for Cl.

We also calculated the value of ΔH^o_{298} for the nucleation reactions (1)–(4) to be -44.4, -42.0, -42.1, and -40.7 kcal/mol, respectively. Based on the ΔH^o_{298} values of sublimation for the monomer to the tetramer from a mass spectrometric study by Ratkovskii et al. [14], we calculated the values of ΔH for the same reactions to be -55±4, -53±5, -56, and -56 kcal/mol at standard conditions, respectively; the tetramer value is only an estimation. Ratkovskii and coworkers also determined the standard enthalpies of dissociation of the dimer, trimer, and tetramer to be 55±4, 109±8, and 156 kcal/mol, respectively. We obtained values of 44.4, 86.4, and 128.5 kcal/mol for the same processes.

Table 3.19: Thermodynamic properties for the $CrCl_2$ nucleation according to reactions (1) – (4) in the text.[a]

	Temperature (K)				
Property[b]	298.15	1000	1200	1500	2000
$\Delta H(1)$	-51.8	-50.1	-49.3	-48.1	-46.1
$\Delta G(1)$	-40.2	-16.9	-10.3	-0.7	14.8
$\Delta S(1)$	-39.0	-33.2	-32.5	-31.6	-30.4
$\Delta H(2)$	-49.5	-47.7	-46.9	-45.7	-43.7
$\Delta G(2)$	-37.9	-12.6	-5.6	4.6	21.7
$\Delta S(2)$	-38.8	-35.1	-34.4	-33.5	-32.4
$\Delta H(3)$	-49.6	-47.8	-47.0	-45.8	-43.8
$\Delta G(3)$	-36.5	-8.7	-1.0	10.0	28.8
$\Delta S(3)$	-43.7	-39.0	-38.3	-37.2	-36.3
$\Delta H(4)$	-50.5	-47.7	-46.9	-45.7	-43.8
$\Delta G(4)$	-27.7	3.1	11.2	23.1	42.5
$\Delta S(4)$	-43.5	-41.0	-40.1	-39.4	-38.2

[a] ΔH and ΔG in kcal/mol, ΔS in cal/ mol K. [b] The ΔH values listed includes the CASPT2 correction for D_e (see text).

Schoonmaker et al. [13] determined the ΔH° value of dissociation of the dimer to be 47.9±3 kcal/mol. We obtained a value of 42.0 kcal/mol. Hence, our ΔH values from the B3LYP calculations for reactions (1) to (4) are all too positive compared to the experimental values. Changing to B3PW91 does not improve this situation significantly. We therefore used our CASPT2 dimerization as a basis to estimate all other dissociation energies. Our approach was the following: first, as each $CrCl_2$ adds almost a constant value, we took the CASPT2 dimerization energy of 54.0 kcal/mol and corrected this by the higher than two-body contributions from our B3LYP calculations. This gives changes in total electronic energies (not including zero-point vibrational energy corrections) of ΔE = -54.0 kcal/mol for reaction (1) as discussed above, -51.7 for reactions (2) and (3), and -50.5 for reaction (4). Next we took the vibrational analysis from our B3LYP calculation and added these to our CASPT2 values. The calculated corrected enthalpies ΔH and free energies ΔG at different temperatures are listed in Table 3.19. The reported ΔH values

are now in much better agreement with experiment, although they might be still a bit low.

We used Eq. 2.91 to estimate the vapor-phase composition of $CrCl_2$ at 1200 K (i.e. approximately the same temperature in which the ED experiment was done in Ref. [3]). We calculate a vapor composition of 39.4% monomer, 51.0% dimer, 9.2% trimer, and 0.4% tetramer. We see that these values are quite different than our calculated vapor composition from the least-squares refinement, in which we estimated a vapor composition of 77% monomer, 19% dimer, and 4% trimer. We see that all of these oligomerization energies do not help us much in trying to estimate, based on the computations, the possible vapor composition at our ED experimental conditions. The vapor decomposion is very sensitive to slight changes in the ΔG values. Moreover, what most likely happens is a sublimation process, during which larger species might evaporate from the solid together with the monomeric molecules. Hence, the estimation of the vapor composition is beyond our present possibilities.

$CrBr_2$

The results of our calculated dissociation energies for the various $CrBr_2$ oligomers at the PW91/LanL2DZ and PW91 levels of theory are shown in Table 3.20. Our results show that the addition of each monomer to the clusters adds approximately a constant value of 45 kcal/mol. This result is interesting, since the global minima for the trimers and tetramers were not the anti-ferromagnetically coupled chains of monomers like CrF_2 or $CrCl_2$, yet we see a nearly constant addition to the dissociation energy. Even more so is the fact that these D_e values are very close to those we obtained for the global minima of the $CrCl_2$ oligomers without the CASPT2 correction. The values of D_e (without zero-point corrections) for the quintet state of (T1) and the singlet state of (Q1) (i.e. the continuation of the anti-ferromangetically coupled chain) was calculated to be 88.9 and 133.4 kcal/mol, respectively. The dissociation energies of the quintet state of (T2) and the nonet state of (Q4) are 1.9 and 2.8 kcal/mol higher than (T1) and (Q1), respectively. Our CASPT2 calculations give a dissociation energy for (D1) of 46.1 kcal/mol, in good agreement with our DFT results.

We calculated the ΔH, ΔG, and ΔS values of the oligomerization reactions (1)–(4), and the results of these calculations are given in Table 3.21. We see that, again, all thermodynamic properties become more positive with increasing temperature. Similar to

Table 3.20: Dissociation energies for the global minima of the (D1), (D2), (T2) and (Q4) $CrBr_2$ clusters for each spin state.

		D1		D2		T2		Q4		
Property[a]	Method	$^1A_1$	$^9A_1$	^1A_g	^9A_g	^5A	$^{13}A'$	^1A	^9A	^{17}A
D_e	PW91[b]	44.3	43.2	44.0	43.2	88.2	82.7	127.3	127.8	126.3
	PW91	46.4	44.1	46.3	44.0	90.8	80.1	133.2	136.2	125.7
$D_e + ZPVE$	PW91	45.6	43.4	45.6	43.2	89.1	78.6	130.7	133.7	123.4

[a] Dissociation energies in kcal/mol. [b] PW91 calculations using the LanL2DZ basis set.

Table 3.21: Thermodynamic properties for the $CrBr_2$ nucleation according to reactions (1) – (4) in the text.[a]

	Temperature (K)				
Property	298.15	1000	1200	1500	2000
$\Delta H(1)$	-45.1	-42.4	-41.6	-40.4	-38.4
$\Delta G(1)$	-34.0	-9.8	-3.4	6.0	21.2
$\Delta S(1)$	-37.2	-32.5	-31.8	-31.0	-29.8
$\Delta H(2)$	-43.3	-40.5	-39.7	-38.5	-36.5
$\Delta G(2)$	-26.8	9.8	19.8	34.5	58.5
$\Delta S(2)$	-55.1	-50.3	-49.5	-49.1	-47.5
$\Delta H(3)$	-44.2	-41.4	-40.6	-39.4	-37.4
$\Delta G(3)$	-31.8	-4.7	2.6	13.3	30.6
$\Delta S(3)$	-41.1	-36.7	-36.0	-35.5	-34.0
$\Delta H(4)$	-42.3	-39.5	-38.7	-37.5	-35.5
$\Delta G(4)$	-24.6	15.0	25.8	41.8	67.9
$\Delta S(4)$	-59.3	-54.5	-53.7	-52.8	-51.7

[a] ΔH and ΔG in kcal/mol, ΔS in cal/ mol K.

$CrCl_2$, reaction (1) is the most exothermic, and the general trend in exothermicity is (1) > (3) > (2) > (4). According to our calculated ΔG values, we see that reaction (1) is the most thermodynamically favorable and (4) is the least favorable. Schoonmaker and

coworkers [13] determined that the value of ΔH° of dissociation for Cr_2Br_4 was 47.0±3 kcal/mol, in good agreement with our PW91 value of 45.1 kcal/mol.

CrI_2

The calculated dissociation energies for the various CrI_2 oligomers are given in Table 3.22. Our results show that the addition of a monomer to each of the clusters adds between 41.6–46.5 kcal/mol.

Table 3.22: Dissociation energies for the global minima of the (D1), (D2), (T2) and (Q3) CrI_2 clusters for each spin state.

		D1		D2		T2		Q3		
Property[a]	Method	$^1A_1$	$^9A_1$	^1A_g	^9A_g	^5A	$^{13}A'$	^1A_g	^9A	$^{17}A_g$
D_e	PW91[b]	41.3	40.8	40.8	40.2	82.6	80.6	121.5	120.5	119.9
	PW91	44.0	44.1	44.0	-	90.6	81.0	132.2	131.6	120.2
$D_e + ZPVE$	PW91	43.3	43.3	43.3	-	89.1	79.5	129.7	129.3	118.4

[a] Dissociation energies in kcal/mol. [b] PW91 calculations using the LanL2DZ basis set.

There is an interesting trend which we observed among the D_e values for the $CrCl_2$, $CrBr_2$, and CrI_2 clusters. Looking at their overall dissociation energies, we see that they are all quite similar (see Tables 3.18 and 3.20). Even more surprising is the fact that among these three systems, we have two different structures for the global minima for the trimers and three for the tetramers.

Our calculated D_e value for the nonet state of (D1) from our CASPT2 calculations is 37.1 kcal/mol - significantly lower than our PW91 value. If we consider the continuation of the anti-ferromagnetically coupled chain of CrI_2 units, we calculate the dissociation energies (without zero-point corrections) for the quintet state of (T1) and the singlet state of (Q1) to be 83.5 and 124.5 kcal/mol, respectively. We see that these values are 7.1 and 7.7 kcal/mol lower than the D_e for the quintet state of (T2) and the singlet state of (Q3), respectively. Hence, structures (T2), (Q3), and (Q4), which contain a Cr-Cr bond, become more stable than the chain-like structures as we go down the halide group, as the values of D_e for the low-spin (T2) and (Q4) structures of $CrBr_2$ were only 1.9 and 2.8 kcal/mol higher than the respective chain-like structures.

Table 3.23: Thermodynamic properties for the CrI_2 nucleation according to reactions (1) – (4) in the text.[a]

	Temperature (K)				
Property	298.15	1000	1200	1500	2000
$\Delta H(1)$	-42.9	-40.1	-39.4	-38.2	-36.2
$\Delta G(1)$	-33.4	-7.9	-1.5	7.8	22.8
$\Delta S(1)$	-31.8	-32.2	-31.5	-30.6	-29.5
$\Delta H(2)$	-45.4	-42.6	-41.8	-40.6	-38.6
$\Delta G(2)$	-29.0	7.8	17.9	32.6	56.8
$\Delta S(2)$	-55.2	-50.5	-49.7	-48.9	-47.7
$\Delta H(3)$	-40.2	-37.5	-36.7	-35.5	-33.6
$\Delta G(3)$	-26.8	4.7	13.1	25.4	45.5
$\Delta S(3)$	-45.1	-42.3	-41.5	-40.7	-39.5
$\Delta H(4)$	-42.7	-40.0	-39.2	-38.0	-36.0
$\Delta G(4)$	-22.3	20.5	32.5	50.3	79.5
$\Delta S(4)$	-68.5	-60.5	-59.8	-58.9	-57.7

[a] ΔH and ΔG in kcal/mol, ΔS in cal/ mol K.

Looking at the dimer D_e values from our CASPT2 calculations from the four chromium dihalides, we see that it decreases going down the halide group. Not only this, but if we also calculate the difference in the CASPT2 dimer D_e values between these four molecules, i.e. (CrF_2 and $CrCl_2$), ($CrCl_2$ and $CrBr_2$), and ($CrBr_2$ and CrI_2) we get 3.3, 5.6, and 9.0 kcal/mol, respectively. We see that there is roughly an increase of 3 kcal/mol in the differences in the dissociation energy for each dimer going from F to I. We see two different patterns emerging between the CASPT2 and DFT results. CASPT2 predicts a steady decrease in the dissociation energies of the chromium dihalide oligomers going down the halide group. Our DFT calculations show that the CrF_2 oligomers have overall the largest dissociation energies; the dissociation energies of the $CrCl_2$ to the CrI_2 oligomers are roughly the same. It is interesting to note that Brewer et al. [123] reported that the ΔH^o values of sublimation for CrF_2, $CrCl_2$, $CrBr_2$, and CrI_2 were 85, 64.8, 63.3, and 62 kcal/mol, respectively; the CrF_2 value was an estimation. We clearly see that the ΔH^o values of sublimation for $CrCl_2$, $CrBr_2$, and CrI_2 are very similar.

We also calculated the thermodynamic properties for nucleation reactions (1)–(4) at various temperatures, the results of which are given in Table 3.23. Of the four reactions, only dimerization has a negative ΔG value above 1000 K, and the general trend in thermodynamic favorability at high temperatures is (1) > (3) > (2) > (4).

3.2.6 Infrared Analysis

The infrared spectra of the gas-phase chromium dihalides are complex, with several peaks arising from the different species present in the vapor. A definite assignment of these peaks is quite difficult because many of them are either weakly absorbing or overlap with vibrations from other oligomers. In this section, we report the calculated vibrational frequencies of the chromium dihalide global minima from the monomer to the trimer. We also compare our results with the available literature data. It should be noted that no experimental IR data could be found for the CrF_2 oligomers and only the results for the monomer are reported.

The calculated frequencies and IR intensities for the monomer, dimer, and trimer global minima from our intensive geometry optimizations are shown in Table 3.24. Starting with the CrF_2 monomer, the most intense peak is from the asymmetric Cr-F stretching frequency (ν_3) located at 716 cm^{-1}. This stretching occurs at lower frequencies for the dimer (649 cm^{-1}) and the trimer (653 cm^{-1}) and corresponds to the asymmetric stretch of the terminal fluorides. The spectrum of the dimer should consist of several other peaks located at roughly 480, 440, 190, and 60 cm^{-1}. The Cr_3F_6 spectrum would have additional peaks around 470, 210, 110, and 45 cm^{-1}.

According to our B3LYP calculations, the IR spectrum of $CrCl_2$ vapor should consist of intense peaks located around 470, 420, and 330 cm^{-1}. The first peak arises from ν_3 of the monomer, with the other two coming from the dimer and trimer. Kobra [8] performed a gas-phase IR analysis of $CrCl_2$ at 950 °C and located a series of broad, intense peaks at 475, 415, and 320 cm^{-1}. He labeled the first peak as ν_3 of the monomer with the two other peaks coming from the dimer or trimer. Kobra also observed two low intensity peaks located at 260 and 235 cm^{-1}. We see that the three intense peaks are in good agreement with our calculated frequencies. The one at 475 cm^{-1} comes exclusively from the monomer, and the peak at 415 cm^{-1} could come from from both the dimer and trimer, as both of these molecules have an intense band within this region. The one at 320 cm^{-1} could, again, have contributions from both the dimer and trimer; there is the

Table 3.24: Vibrational frequencies (in cm^{-1}) and IR intensities (in km mol^{-1}) calculated for the global minima of the different chromium dihalide species.[a]

Molecule	Species	Frequencies and Intensities
CrF_2	Monomer	119(28), 614(56), 716(224)
	Dimer	48(6), 57(31), 81, 136, 190(45), 201, 398, 442(88), 463, 481(132), 649(432), 667
	Trimer	24(3), 44(21), 60, 61, 84(2), 108(18), 130(9), 140, 169, 209(53), 248(1), 368 414(3), 424, 453, 468(87), 482, 495(173), 510(408), 653(381), 659
$CrCl_2$[b]	Monomer	49(15), 349(11), 473(147)
	Dimer	21(8), 23(2), 37, 90, 113, 115(19), 265(8), 282(6), 284, 330(46), 420(293), 433(5)
	Trimer	13(2), 18(7), 23, 29, 29, 90, 92(4), 95(8), 105, 133(18), 144, 213, 261, 281(13) 288, 293(5), 309, 330(191), 350(79), 424(299), 429
$CrBr_2$	Monomer	32(5), 224(4), 376(80)
	Dimer	10, 10(1), 21, 64, 80, 85(5), 168, 180, 240, 274(17), 337(160), 343
	Trimer	22, 54, 71(1), 72, 78(1), 84(1), 89, 104(1), 109, 121(3), 131(1), 138 145, 159(5), 186(1), 198(14), 203(7), 240(23), 281(30), 309(51), 315(42)
CrI_2	Monomer	13(4), 141, 329(58)
	Dimer	14, 16, 38, 52(2), 70, 72, 96(5), 136, 194, 242(17), 279(75), 306
	Trimer	14, 44, 52, 55, 62, 64(1), 68, 78, 85(1), 96, 101, 110(5), 117(1), 135(1) 144(1), 171(8), 187(5), 205(16), 244(21), 262(38), 266(19)

[a] Only non-zero intensities are listed and set in parentheses after the corresponding frequency. [b] B3LYP result.

possibility that the monomer's symmetric stretching frequency at 349 cm^{-1} could also be buried within this peak. In an Ar MI-IR experiment by Hastie et al. [7], several peaks of different intensities were located at 500, 430, 415, 370, 342, 324, 282, 263, 257, 170, and 50 cm^{-1}, and the authors mentioned that they came from the dimer and trimer; several of these frequencies are in good agreement with our calculated values. It is interesting to mention that Konings et al. [10] reported that the ν_3 value for the monomer is at 422 cm^{-1}; we see that this matches one of the frequencies for the dimer from our calculations.

As we have $[4(n-1)+2]$ Cr-X bonds for the $(CrF_2)_n$ and $(CrCl_2)_n$ clusters, we have $(4n-2)$ Cr-X stretching frequencies in the CrX_2 chain. The two highest frequency modes are the symmetric and asymmetric terminal Cr-X_t stretching modes. The coupling

between the symmetric and antisymmetric modes becomes smaller as the chain grows for $CrCl_2$, and the splitting between these two modes become smaller with only 5 cm^{-1} left for the trimer. For CrF_2, the coupling between these two modes decreases to 18 cm^{-1} for the dimer and increases slightly to 24 cm^{-1} for the trimer. The lowest frequencies for all of the $CrCl_2$ (and CrF_2) clusters are the ring puckering, ring twisting, and terminal halide bending modes.

Looking at the data for the $CrBr_2$ species, we expect the IR spectrum to consist of three intense peaks located at approximately 380, 340, and 310 cm^{-1}; the first peak comes from the asymmetric Cr-Br stretching mode of the monomer, and the remaining two come from the dimer and trimer. Kobra [8] studied the gas-phase IR spectrum of $CrBr_3$ and observed that it underwent decomposition to $CrBr_2$ and reacted with Br_2 gas to form $CrBr_4$. He concluded that the asymmetric stretching band from the $CrBr_2$ monomer was at 365 cm^{-1}. Kobra also observed bands at 320, 246, and 200 cm^{-1} and assigned these to the different vibrations from the dimer. We see that our monomer values are in good agreement; the dimer vibration at 320 cm^{-1} agrees reasonably well with our peak at 337 cm^{-1}. However, our data for the dimer does not show any absorptions around 246 or 200 cm^{-1}. Our calculated peak at 274 cm^{-1} is the only one that comes close to the experimental values for the dimer. Looking at the trimer, we see that there are several absorptions around 246 and 200 cm^{-1}. Since this gas-phase IR experiment started with $CrBr_3$ and not from $CrBr_2$, the vapor composition may be complex, and we cannot ascertain whether the peaks at 246 and 200 cm^{-1} come from the trimer or from other species present in the vapor.

The gas-phase IR absorption spectrum of CrI_2 vapor was obtained by Konings and Booij [10]. They observed the asymmetric stretching and bending peaks for the monomer at 319.7 and 37 cm^{-1}, respectively. We see that the asymmetric stretching frequency is in good agreement with our value, and the bending frequency is higher than our calculated value. They also observed three additional bands at 280.9 (intense), 214 (weak), and 88 (weak) cm^{-1}. They concluded that the two bands at 280.9 and 88 came from the dimeric species, and the one at 214 came from the condensed phase. Looking at our calculated frequencies for the dimer, we see an intense band at 279 and a weak band at 96 cm^{-1}, which agree with the experimental data. However, a band at 242 cm^{-1} was not observed in their spectra, and this peak could have been buried underneath the strong absorption band at 280.9 cm^{-1}. Schiefenhövel and coworkers [23] calculated the IR spectra of the

CrI_2 monomer and dimer with LDA. For the monomer, they calculated the frequencies to be at 70, 148, and 345 cm^{-1}, and for the dimer, they calculated the frequencies to be 19, 22, 38, 53, 72, 77, 108, 150, 215, 265, 305, and 336 cm^{-1}. We see that all of their frequencies are higher than our corresponding values.

3.3 Gas-Phase Electron Diffraction Analysis of $CrCl_2$

The experimental and theoretical molecular intensity and radial distribution curves are given in Figures 3.12 and 3.13; the experimental molecular intensities are given in the Appendix. It can be seen that most of the information about the systems present in the vapor is in the first peak, corresponding to the bond lengths. The major component of the vapor, the monomer, has only one Cl$\cdots$Cl nonbonded distance, but the clusters have many strong contributions in this region, even if they are present only in small amounts. Therefore, it is not surprising that depending on the refinement scheme, within a certain interval, different vapor compositions and somewhat different geometrical parameters can give equally good agreement - even if we consider only realistic solutions. Moreover, if we accept the results of the computation about the structure of the clusters, we have altogether eight different Cr-Cl bond lengths within the first peak, differing from each other by about 0.02 Å to 0.20 Å, with their different vibrational amplitudes and different weights depending on their relative amounts.

There is one more uncertainty concerning the ED results. Our computations showed (see Table 3.2) that the symmetric $^5\Pi_g$ saddle point state is only about 0.02–0.09 eV higher in energy than the $^5B_2$ ground state, and this means that molecules in this state may also be present in the vapor phase since the thermal energy of our experiment is more than enough to produce them. Even if the lifetime of these transition-state molecules is short, it might still be much longer than the very fast interaction time of the electron beam and the molecular beam in the experiment (approximately 10^{-18} sec). Even molecules in the $^5\Sigma_g^+$ excited state might be present in the vapor according to some of the computations. The monomers in the $^5\Pi_g$ and $^5\Sigma_g^+$ states are linear and also have somewhat longer bond lengths than the ground state ($^5B_2$) molecule. We tried to include two different monomeric species in the analysis, but this was not successful due to the high correlations. There is also a certain elusiveness concerning the dimeric species which constitutes about 20% of the vapor. The energy difference, for example, between the nonet and singlet dimeric

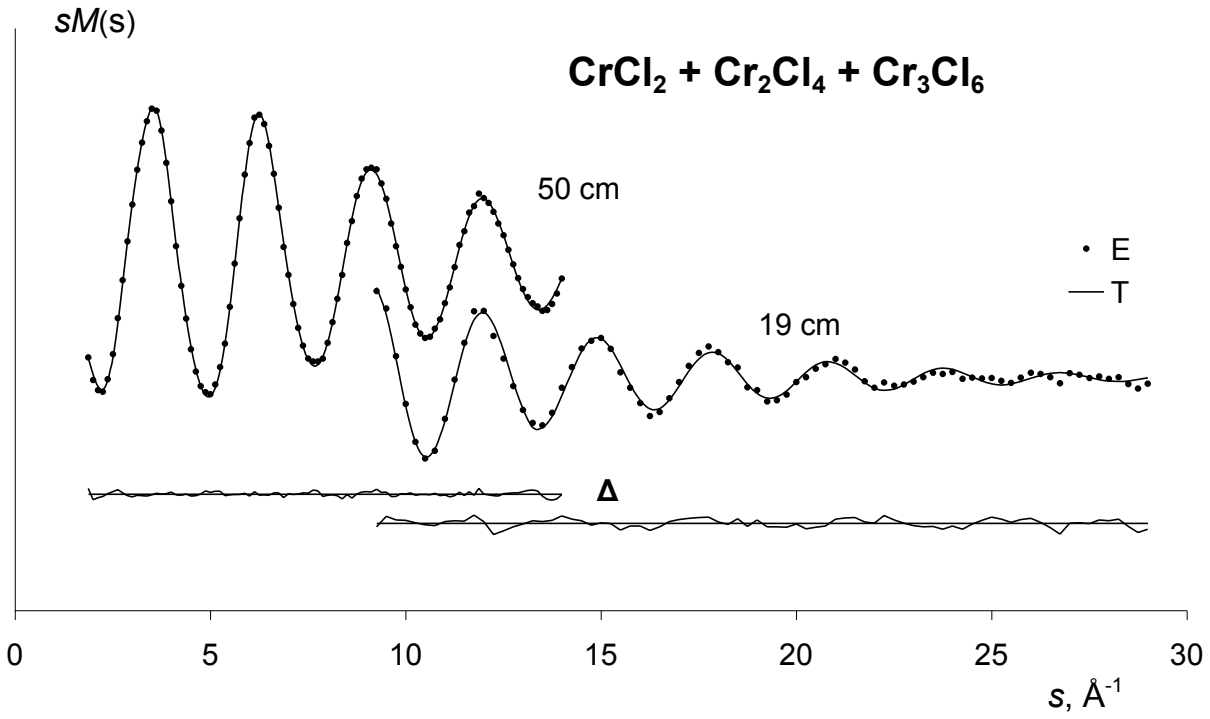

Figure 3.12: Experimental (E, dots) and calculated (T, solid line) electron diffraction molecular intensities for a vapor composition of 77(4)% monomers, 19(4)% dimers, and 4(3)% trimers of chromium dichloride.

structures of C_{2v} symmetry is about 0.024 eV, and the DFT and correlated methods do not even agree on which one is the ground state. These structures differ by several thousandths of an Å in some of their bond lengths. Moreover, the energy difference between the C_{2v} and C_{2h} symmetry dimers is only about 0.001 eV, although their geometries do not differ much. Therefore, in determining the uncertainties of the structural parameters, we have to consider that some structures may be averages of similar molecular species.

The results of the ED analysis of $CrCl_2$ are given in Table 3.25. The thermal average bond length (r_g), 2.214(13) Å, agrees with the previously [3] determined value within their uncertainties. The equilibrium bond length can be estimated from the thermal average value by introducing vibrational corrections.
This process is done by the use of the following equation:

$$r_e^M = r_g - (3/2)al_T^2 \tag{3.10}$$

where a is the Morse parameter and l_T is the vibrational amplitude at temperature T.

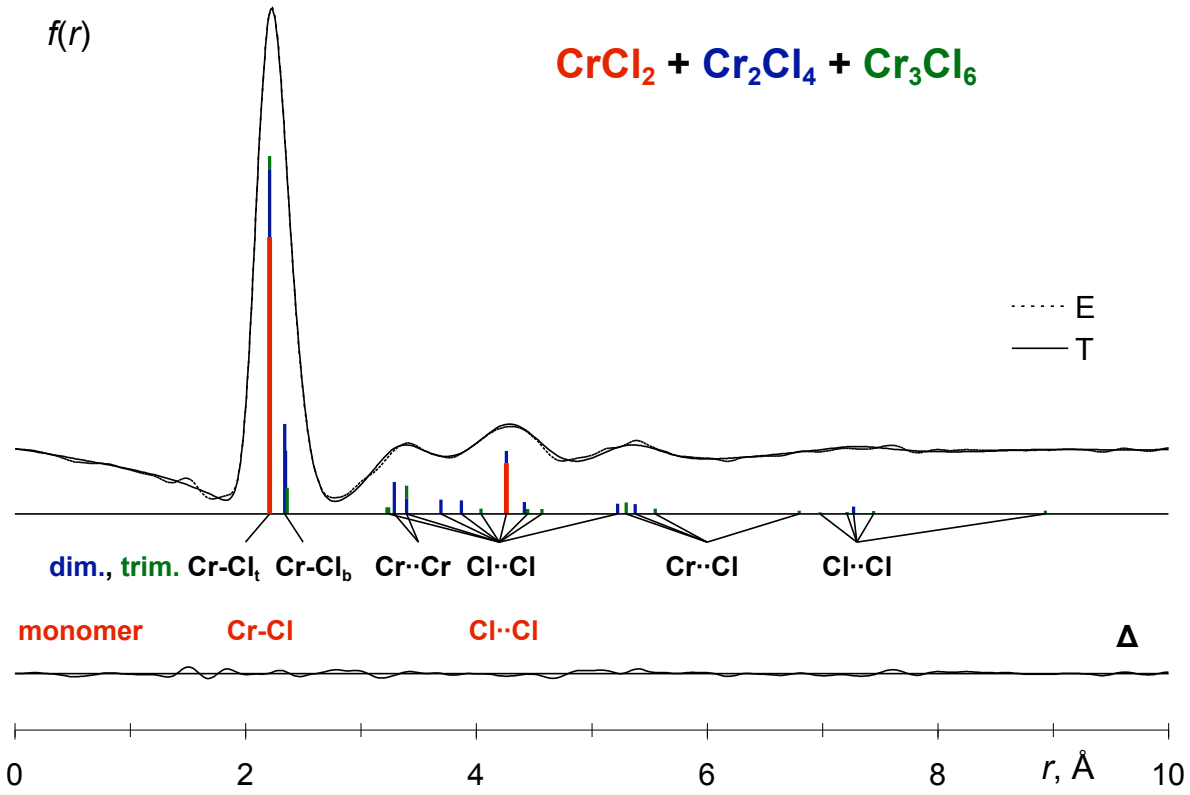

Figure 3.13: Experimental (E, dotted line) and calculated (T, solid line) radial distributions and their differences (Δ) corresponding to the molecular intensities of Figure 3.12. The contributions of different distances are indicated.

As discussed above, the value we determined here depends on several assumptions and thus carries a larger than usual uncertainty. The equilibrium Cr-Cl bond length (r_e^M) of 2.196(20) Å is in agreement with several of our computed values, see Table 3.2. The bond angle from electron diffraction, 149(9.5)°, has an even larger uncertainty, due to the fact that the peak around 4.2 Å on the radial distribution curve has several components from the dimers and trimers, and thus the exact position of the monomer Cl$\cdots$Cl distance is uncertain. Nonetheless, this bond angle does not correspond to a linear molecule, even if taking into account the shrinkage effect. If we assume that due to the high experimental temperature and the small energy difference between the ground state and the $^5\Pi_g$ state the linear transition-state molecules could also be present in the vapor in a smaller amount - and assuming that they had a bond length similar to that of the ground state molecule as

Table 3.25: Geometrical parameters and vapor composition for $CrCl_2$ from electron diffraction.

Parameter	Value
r_g(Cr-Cl)[a], Å	2.214(13)
r_e^M(Cr-Cl)[b], Å	2.196(20)
l(Cr-Cl)[c], Å	0.093(3)
κ(Cr-Cl)[d], Å^3	5.17x10^{-5}
r_g(Cl$\cdots$Cl), Å	4.272(95)
l(Cl$\cdots$Cl), Å	0.216(26)
$\angle_a$ Cl-Cr-Cl, deg.	149(9.5)
Monomer (%)	77.4(4.2)
Dimer (%)	18.7(4.2)
Trimer (%)	3.9(2.8)

[a] The r_g(Cr-Cl) value from Ref. [3] is 2.207(10) Å. [b] Calculated from r_g(Cr-Cl) by anharmonic corrections. [c] Refined in a group with the amplitudes of the dimer and trimer bond lengths. [d] Not refined.

obtained from our calculations (see Table 3.2) - its Cl$\cdots$Cl distance would be only about 0.12 Å longer than that of the ground-state molecule with a 149° bond angle due to the shrinkage effect. This would somewhat decrease the Cl$\cdots$Cl distance and, consequently, the bond angle of the ground-state molecule. The large uncertainty of the bond angle covers this possibility.

The electron diffraction radial distribution curve (Figure 3.13) clearly indicates that there are other species present in the gas phase beside the monomer since for a triatomic molecule, only two peaks corresponding to the Cr-Cl bond distance and the Cl$\cdots$Cl nonbonded distance would be observed. The peak at 3.3 Å contains the Cr$\cdots$Cr and Cl$_b\cdots$Cl$_b$ distances within the rings of the oligomers (Figure 3.13). The monomer Cl$\cdots$Cl distance is in the peak at 4.3 Å, together with several oligomer distances, and the further peaks, at about 5.4 and 7.3 Å, correspond to different longer nonbonded distances of the dimer and trimer molecules. The agreement between the experimental and calculated distribution is very good, demonstrating that the chain-like structures support the experimental data. Pictures of the thermally-averaged dimer and trimer from our least-squares refine-

ment are shown in Figure 3.14. We see that the rings within these thermally-averaged structures are puckered, yet still contain the four-membered ring motif as were found in the computations. We also have to mention that the more general, six-membered ring structure of metal halide trimers (see, for example Ref. [124]) does not agree with the experimental data. In that structure, there are three equal Cr$\cdots$Cr distances in the ring that are situated around 4.0 - 4.1 Å. That would push the monomer Cl$\cdots$Cl distance to the peak at 3.3 Å, resulting in a monomer bond angle smaller than 110 degrees, which would not agree with either of our computations. Even if the trimer amount is about 3% in both types of refinements, due to the large atomic number of Cr and the fact that there are three such distances, its effect is noticeable. Due to the many closely-spaced distances and of the relatively low concentration of the larger species in the vapor, it is not possible to distinguish between their high-spin and low-spin states, or between the C_{2v} and C_{2h} structures of the dimer. Based on our refinement scheme, we predict that the vapor composition consists of 77.4(4.2)% monomer, 18.7(4.2)% dimer, and 3.9(2.8)% trimer.

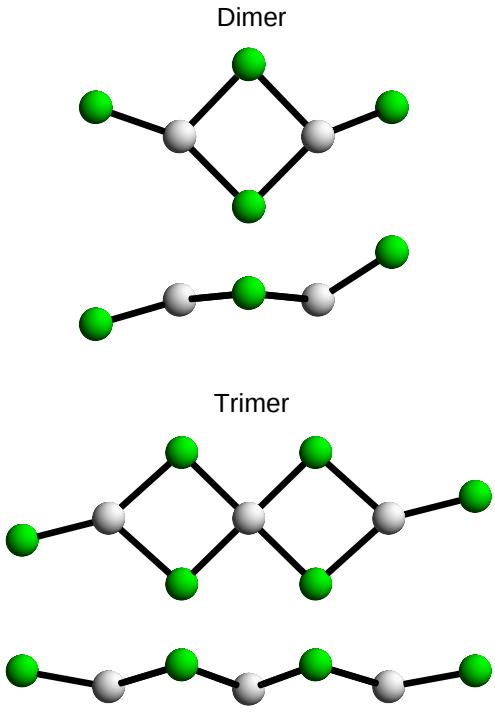

Figure 3.14: Thermal-averaged dimer and trimer structures for $CrCl_2$ from the least-squares analysis. Top and side views are given for each cluster.

3.4 The Solid State of $CrCl_2$

Crystalline α-$CrCl_2$ has an orthorhombic unit cell with $Pnnm$ symmetry [115,116]. CrF_2 and $CrBr_2$ have monoclinic unit cells with $P2_1/n$ and $C2/m$ symmetries, respectively [117,118]. There has been some debate on the crystal structure of CrI_2. Tracy et al. [119] reported a monoclinic unit cell of $C2/m$ symmetry, and Besrest et al. [120] later concluded on an orthorhombic unit cell with $Cmc2_1$ symmetry. Although all of the chromium dihalides possess different crystallographic symmetries, they all have one major structural similarity in common. All of them contain a central chromium atom surrounded by a Jahn-Teller distorted octahedron of halide atoms (similar to cubic close packed geometry). Four of the Cr-X bonds within the plane are all equivalent, and the remaining two Cr-X bonds are elongated. These structures form infinite chains of parallel CrX_2 ribbons which are rotated at some angle to one another. These structure is represented pictorally in Figure 3.15 for α-$CrCl_2$.

Our calculated global minima for the oligomers of CrF_2 and $CrCl_2$ consist of planar, anti-ferromagnetically coupled ribbons of CrX_2 molecules linked together through bridging halide atoms. It is very unusual for these oligomers to have structures which are very similar to that of the solid state. In one of our recent papers [30], we calculated several different properties of the solid state α-$CrCl_2$ from DFT. In α-$CrCl_2$, the ribbons of $CrCl_2$ units align in perpendicular sheets along the crystallographic c-axis. The spins of the Cr $3d$ electrons were experimentally found to be anti-ferromagnetically coupled along these chains [121, 122]. However, there are different possibilities in the spin coupling patterns, and we sought to determine if the coupling scheme occurred via intrachain coupling or interchain coupling (see Figure 3.16). Not only this, but we wanted to determine if GGA (PW91) or LSDA produced a better crystal structure and determined which DFT method best reproduced the experimental spin coupling constants.

According to our results, the anti-ferromagnetic (AFM) coupling scheme is energetically favored over the ferromagnetic (FM) coupling pattern for both PW91 and LSDA crystal structures (Figures 3.16 and 3.17). PW91 produces a very shallow minimum for both coupling schemes, and the binding energy was nearly constant beyond a cell volume of 80 $Å^3$. The PW91 functional with AFM-I coupling produces a slightly under-bonded structure, with the a and b lattice constants overestimated by roughly 5%. LSDA exhibits an overbinding effect perpendicular to the c-axis and produces a theoretical cell volume that is 17% smaller than the experimental cell volume. The Cr-Cl bond lengths within

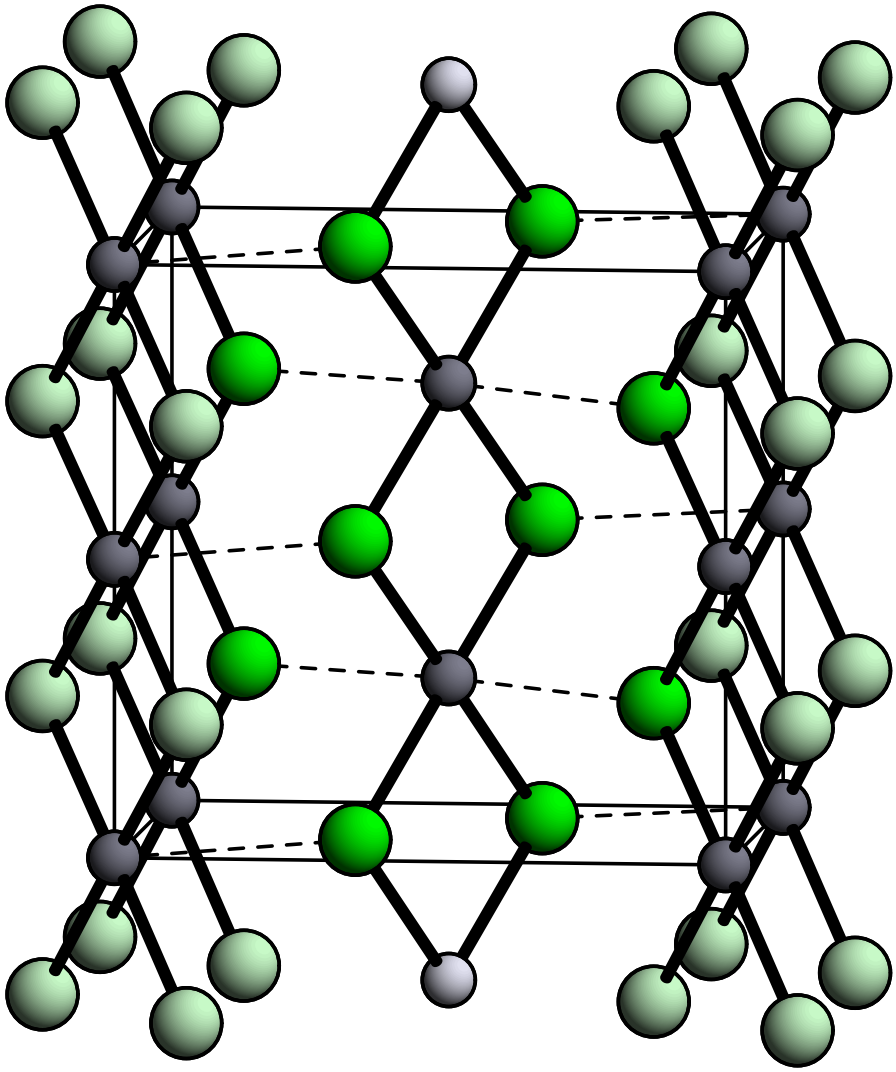

Figure 3.15: Magnetic unit cell of the anti-ferromagnetically coupled α-$CrCl_2$. Green/large (grey/small) spheres represent Cl(Cr) atoms. Dashed lines indicate elongated octahedral bonds. Figure obtained from Ref. [30].

the molecular ribbons are very similar to those that we obtained from the B3LYP gas phase calculations. A comparison of the Cr-Cl bond lengths from our solid state calculations with our gas-phase data is given in Table 3.4. Both the FM and AFM-I schemes from our

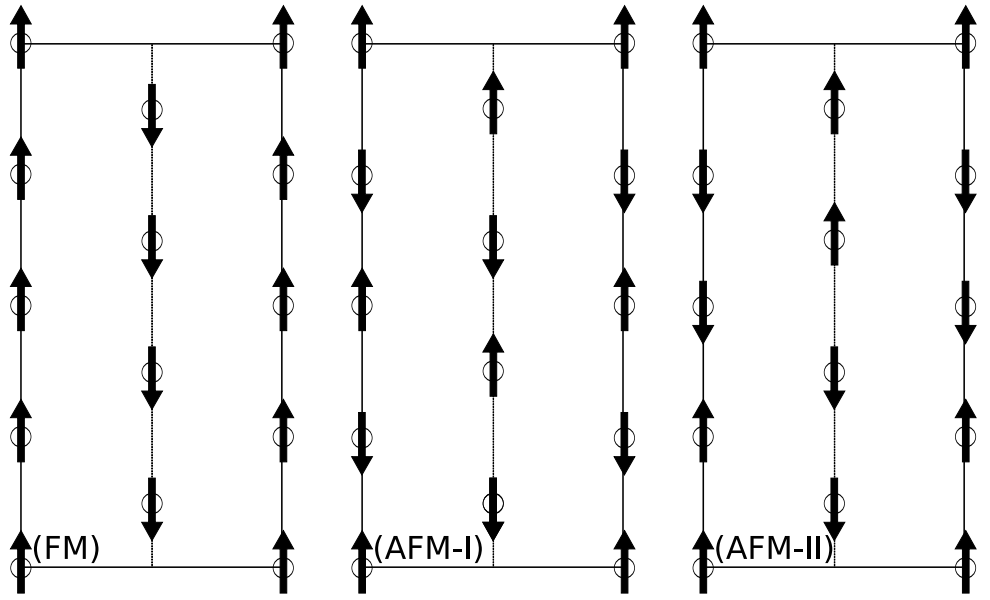

Figure 3.16: Different intra and interchain coupling schemes examined for α-$CrCl_2$. Figure obtained from Ref. [30].

PW91 calculations reproduce the experimental ribbon structures reasonably well. As expected, the overbinding effects from LSDA produce bond lengths that are slightly too short. We found that the intrachain Cr-Cl bond length changes very little in the coupled and uncoupled schemes, and this same effect is observed in our gas-phase calculations for all of the $CrCl_2$ clusters (i.e. high spin and low spin states have almost identical geometries). Our gas-phase Cr-Cl bond lengths for the bridging halides agree very well with our PW91 solid state results as well as those from Oswald and coworkers.

Given that we are able to accurately reproduce the crystal structure for α-$CrCl_2$, our next goal is to reproduce the experimental spin coupling constants among the Cr $3d$ orbitals. Crystalline α-$CrCl_2$ was found to be a $S = 2$ Heisenberg antiferromagnet. The chainlike structure would be easily described by the Heisenberg Hamiltonian

$$H_H = -2J \sum_{c,i} \mathbf{S}_i \mathbf{S}_{i+1} - 2J' \sum_{c,i} \sum_{c',i'} \mathbf{S}_i \mathbf{S}_{i'+1} \tag{3.11}$$

taking into account intra- and interchain next neighbor coupling, J and J', respectively. The first sum in Eq. 3.11 runs over all spins i in each chain c, and the second sum runs

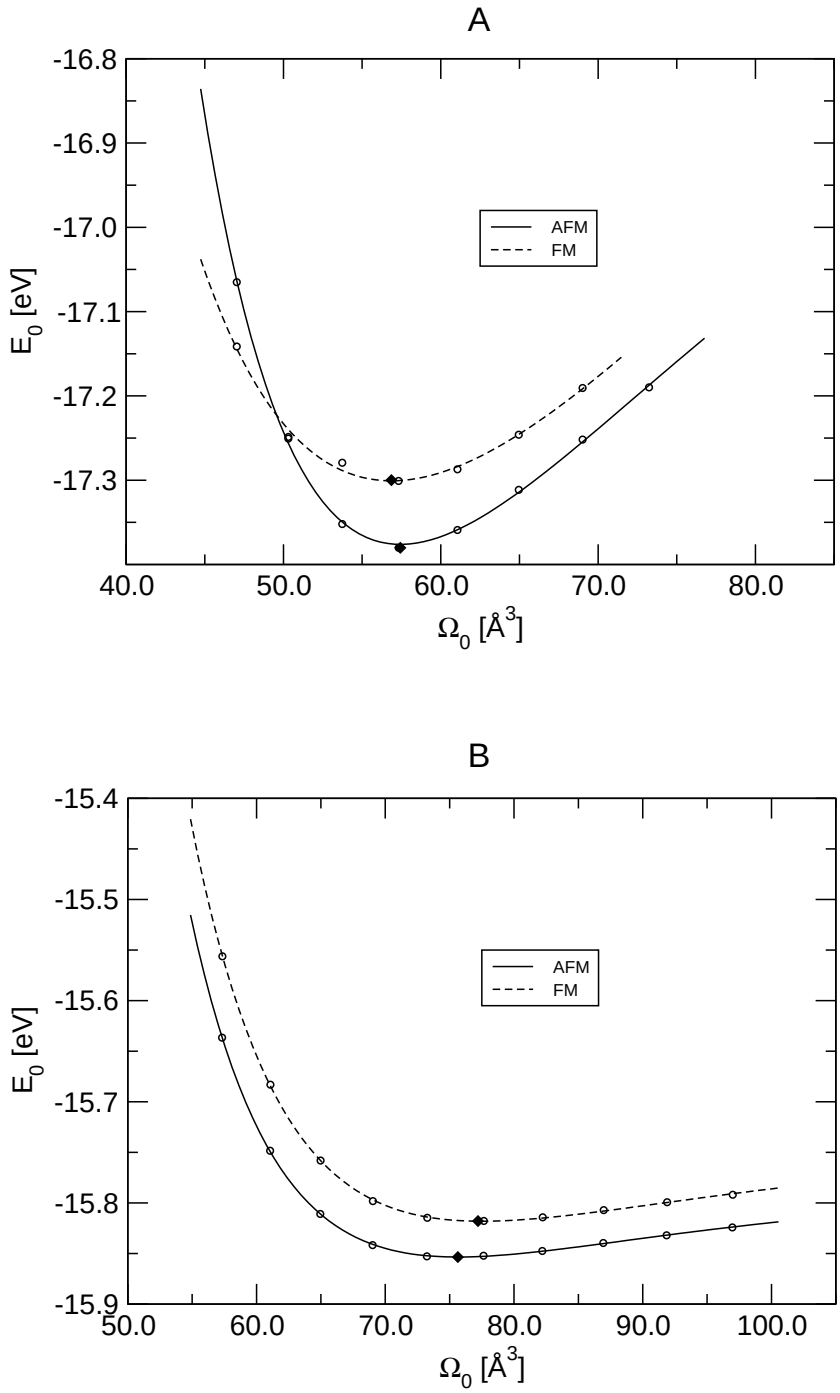

Figure 3.17: $E(\Omega_o)$-curves. Circles: data points, lines: Vinet-fit, diamonds: parameters of final structure. (A) is the LSDA result. (B) is the PW91 result. E_o: binding energy per $CrCl_2$ unit, Ω_o: unit cell volume per $CrCl_2$ unit. Figure obtained from Ref. [30].

Table 3.26: Comparison of the intrachain Cr-Cl bond lengths from crystalline α-$CrCl_2$ with our gas-phase structures. Bond lengths listed are in Å.

Method	R (Cr-Cl)
Tracy et al.[a]	2.40
Oswald[b]	2.37
FM, PW91	2.36
FM, LSDA	2.32
AFM-I, PW91	2.36
AFM-I, LSDA	2.34
Gas-phase B3LYP	2.354, 2.373[c]

[a] Ref. [116]. [b] Ref. [115]. [c] Bridging Cr-Cl distances for the $CrCl_2$ dimer global minimum from Figure 3.8.

over all spins within the adjacent chains c, c'. With the exception of the high-spin FM state, all solutions to the spin-unrestricted DFT or UHF equations used by us are not eigenfunctions of the Heisenberg Hamiltonian [57]. Therefore, we can work with the Ising Hamiltonian

$$H_I = -2J \sum_{c,i} S_{z,i} S_{z,i+1} - 2J' \sum_{c,i} \sum_{c',i'} S_{z,i} S_{z',i'} \tag{3.12}$$

and fit the first-principles energies for three different magnetic coupling schemes to respective expectation values H_I to obtain J and J'. These three different coupling schemes, which are labeled as FM, AFM-I, and AFM-II, are depicted in Figure 3.16. AFM-I was calculated to be the magnetic ground state. For these states, we are able to calculate their energies

$$E_{FM} = -2JS^2 + 8J'S^2 + E_o \tag{3.13}$$

$$E_{AFM-I} = 2JS^2 + E_o \tag{3.14}$$

$$E_{AFM-II} = -4J'S^2 + E_o \tag{3.15}$$

per spin S_i, where we also introduced the nonmagnetic contributions E_o to the binding energy. Thus, we obtained J and J' by

$$J = \frac{1}{8S^2}(E_{FM} + 3E_{AFM-I} - 2E_{AFM-II}) \tag{3.16}$$

$$J' = \frac{1}{16S^2}(E_{FM} + E_{AFM-I} - 2E_{AFM-II}) \tag{3.17}$$

The values of E_{FM}, E_{AFM-I}, and E_{AFM-II} are calculated using the experimental cell coordinates as well as our optimized structures.

The results of our spin-coupling calculations for solid-state α-$CrCl_2$ are given in Table 3.4 along with the experimental values. Also at the experimental geometry, we utilize the PBE exchange-correlation functional [42] and a combination of LSDA with on-site Coulomb repulsion (LSDA+U) [28]. In the LSDA+U theory, we chose $U + J = 3.8$ eV, which gave the best agreement with the spin-coupling constant, J. For all methods, we reproduce the antiferromagnetic character of α-$CrCl_2$ such that $J < 0$. We also find that $J' > 0$ and that $|J'| < |J|$. However, our calculated values of J are more than double the experimental value, with the exception of the fitted LSDA+U value. We also obtain even worse results for the J' values. Using the optimized geometries for PW91 and LSDA gave no improvements for the results. We also note that the values of J and J' change very little for our PW91 results from both the experimental and optimized geometries.

Table 3.27: Spin coupling constants for α-$CrCl_2$, calculated at experimental and theoretical geometries.

Geometry	Method	$J(k_BK^{-1})$	$J'(k_BK^{-1})$
Experimental	Literature[a]	-9.5	1.23
	LSDA	-23.9	2.68
	PW91	-19.4	3.08
	PBE	-18.0	3.62
	PBE0	-37.9	-11.19
	LSDA+U	-9.6	1.46
Optimized	LSDA	-49.5	4.32
	PW91	-19.8	3.08

[a] Ref. [115]

DFT typically fails to describe magnetic interactions for strongly correlated systems [29, 125]. This deficiency arises from the self-interaction energy. It can be partially overcome by explicitly correcting for the electronic self-interaction [126, 127] or by including some of the exact exchange in the exchange-correlation functional [128]. Perdew et al. argued for an exact exchange mixing coefficient $a = 0.25$ from coupling-constant integration [129] and the according extension (PBE0) of the PBE exchange-correlation

functional [54], which has given improved magnetic coupling parameters [130]. We preform exact exchange calculations with variable mixing a around $a = 0.25$ (see Figure 3.18 for results). A value of $a = 1.0$ would give 100% of the Hartree-Fock exchange energy. The strong dependence of J and J' on the value of a can be stated, however, in contrast to other studies including the exact exchange does not improve the agreement with experimental data. Both J and J' are negative around $a = 0.25$, suggesting an anti-ferromagnetic interchain coupling and thus a positive ratio J/J', in contrast to the experiment.

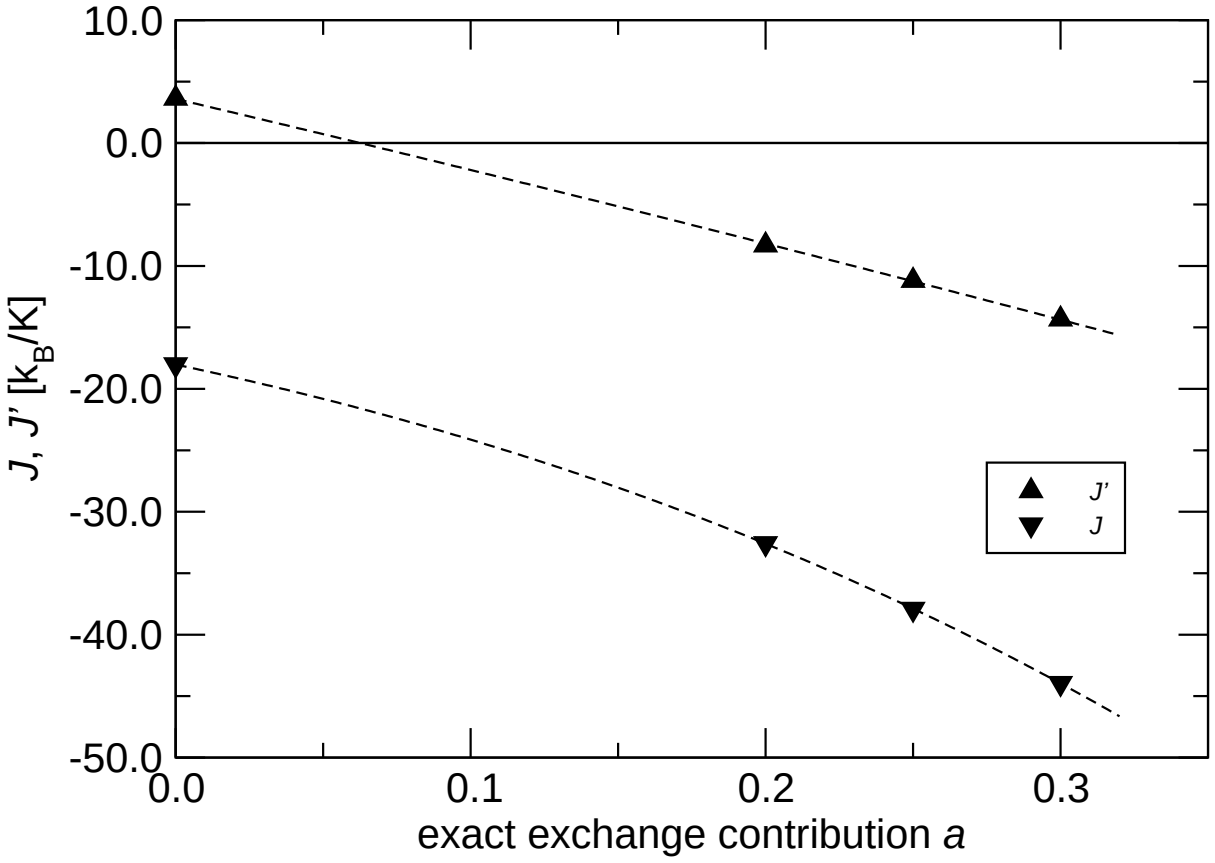

Figure 3.18: Magnetic coupling constants J, J' from hybrid-DFT calculations, varying the exact exchange mixing coefficient a. Figure obtained from Ref. [30]

Chapter 4

Trends among the Chromium Dihalides

In Chapter 3, we found that many of the properties of the different chromium dihalides were quite similar. For example, the ground electronic state of all of the monomers is the $^5B_2$ state, arising from the Renner-Teller distorted $^5\Pi_g$ state - leading to bent structures for all of them. We also discovered that all of the lowest energy dimers consisted of a planar, anti-ferromagnetically coupled, dihalide bridged structure of either C_{2v} or C_{2h} symmetry. All of the dimers with D_{2h} symmetry represented second-order saddle points with imaginary bending modes of the terminal halides going to either *cis* (C_{2v}) or *trans* (C_{2h}) structures. There are several more interesting trends among the properties of the chromium dihalide species which we discovered from our calculations, which are reported in this chapter.

Beginning with the monomers, we looked at the chromium-halide bond lengths in their ground states (from our DFT calculations) and compared them with the experimental gas-phase data along with the solid-state (where available). We also compared the X-Cr-X bond angles for the different monomers in the $^5B_2$ ground states. The results of these analyses are shown in Figure 4.1. Not surprisingly, our calculations show that there is a steady increase in the Cr-X bond length going down the halide group, which is supported by the experimental gas-phase data. Going from $CrCl_2$ to $CrBr_2$, we see that the Cr-X bond length changes the least. A similar trend is also found in the intrachain as well the interchain Cr-X bonds in the crystals. Looking at the bond angles, we see that they increase with the increasing size of the halide.

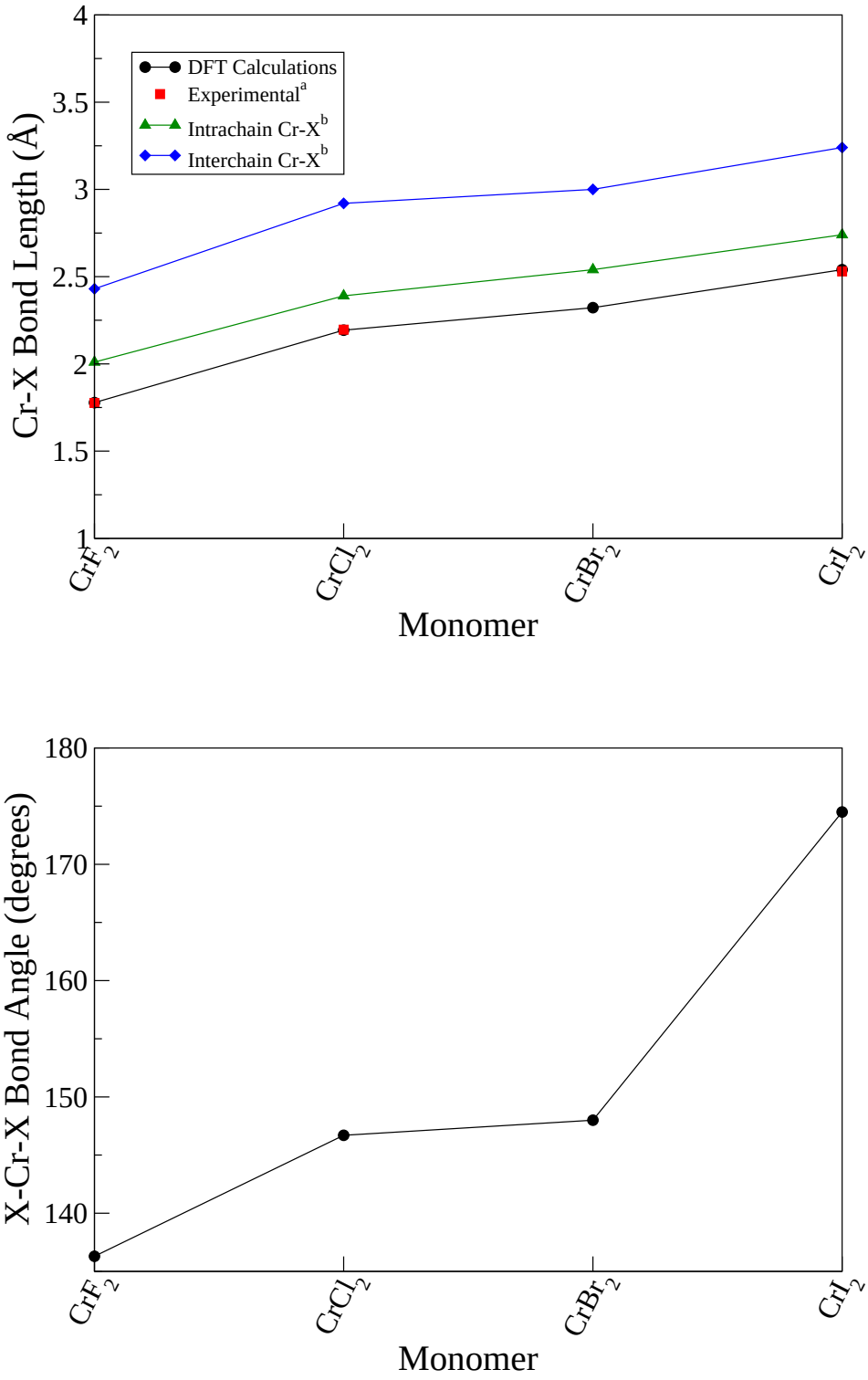

Figure 4.1: Comparison of the Cr-X bond lengths and angles among the different monomers. [a] CrF_2: ED result from Ref. [4], $CrCl_2$: from our ED analysis, CrI_2: estimated value from Ref. [10]. [b] Solid-state intra- and interchain Cr-X distances from Refs. [116–119].

This trend is not linear, as there is a large difference in the bond angle (roughly 25°) between $CrBr_2$ and CrI_2. Interestingly, the bond angles of $CrCl_2$ and $CrBr_2$ are almost the same.

Looking at the dimers in the singlet states, there are some interesting properties among the Mulliken spin densities of the Cr atoms and the Cr-Cr distances. These trends are represented in Figure 4.2. For the Mulliken spin density, we only report the α spin value. We see that the Cr-Cr distance tends to increase with the increasing size of the halides, with the exception being Cr_2Br_4, as this distance slightly smaller than Cr_2Cl_4. The Mulliken spin density on the Cr atoms increases almost linearly going down the halide group and varies between 3.9 for Cr_2F_4 to 4.2 for Cr_2I_4, which is consistent with the decreasing electronegativity from F to I. We also report that the overall spin density on the terminal halides increases from 0.01 for fluorine to 0.17 for I. The spins of the bridging halides change very little and are always close to zero.

All of the chromium dihalides have different crystallographic symmetries, yet they all have one structural similarity in common, which is that they all contain planar dihalide bridged structures which are rotated at some angle to one another. For CrF_2 and $CrCl_2$, these planar, anti-ferromagnetically coupled structures were the global minima for the dimer to the tetramer. For $CrBr_2$ and CrI_2, these structures were lowest in energy only for their dimers. It was seen that as the length of the ribbon increased (i.e. going from the dimer to the tetramer), the change in the geometry decreased. To see how the intrachain Cr-X distances for the larger clusters compare with those of the experimental solid-state, we looked at the average Cr_1-X_b distances in the dimers and the average Cr_2-X_b distances in the trimers and tetramers. A plot of these bond lengths for the dimer to the tetramer for the anti-ferromagnetically coupled ribbons [(D1), (T1), (Q1)] is shown in Figure 4.3; the intrachain Cr-X distances in the solid state are given for comparison. We see that all of the gas-phase Cr-X_b distances in the clusters converge nicely to their solid-state values, though a majority of them are slightly shorter than the experimental values. This is expected, as the solid-state structures also include interchain interactions. The absolute differences in the Cr-X_b bond lengths between the solid-state and Cr_4F_8, Cr_4Cl_8, Cr_4Br_8, and Cr_4I_8 are 0.66%, 0.08%, 1.26%, and 0.66%, respectively.

In our analysis of the dissociation energies of the low-energy oligomers, we saw that CrF_2 had the highest of the dissociation energies. One would logically predict that the

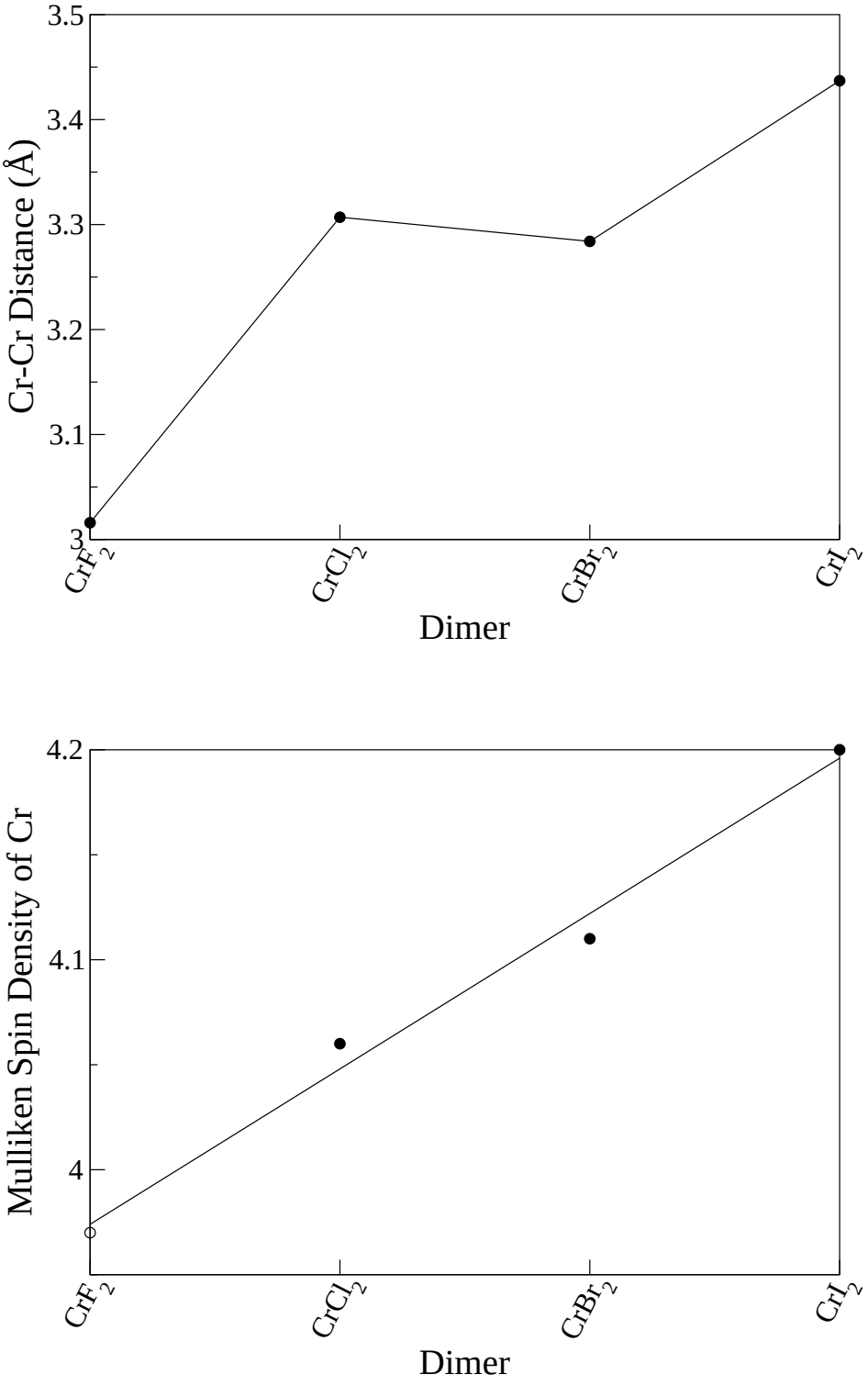

Figure 4.2: Comparison of the Cr-Cr distances and Mulliken spin densities for the singlet state dimers from DFT calculations.

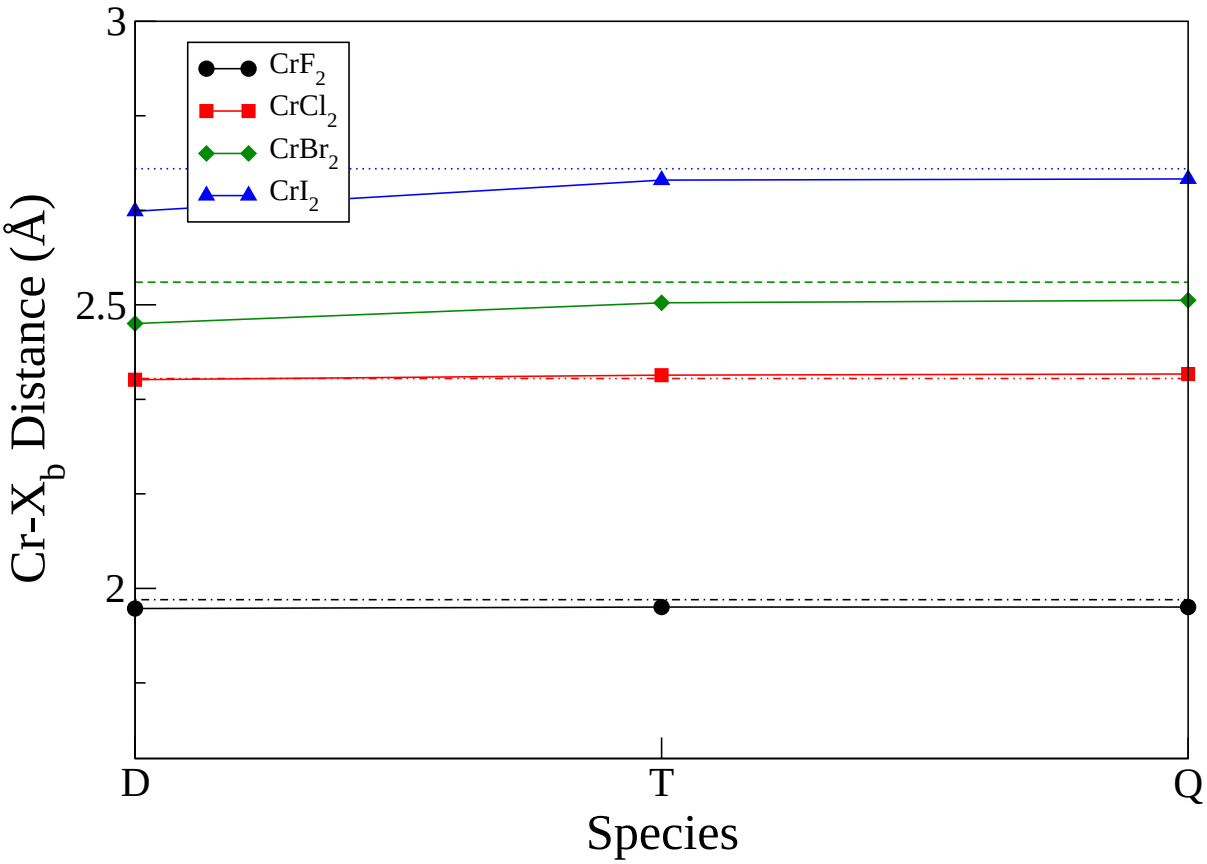

Figure 4.3: Gas-phase Cr-X_b distances for the dihalide-bridged, anti-ferromagnetically coupled oligomers. Solid-state values are indicated by dashed lines and are taken from Refs. [116–119].

dissociation energies would decrease going down the halide group, as ion-ion interactions become progressively weaker. This was not the case. Our calculations showed that the dissociation energies of the $CrCl_2$, $CrBr_2$, and CrI_2 oligomers were roughly the same, with each monomer adding approximately 45 kcal/mol to the cluster. These trends are represented pictorally in Figure 4.4 for the oligomer global minima. We see that the D_e for the CrF_2 oligomers are approximately 10-20 kcal/mol higher than all of the other chromium dihalides. The D_e values for $CrCl_2$, $CrBr_2$, and CrI_2 are all very close to each other. We note that the plots of the dissociation energies are linear for all of the chromium dihalides. Turning to the literature, we found that the standard sublimation enthalpies of the chromium dihalides follow a similar pattern. Brewer et al. reported that the standard sublimation enthalpies of CrF_2, $CrCl_2$, $CrBr_2$, and CrI_2 were 85, 64.8, 63.3,

and 62 kcal/mol, respectively [13,123,131–135]; the CrF_2 value was an estimation. We see that the sublimation enthalpy for CrF_2 is approximately 20 kcal/mol higher than the other chromium dihalides. We calculated the standard dissociation enthalpies (ΔH°_{dis}) for the tetramers of CrF_2, $CrCl_2$, $CrBr_2$, and CrI_2 to be 158.8, 128.5, 132.6, and 128.5 kcal/mol, respectively. Note that the $CrCl_2$ value does not include the CASPT2 corrections. The ΔH°_{dis} of dissociation for Cr_4F_8 is roughly 26-30 kcal/mol higher than the other three tetramers. The ΔH°_{dis} values for Cr_4Cl_8, Cr_4Br_8, and Cr_4I_8 are similar, with the Cr_4Br_8 value being 4 kcal/mol higher than the other two. If we take the average ΔH_{298} values for reactions (1)–(3) (see section 3.2.5) as a crude approximation of the standard enthalpies of sublimation for the chromium dihalides, we get 52.9, 42.8, 44.2, and 42.8 kcal/mol for CrF_2, $CrCl_2$, $CrBr_2$, and CrI_2, respectively. Though these enthaplies are significantly less than the experimental values, we see the relationships arising among these molecules early in the nucleation processes.

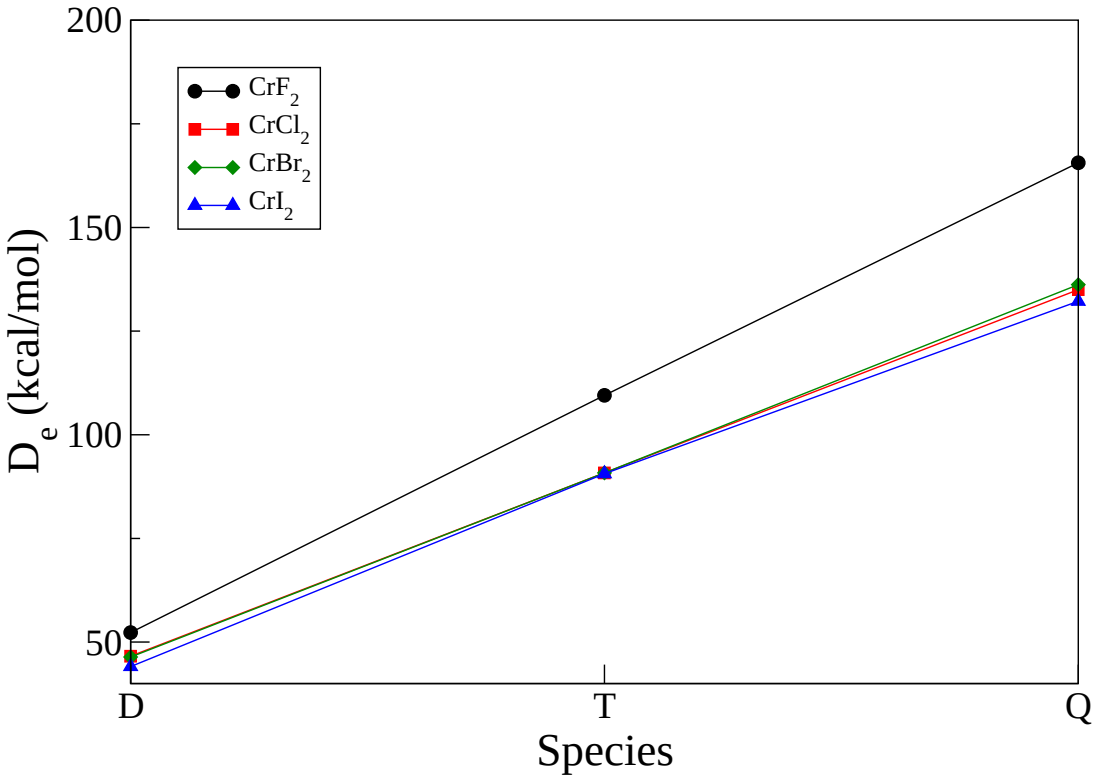

Figure 4.4: Dissociation energies (D_e) for the different chromium dihalide oligomers obtained from DFT calculations.

During the calculations of the chain-like structures for the chromium dihalides, we noticed that the energy difference between the high and low-spin states converged to specific values. For the tetramers of CrF_2, $CrCl_2$, $CrBr_2$, and CrI_2, the energy difference between the septendecet and singlet states of (Q1) from our DFT calculations are 0.022, 0.048, 0.104, and 0.057 eV, respectively. We mention that in our solid-state calculations of α-$CrCl_2$, the energy difference between the AFM and FM coupling schemes was only 0.016 eV. We see that our gas-phase calculations overestimate the energy difference - being slightly over double that of the calculated solid-state value. The literature value for this energy difference at 298 K is 0.009 eV [115]. It is well-known, however, that BS-DFT overestimates the energy difference between the high and low-spin states [53].

Chapter 5

Conclusions

The chromium dihalides represent a class of deceptively simple molecules for which to study experimentally and theoretically. The difficulties from both the computations and experimental analyses amply support this.

According to the literature, both the electronic state and the shape of the ground-state monomeric molecules were in doubt. Infrared spectroscopy and gas-phase electron diffraction experiments supported a linear structure for the monomers, in agreement with the geometry predicted by LFT. From a computational standpoint, handling an open electron shell system requires special care. It has been shown previously [19,20] that LFT is only a crude approximation for these systems, as there is a noticeable $3d$-$4s$ mixing, giving rise to low-lying, closely-spaced electronic states. In this thesis, complete active space calculations with different sizes of the active space were applied; as well as multi-reference, second-order many-body perturbation theory, and coupled cluster calculations, in order to treat both dynamical and nondynamical electron correlation for the monomers. Our results showed that the treatment of these systems is extremely method-dependent. Our DFT calculations predicted that from among the possible electronic states of a linear molecule, the $^5\Pi_g$ state has the lowest energy, but it is a second-order saddle point, in agreement with the ramifications of the Renner-Teller effect. Our CASSCF(16,15) and CCSD(T) calculations also showed that the $^5\Pi_g$ state was lowest in energy for the linear molecules.

The chromium dihalides, with their d^4 electronic configuration, are interesting systems in that they are subject to both the Jahn-Teller and the Renner-Teller effects; the former in their crystals and the latter in the gas-phase. The chromium atoms in the chromium

dihalide crystals have a distorted (elongated) octahedral coordination according to their X-ray diffraction data, consistent with a typical Jahn-Teller distortion of a high-symmetry octahedral coordination around a d^4 metal. Our solid-state calculations on α-$CrCl_2$ also supported this distorted structure. Linear molecules are not subject to Jahn-Teller effects, but they can undergo Renner-Teller effects, as this is demonstrated by the vapor-phase molecules.

According to the Renner-Teller effect, the lowest-energy linear electronic state of the molecule, $^5\Pi_g$, splits into two nondegenerate states, of which the $^5B_2$ symmetry state is the ground state from all of our DFT, CCSD(T), and CASSCF(16,15) calculations, and the molecule is bent. However, the actual depth of the bending potential for these molecules is very shallow, with only a few vibrational levels fitting within this well. As high temperatures are required to vaporize these molecules, our calculations showed that a significant percentage of them will have enough energy to become linear. The ramifications of this is that the vibrationally-averaged structure could appear linear in the gas-phase at such high temperatures. Our calculated bond lengths for the ground states were all in good agreement with the DFT, CCSD(T), and ED studies from other groups. Some of the correlated ab-initio calculations produced different ground states. The CASPT2 method puts the $^5B_2$ electronic state above the $^5\Sigma_g^+$ state for CrF_2, $CrCl_2$, and $CrBr_2$. Our full-space MP2 calculations predicted a $^5\Sigma_g^+$ ground state for CrF_2. However, given that our DFT and full-space CCSD(T) calculations places the $^5B_2$ state below the $^5\Sigma_g^+$ state, we are certain that the ordering of the states is $^5B_2 <^5 \Sigma_g^+ <^5 \Delta_g$. The lower spin states were much higher in energy and were not contestants for the ground state.

Small clusters of chromium dihalides from the dimers to the tetramers were studied with DFT. We observed that all of the low-spin states exhibited broken-symmetry solutions. All of the global minima for the dimers consisted of planar, dihalide-bridged structures of either C_{2h} or C_{2v} symmetry. Our DFT calculations predicted that the global minima were in the singlet state, with the exception of Cr_2I_4, whose global minimum was calculated to be in the nonet state. The energy difference between the C_{2h} and C_{2v} structures is very small, and both of them are candidates for the global minimum. The lowest energy singlet and nonet states of the dimers had almost identical geometries.

The BS-DFT calculations unrealistically overestimate the stabilities of the coupled-spin states. Hence, we carried out CASPT2(8,10) calculations for the singlet and nonet states of the dimers. Our calculations showed that the high-spin nonet states were slightly

lower in energy than the singlet states, with the exception of Cr_2F_4, for which the singlet state was lowest in energy. Because of the high computational cost of these type of calculations, the geometry of the dimers was fixed at those obtained from DFT calculations, and a proper geometry optimization could easily favor the singlet state over the nonet. This, however, was not computationally feasible.

For the trimers, we obtained two different geometries for the global minima. For Cr_3F_6 and Cr_3Cl_6, the continuation of the planar ribbon-like structure of C_{2h} symmetry was lowest in energy. All of the Cr atoms within these structures were anti-ferromagnetically coupled, leading to quintet global minima, with the high-spin tridecet states lying less than 0.022 eV above the quintet states. The global minima for Cr_3Br_6 and Cr_3I_6 consisted of the triangular structure (T2) in the quintet state.

The lowest energy tetramers of CrF_2 and $CrCl_2$, again, consisted of planar ribbons with C_{2h} symmetry - very similar to their solid-state structures; the singlet states were lowest in energy, with the nonet and septendecet states lying slightly higher in energy. It is interesting to point out that in our solid-state calculations of α-$CrCl_2$, the spins of the $3d$ electrons on the Cr atoms within the chains are all anti-ferromagnetically coupled in the ground state with a $(4\alpha 4\beta 4\alpha 4\beta \ldots)$ spin-coupling pattern. Hence, our solid-state calculations would predict that the monomer and trimer would be in the quintet state and the tetramer would be in the singlet state. This is indeed the case from our gas-phase calculations of $CrCl_2$. We calculated the global minima of Cr_4Br_8 and Cr_4I_8 consisted of a continuation of the triangular structure (Q3) and (Q4); however, the nonet state of Cr_4Br_8 was lowest in energy and not the singlet. We believe that the strong spin-spin repulsion between the two closely-spaced Cr atoms in our BS representation of the singlet state is responsible for its destabilization relative to the nonet state. The singlet state of (Q3) was calculated to be the global minimum of Cr_4I_8.

We estimated the two-body basis set superposition errors (BSSE) for the oligomer global minima using counterpoise-corrected energies, with several different combination schemes tested for the trimers and tetramers. Our calculations showed that the amount of the BSSE is relatively small and less than 10% of the binding energies. However, the energy differences between the global minima and some of the low-lying states were smaller than the magnitude of the BSSE. After calculating the BSSE for all of the low-energy minima, we cannot say with certainty that the global minimum for the CrI_2 dimer is the nonet state, as the energy difference between the singlet and nonet states is too

small. The differences in the BSSE between the remaining global minima and low-lying states were not larger than their corresponding energy differences.

We reanalyzed the previously published ED data on $CrCl_2$ [3] taking into consideration the more complicated vapor composition as supposed in that study. We found that the vapor of chromium dichloride contained about 19(4)% dimers and 4(3)% trimers beside the main component, the monomers, but their larger size means greater contributions to the molecular scattering due to their larger number of atomic pairs than their small percentage would indicate. The present ED analysis is in agreement with the previous one in that the molecule is not linear; however, the bond angle from the present study, 149(9.5)°, is much larger than the one reported in Ref. [3], which was calculated to be 110°. We estimated the experimental equilibrium bond length of $CrCl_2$ by anharmonic corrections, which came to r_e^M(Cr-Cl) = 2.196(20) Å. This value as well as the bond angle of the molecule agrees very well with our computations. The unusually large uncertainties of the parameters are due to the complicated vapor composition and the very large correlations among the closely spaced distances belonging to the different species. The dibridged structure of the trimeric species, found to be the ground-state structure by our computations, is also in agreement with the experiment, while the usual structure of metal halide trimers, the six-membered ring structure, is not. The bridged structure of the dimeric and trimeric species can be considered as a first step in the nucleation process leading to the crystal of $CrCl_2$.

Young et al. [136] conclude their recent article on the shape of the TiF_2 molecule with the following statement: "There is now no reliable experimental evidence for the nonlinearity of any first row transition metal difluoride or dichloride." In view of our findings on the nonlinearity of $CrCl_2$, we offer the following comment. Our computations determined that this molecule undergoes Renner-Teller symmetry breaking, and within the adiabatic (Born-Oppenheimer) approximation - which strictly defines the structure of a molecule [137] - it is bent. It is comforting that the electron diffraction experimental data are fully consistent with this finding. At this point, it is of interest to look into the question: could the ED data alone be interpreted by a linear arrangement of the molecule? This question is not as straightforward as we might think since ED yields a thermal average structure rather than the equilibrium structure, hence, even a linear molecule appears to be bent in an ED analysis. Thus, the question is whether it might be possible to distinguish a bent thermal average structure from a genuinely nonlinear

geometry? The shrinkage of the nonbonded Cl$\cdots$Cl distance for a linear metal dichloride molecule is always much larger than that of a truly bent molecule, so the thermal-average structure for such a linear molecule could be close to a truly bent one. There is a simple relationship between the bending frequency of a linear molecule and the shrinkage effect and, consequently, the bond angle of the molecule [138]. As we already discussed above, the computed bending frequencies of $CrCl_2$ are much too small to be reliable. However, there are experimental frequencies available for several other transition metal dichlorides [2]. In between $TiCl_2$ (130 cm^{-1}) and $CuCl_2$ (122 cm^{-1}), the bending frequencies of other first-row transition metal dichlorides vary between about 85 – 95 cm^{-1}. Thus, it seems reasonable to suppose that the gas-phase bending frequency of $CrCl_2$ would not be smaller than, say, 90 – 100 cm^{-1}. We performed structure analyses with bond angles constrained at values corresponding to bending frequencies in the region between 60 – 120 cm^{-1}. The agreement with experiment somewhat worsened compared with the structure with the refined 149° bond angle. However, whenever the constraint on the bond angle was lifted, it always refined to the 149° value. We also checked what bending frequency would correspond to a thermal average bond angle of 149° for a molecule whose equilibrium structure would be linear. The corresponding ν_2 was 73 cm^{-1}. This value appears far too low considering the trend of the bending frequency variation among the first row transition metal dichlorides. This observation lends additional support for the nonlinearity of $CrCl_2$.

We calculated various thermodynamic properties of the oligomers at 298.15 K as well as from 1000–2000 K. The CrF_2 oligomers had the highest of the dissociation energies, between 10-20 kcal/mol higher than the other dihalides. We saw that the dissociation energies as well as the enthalpies of the oligomerization reactions for $CrCl_2$, $CrBr_2$, and CrI_2 were close in value to each other. The addition of each CrX_2 monomer to the clusters added an almost constant value in energy. For CrF_2, this value was approximately 55 kcal/mol, and for the other dihalides, this value was roughly 45 kcal/mol. This result was also supported by our PAW calculations where we obtained a cohesive energy of 42.9 kcal/mol per $CrCl_2$ unit for the AFM infinite chain. This compares well with the 46.4 kcal/mol per unit for the solid which includes interactions between the $CrCl_2$ chains. Our dissociation energies and standard enthalpies of dissociation were underestimated by our DFT methods. For $CrCl_2$, we applied a correction to the dissociation energies which gave better agreement with the experimental data. The similarity in the dissociation energies and nucleation enthalpies among $CrCl_2$, $CrBr_2$, and CrI_2 was very surprising, as $CrBr_2$

and CrI_2 have different global minima for the trimers and tetramers. It is interesting to note that the standard enthalpies of sublimation for the chromium dihalides follow a similar pattern to those we calculated for D_e and ΔH°_{dis}, though again our DFT results were too low compared to the literature data.

We investigated crystalline α-$CrCl_2$ using first-principles DFT calculations. We optimized the crystal structure utilizing the LSDA or PW91 exchange functional. The PW91 optimized structure is in good agreement with experiment. We also confirmed experimental data in that α-$CrCl_2$ is anti-ferromagnetically coupled along the crystallographic c-axis. The intra- and interchain magnetic coupling constants were calculated using a variety of different methods; all local and semilocal exchange-correlation schemes grossly overestimate the magnetic coupling. A LSDA+U study with $U + J = 3.8$ eV gives good agreement with experiment. Hybrid DFT calculations, which include some of the exact exchange, also give rather poor results with a qualitatively different interchain coupling scheme.

Chapter 6

Appendix

6.1 Cartesian Coordinates of the Low-energy Structures

Table 6.1: Cartesian coordinates (in Å) and energies of the optimized CrF_2 oligomers.

Method	Structure	State	Atom	X	Y	Z
E=-572.255636129 au						
PW91/LanL2DZ	D1	$^9A_1$	Cr	0	1.543793	0.144313
			F	0	0	1.411996
			Cr	0	-1.543793	0.144313
			F	0	-3.205530	-0.554396
			F	0	0	-1.072871
			F	0	3.205530	-0.554396
E=-572.256411925 au						
PW91/LanL2DZ	D1	$^1A_1$	Cr	-1.537951	0.147900	0
			F	0	1.417027	0
			Cr	1.537951	0.147900	0
			F	0	-1.074047	0
			F	-3.193075	-0.565898	0
			F	3.193075	-0.565898	0

Table 6.1 *Continued*

Method	Structure	State	Atom	X	Y	Z
E=-572.255654275 au						
PW91/LanL2DZ	D2	$^{9}A_g$	Cr	1.524247	0.225088	0
			F	0.217913	-1.227020	0
			Cr	-1.524247	-0.225088	0
			F	-0.217913	1.227020	0
			F	3.272621	-0.197861	0
			F	-3.272621	0.197861	0
E=-572.256051093 au						
PW91/LanL2DZ	D2	$^{1}A_g$	Cr	-1.512217	-0.220525	0
			F	-0.220722	1.238545	0
			Cr	1.512217	0.220525	0
			F	0.220722	-1.238545	0
			F	-3.261974	0.188816	0
			F	3.261974	-0.188816	0
E=-858.431698201 au						
PW91/LanL2DZ	T1	$^{13}A_g$	Cr	0	0	0
			F	-1.843505	-0.724066	0
			Cr	-2.938076	0.908941	0
			F	-4.735950	0.748309	0
			F	1.060520	-1.649597	0
			Cr	2.938076	-0.908941	0
			F	1.843505	0.724066	0
			F	4.735950	-0.748309	0
			F	-1.060520	1.649597	0

Table 6.1 *Continued*

Method	Structure	State	Atom	X	Y	Z
E=-858.432958714 au						
PW91/LanL2DZ	T1	^5A_g	Cr	0	0	0
			F	1.943465	-0.409945	0
			Cr	1.964254	-2.367587	0
			F	3.580436	-3.164787	0
			F	0	1.968041	0
			Cr	-1.964254	2.367587	0
			F	-1.943465	0.409945	0
			F	-3.580436	3.164787	0
			F	0	-1.968041	0
E=-1144.60614654 au						
PW91/LanL2DZ	Q1	$^{17}A_g$	Cr	1.537560	-0.067304	0
			F	-0.052386	-1.241218	0
			Cr	-1.537560	0.067304	0
			F	-3.133514	-1.114344	0
			Cr	-4.620320	0.163622	0
			F	-6.314253	-0.453999	0
			F	3.133514	1.114344	0
			Cr	4.620320	-0.163622	0
			F	6.314253	0.453999	0
			F	3.021861	-1.367231	0
			F	0.052386	1.241218	0
			F	-3.021861	1.367231	0

Table 6.1 *Continued*

Method	Structure	State	Atom	X	Y	Z
E=-1144.60748365 au						
PW91/LanL2DZ	Q1	^9A_g	Cr	0	0	0
			F	0	0	1.970813
			Cr	1.929158	0	2.380429
			F	1.936769	0.065493	4.376719
			Cr	3.887650	0.199866	4.783274
			F	5.437346	0.384969	5.687350
			F	1.928085	-0.065493	0.424270
			F	-1.936769	0.141189	-0.424270
			Cr	-1.929158	0.199866	-2.380429
			F	0	0	-1.970813
			F	3.474079	0.065493	2.825366
			F	-3.474079	0.427588	-3.301507
E=-1144.60831114 au						
PW91/LanL2DZ	Q1	^1A_g	Cr	-1.538661	0	0
			Cr	-4.616479	-0.030205	0
			F	-3.081943	-1.244278	0
			F	-3.072252	1.239071	0
			F	-6.267687	-0.746345	0
			Cr	1.538661	0	0
			F	0	-1.237689	0
			F	0	1.237689	0
			Cr	4.616479	0.030205	0
			F	3.072252	-1.239071	0
			F	3.081943	1.244278	0
			F	6.267687	0.746345	0

Table 6.1 *Continued*

Method	Structure	State	Atom	X	Y	Z
E=-573.698457231 au						
B3LYP	D1	$^9A_1$	Cr	-1.522258	-0.099452	0
			F	0	-1.360610	0
			Cr	1.522258	-0.099452	0
			F	3.261938	0.382775	0
			F	0	1.125470	0
			F	-3.261938	0.382777	0
E=-573.698994152 au						
B3LYP	D1	$^1A_1$	Cr	0	1.511590	0.089250
			F	0	0	-1.147754
			Cr	0	-1.511590	0.089250
			F	0	-3.263903	-0.342605
			F	0	0	1.356964
			F	0	3.263903	-0.342605
E=-573.698606995 au						
B3LYP	D2	^9A_g	Cr	-0.024271	-1.522315	0
			F	-0.591069	-3.236319	0
			F	-1.244058	0	0
			Cr	0.024271	1.522315	0
			F	1.244058	0	0
			F	0.591069	3.236319	0
E=-573.699019712 au						
B3LYP	D2	^1A_g	Cr	-1.508435	0.027294	0
			F	0	-1.256942	0
			Cr	1.508435	-0.027294	0
			F	3.231457	-0.557902	0
			F	0	1.256942	0
			F	-3.231457	0.557902	0

Table 6.1 *Continued*

Method	Structure	State	Atom	X	Y	Z
E=-860.59412079 au						
B3LYP	T1	$^{13}A_g$	Cr	0	0	0
			F	1.934852	-0.380290	0
			Cr	1.943351	-2.329844	0
			F	3.424940	-3.362088	0
			F	0	1.967610	0
			Cr	-1.943351	2.329844	0
			F	-1.934852	0.380290	0
			F	-3.424940	3.362088	0
			F	0	-1.967610	0
E=-860.594915809 au						
B3LYP	T1	$^{5}A_g$	Cr	0	0	0
			F	1.936634	-0.357718	0
			Cr	1.944558	-2.304603	0
			F	3.431780	-3.329269	0
			F	0	1.965355	0
			Cr	-1.944558	2.304603	0
			F	-1.936634	0.357718	0
			F	-3.431780	3.329269	0
			F	0	-1.965355	0
E=-1147.48959945 au						
B3LYP	Q1	$^{17}A_g$	Cr	-0.011158	1.513441	0
			Cr	-0.011158	4.548210	0
			F	1.230246	3.048227	0
			F	-1.270349	3.028844	0
			F	0.449574	6.295230	0
			Cr	0.011158	-1.513441	0
			F	1.253966	0.008963	0
			F	-1.253966	-0.008963	0
			Cr	0.011158	-4.548210	0
			F	1.270349	-3.028844	0
			F	-1.230246	-3.048227	0
			F	-0.449574	-6.295230	0

Table 6.1 *Continued*

Method	Structure	State	Atom	X	Y	Z
E=-1147.48985627 au						
B3LYP	Q1	^9A_g	Cr	-0.011198	1.510314	0
			Cr	-0.011198	4.521447	0
			F	1.238105	3.028404	0
			F	-1.277754	3.008419	0
			F	0.448070	6.268312	0
			Cr	0.011198	-1.510314	0
			F	1.249473	0.009040	0
			F	-1.249473	-0.009040	0
			Cr	0.011198	-4.521447	0
			F	1.277754	-3.008419	0
			F	-1.238105	-3.028404	0
			F	-0.448070	-6.268312	0
E=-1147.49039974 au						
B3LYP	Q1	^1A_g	Cr	-0.011187	1.514805	0
			Cr	-0.011187	4.531316	0
			F	1.238376	3.040086	0
			F	-1.278216	3.020145	0
			F	0.448283	6.278728	0
			Cr	0.011187	-1.514805	0
			F	1.252287	0.009102	0
			F	-1.252287	-0.009102	0
			Cr	0.011187	-4.531316	0
			F	1.278216	-3.020145	0
			F	-1.238376	-3.040086	0
			F	-0.448283	-6.278728	0

Table 6.2: Cartesian coordinates (in Å) and energies of the optimized $CrCl_2$ oligomers.

Method	Structure	State	Atom	X	Y	Z
E=-232.762638816 au						
PW91/LanL2DZ	D1	$^9A_1$	Cr	-1.741411	0.252080	0
			Cl	0	1.949182	0
			Cr	1.741411	0.252080	0
			Cl	3.795895	-0.630550	0
			Cl	0	-1.399842	0
			Cl	-3.795895	-0.630550	0
E=-232.763519498 au						
PW91/LanL2DZ	D1	$^1A_1$	Cr	1.704230	-0.242862	0
			Cl	0	-1.959682	0
			Cr	-1.704230	-0.242862	0
			Cl	-3.773332	0.599591	0
			Cl	0	1.446232	0
			Cl	3.773332	0.599591	0
E=-232.762605062 au						
PW91/LanL2DZ	D2	^9A_g	Cr	-0.269376	1.729939	0
			Cl	0.269376	3.900297	0
			Cl	1.649170	0.277064	0
			Cr	0.269376	-1.729939	0
			Cl	-1.649170	-0.277064	0
			Cl	-0.269376	-3.900297	0
E=-232.763474755 au						
PW91/LanL2DZ	D2	^1A_g	Cr	-0.242568	1.696309	0
			Cl	0.242568	3.877219	0
			Cl	1.680012	0.267939	0
			Cr	0.242568	-1.696309	0
			Cl	-1.680012	-0.267939	0
			Cl	-0.242568	-3.877219	0

Table 6.2 *Continued*

Method	Structure	State	Atom	X	Y	Z
E=-349.183018312 au						
PW91/LanL2DZ	T1	$^{13}A_g$	Cr	0	0	0
			Cl	2.419352	-0.144141	0
			Cr	2.426755	-2.547018	0
			Cl	4.466110	-3.468313	0
			Cl	0	2.420147	0
			Cr	-2.426755	2.547018	0
			Cl	-2.419352	0.144141	0
			Cl	-4.466110	3.468313	0
			Cl	0	-2.420147	0
E=-349.184129153 au						
PW91/LanL2DZ	T1	$^{5}A_g$	Cr	0	0	0
			Cl	2.421489	-0.092127	0
			Cr	2.424279	-2.489561	0
			Cl	4.458289	-3.419793	0
			Cl	0	2.414354	0
			Cr	-2.424279	2.489561	0
			Cl	-2.421489	0.092127	0
			Cl	-4.458289	3.419793	0
			Cl	0	-2.414354	0

Table 6.2 *Continued*

Method	Structure	State	Atom	X	Y	Z
E=-465.602642798 au						
PW91/LanL2DZ	Q1	$^{17}A_g$	Cr	1.764242	-0.100088	0
			Cl	-0.098988	-1.647030	0
			Cr	-1.764242	0.100088	0
			Cl	-3.626818	-1.454501	0
			Cr	-5.279176	0.284237	0
			Cl	-7.397125	-0.441029	0
			Cl	3.626818	1.454501	0
			Cr	5.279176	-0.284237	0
			Cl	7.397125	0.441029	0
			Cl	3.431420	-1.854569	0
			Cl	0.098988	1.647030	0
			Cl	-3.431420	1.854569	0
E=-465.6032238 au						
PW91/LanL2DZ	Q1	$^{9}A_g$	Cr	1.754150	0.101168	0
			Cl	-0.108064	1.643661	0
			Cr	-1.754150	-0.101168	0
			Cl	-3.614248	1.481990	0
			Cr	-5.243199	-0.271957	0
			Cl	-7.369227	0.424897	0
			Cl	3.614248	-1.481990	0
			Cr	5.243199	0.271957	0
			Cl	7.369227	-0.424897	0
			Cl	3.418643	1.853550	0
			Cl	0.108064	-1.643661	0
			Cl	-3.418643	-1.853550	0

Table 6.2 *Continued*

Method	Structure	State	Atom	X	Y	Z
E=-465.603957184 au						
PW91/LanL2DZ	Q1	^1A_g	Cr	1.756227	-0.100286	0
			Cl	-0.098029	-1.649626	0
			Cr	-1.756227	0.100286	0
			Cl	-3.594535	-1.480919	0
			Cr	-5.224887	0.271458	0
			Cl	-7.350233	-0.428053	0
			Cl	3.594535	1.480919	0
			Cr	5.224887	-0.271458	0
			Cl	7.350233	0.428053	0
			Cl	3.400171	-1.865074	0
			Cl	0.098029	1.649626	0
			Cl	-3.400171	1.865074	0
E=-2015.18319704 au						
B3LYP	D1	$^9A_1$	Cr	0	0.138687	1.691942
			Cl	0	1.825147	0
			Cr	0	0.138687	-1.691942
			Cl	0	-0.358647	-3.846774
			Cl	0	-1.499439	0
			Cl	0	-0.358647	3.846774
E=-2015.18519734 au						
B3LYP	D1	$^1A_1$	Cr	1.653538	0.094292	0
			Cl	3.837637	-0.240746	0
			Cl	0	-1.580948	0
			Cr	-1.653538	0.094292	0
			Cl	0	1.796221	0
			Cl	-3.837637	-0.240746	0
E=-2015.18307275 au						
B3LYP	D2	^9A_g	Cr	-0.132320	1.691643	0
			Cl	0.132320	3.887239	0
			Cl	1.653426	0.145973	0
			Cr	0.132320	-1.691643	0
			Cl	-1.653426	-0.145973	0
			Cl	-0.132320	-3.887239	0

Table 6.2 *Continued*

Method	Structure	State	Atom	X	Y	Z
E=-2015.18516674 au						
B3LYP	D2	^1A_g	Cr	-0.096224	1.650708	0
			Cl	0.096224	3.851911	0
			Cl	1.683724	0.111780	0
			Cr	0.096224	-1.650708	0
			Cl	-1.683724	-0.111780	0
			Cl	-0.096224	-3.851911	0
E=-3022.80948553 au						
B3LYP	T1	$^{13}A_g$	Cr	0	0	0
			Cl	0	2.393323	0
			Cr	2.350577	2.500727	0
			Cl	3.600193	4.329251	0
			Cl	-2.391911	-0.128727	0
			Cr	-2.350577	-2.500727	0
			Cl	0	-2.393323	0
			Cl	-3.600193	-4.329251	0
			Cl	2.391911	0.128727	0
E=-3022.81113319 au						
B3LYP	T1	^5A_g	Cr	0	0	0
			Cl	0	2.390885	0
			Cr	2.347298	2.445482	0
			Cl	3.624129	4.254322	0
			Cl	-2.389655	-0.079521	0
			Cr	-2.347298	-2.445482	0
			Cl	0	-2.390885	0
			Cl	-3.624129	-4.254322	0
			Cl	2.389655	0.079521	0

Table 6.2 *Continued*

Method	Structure	State	Atom	X	Y	Z
E=-4030.4354273 au						
B3LYP	Q1	$^{17}A_g$	Cr	-0.005356	1.732781	0
			Cr	-0.005356	5.167941	0
			Cl	1.634329	3.481868	0
			Cl	-1.660002	3.471655	0
			Cl	0.314783	7.360764	0
			Cr	0.005356	-1.732781	0
			Cl	1.635634	0.005872	0
			Cl	-1.635634	-0.005872	0
			Cr	0.005356	-5.167941	0
			Cl	1.660002	-3.471655	0
			Cl	-1.634329	-3.481868	0
			Cl	-0.314783	-7.360764	0
E=-4030.43648498 au						
B3LYP	Q1	$^{9}A_g$	Cr	1.735360	-0.038330	0
			Cl	-0.031845	-1.636277	0
			Cr	-1.735360	0.038330	0
			Cl	-3.497172	-1.552485	0
			Cr	-5.146112	0.119852	0
			Cl	-7.339980	-0.194169	0
			Cl	3.497172	1.552485	0
			Cr	5.146112	-0.119852	0
			Cl	7.339980	0.194169	0
			Cl	3.413871	-1.743197	0
			Cl	0.031845	1.636277	0
			Cl	-3.413871	1.743197	0

Table 6.2 *Continued*

Method	Structure	State	Atom	X	Y	Z
E=-4030.43719007 au						
B3LYP	Q1	^1A_g	Cr	-0.018465	1.739965	0
			Cr	-0.040483	5.123215	0
			Cl	1.629509	3.473409	0
			Cl	-1.701312	3.440257	0
			Cl	0.256934	7.318260	0
			Cr	0.018465	-1.739965	0
			Cl	1.629509	0.017950	0
			Cl	-1.629509	-0.017950	0
			Cr	0.040483	-5.123215	0
			Cl	1.701312	-3.440257	0
			Cl	-1.629509	-3.473409	0
			Cl	-0.256934	-7.318260	0
E=-2015.06485965 au						
B3PW91	D1	$^9A_1$	Cr	-1.673010	-0.181541	0
			Cl	-3.768621	0.471639	0
			Cl	0	1.439755	0
			Cr	1.673010	-0.181541	0
			Cl	0	-1.870460	0
			Cl	3.768621	0.471639	0
E=-2015.06669595 au						
B3PW91	D1	$^1A_1$	Cr	1.628518	-0.149201	0
			Cl	3.756219	0.382641	0
			Cl	0	1.512913	0
			Cr	-1.628518	-0.149201	0
			Cl	0	-1.856923	0
			Cl	-3.756219	0.382641	0
E=-2015.06452369 au						
B3PW91	D2	^9A_g	Cr	-0.167493	1.673793	0
			Cl	1.636849	0.185172	0
			Cr	0.167493	-1.673793	0
			Cl	-0.167493	-3.843188	0
			Cl	0.167493	3.843188	0
			Cl	-1.636849	-0.185172	0

Table 6.2 *Continued*

Method	Structure	State	Atom	X	Y	Z
E=-2015.06656142 au						
B3PW91	D2	^1A_g	Cr	0	1.628762	0
			Cl	0.491623	3.766335	0
			Cl	-1.682751	-0.023015	0
			Cr	0	-1.628762	0
			Cl	1.682751	0.023015	0
			Cl	-0.491623	-3.766335	0
E=-3022.63334915 au						
B3PW91	T1	$^{13}A_g$	Cr	0	0	0
			Cl	0	2.372169	0
			Cr	2.325542	2.479176	0
			Cl	3.400627	4.396724	0
			Cl	-2.372074	-0.120016	0
			Cr	-2.325542	-2.479176	0
			Cl	0	-2.372169	0
			Cl	-3.400627	-4.396724	0
			Cl	2.372074	0.120016	0
E=-3022.63501134 au						
B3PW91	T1	^5A_g	Cr	0	0	0
			Cl	2.369732	-0.057591	0
			Cr	2.352348	-2.380005	0
			Cl	4.220002	-3.538188	0
			Cl	0	2.370380	0
			Cr	-2.352348	2.380005	0
			Cl	-2.369732	0.057591	0
			Cl	-4.220002	3.538188	0
			Cl	0	-2.370380	0

Table 6.2 *Continued*

Method	Structure	State	Atom	X	Y	Z
E=-4030.20174660 au						
B3PW91	Q1	$^{17}A_g$	Cr	-0.009401	1.715599	0
			Cr	-0.009401	5.117333	0
			Cl	1.613676	3.450257	0
			Cl	-1.658005	3.432458	0
			Cl	0.512481	7.254167	0
			Cr	0.009401	-1.715599	0
			Cl	1.624661	0.010322	0
			Cl	-1.624661	-0.010322	0
			Cr	0.009401	-5.117333	0
			Cl	1.658005	-3.432458	0
			Cl	-1.613676	-3.450257	0
			Cl	-0.512481	-7.254167	0
E=-4030.20237609 au						
B3PW91	Q1	$^{9}A_g$	Cr	-0.006401	1.722650	0
			Cr	-0.016341	5.063683	0
			Cl	1.635709	3.432018	0
			Cl	-1.680526	3.403852	0
			Cl	0.470386	7.207789	0
			Cr	0.006401	-1.722650	0
			Cl	1.635709	0.029676	0
			Cl	-1.635709	-0.029676	0
			Cr	0.016341	-5.063683	0
			Cl	1.680526	-3.403852	0
			Cl	-1.635709	-3.432018	0
			Cl	-0.470386	-7.207789	0

Table 6.2 *Continued*

Method	Structure	State	Atom	X	Y	Z
E=-4030.20365349 au						
B3PW91	Q1	^1A_g	Cr	-0.014331	1.707296	0
			Cr	-0.018391	5.049520	0
			Cl	1.631560	3.416212	0
			Cl	-1.685816	3.392483	0
			Cl	0.485308	7.189877	0
			Cr	0.014331	-1.707296	0
			Cl	1.631560	0.014655	0
			Cl	-1.631560	-0.014655	0
			Cr	0.018391	-5.049520	0
			Cl	1.685816	-3.392483	0
			Cl	-1.631560	-3.416212	0
			Cl	-0.485308	-7.189877	0

Table 6.3: Cartesian coordinates (in Å) and energies of the optimized $CrBr_2$ oligomers.

Method	Structure	State	Atom	X	Y	Z
E=-225.64137971 au						
PW91/LanL2DZ	D1	$^9A_1$	Cr	1.792691	-0.344995	0
			Br	0	-2.217555	0
			Cr	-1.792692	-0.344995	0
			Br	-3.986212	0.614672	0
			Br	0	1.461349	0
			Br	3.986213	0.614671	0
E=-225.642386686 au						
PW91/LanL2DZ	D1	$^1A_1$	Cr	-1.742617	-0.327323	0
			Br	0	-2.221431	0
			Cr	1.742617	-0.327323	0
			Br	3.957973	0.571956	0
			Br	0	1.526425	0
			Br	-3.957973	0.571956	0

Table 6.3 *Continued*

Method	Structure	State	Atom	X	Y	Z
E=-225.640682399 au						
PW91/LanL2DZ	D2	^9A_g	Cr	0.713209	-0.255059	-1.647178
			Cr	-0.713209	0.255059	1.647178
			Br	2.232487	0	-3.479659
			Br	-2.232487	0	3.479659
			Br	-1.344946	-1.176043	-0.371586
			Br	1.344946	1.176043	0.371586
E=-225.642020127 au						
PW91/LanL2DZ	D2	^1A_g	Cr	0	1.758194	0
			Br	1.863887	0.031503	0
			Cr	0	-1.758194	0
			Br	-1.863887	-0.031503	0
			Br	0.707361	4.041069	0
			Br	-0.707361	-4.041069	0
E=-338.497134183 au						
PW91/LanL2DZ	T1	$^{13}A_g$	Cr	0	0	0
			Br	2.058557	-1.562217	0
			Cr	3.637880	0.431814	0
			Br	5.952068	-0.185558	0
			Br	-1.603281	-2.022871	0
			Cr	-3.637880	-0.431814	0
			Br	-2.058557	1.562217	0
			Br	-5.952068	0.185558	0
			Br	1.603281	2.022871	0
E=-338.498494541 au						
PW91/LanL2DZ	T1	^5A_g	Cr	0	0	0
			Br	1.585250	-2.030022	0
			Cr	3.587005	-0.408556	0
			Br	2.032641	1.596567	0
			Br	-2.032641	-1.596567	0
			Cr	-3.587005	0.408556	0
			Br	-1.585250	2.030022	0
			Br	5.910422	0.165438	0
			Br	-5.910422	-0.165438	0

Table 6.3 *Continued*

Method	Structure	State	Atom	X	Y	Z
E=-338.48962585 au						
PW91/LanL2DZ	T2	$^{13}A'$	Cr	1.386413	1.508573	0.103050
			Cr	1.386413	-1.508573	0.103050
			Br	3.528814	0	0.013239
			Br	0.617178	0	2.131790
			Br	-0.924574	-2.548537	-0.051518
			Br	0.617178	0.000000	-2.131790
			Br	-0.924574	2.548537	-0.051518
			Cr	-1.560514	0	-0.533907
			Br	-3.823948	0	0.286436
E=-338.498344337 au						
PW91/LanL2DZ	T2	^{5}A	Cr	1.346436	1.371368	0.087089
			Cr	1.251021	-1.311425	0.089374
			Br	3.512536	-0.049330	-0.030629
			Br	0.786233	0.041403	2.276079
			Br	-0.958530	-2.520183	0.019805
			Br	0.607104	-0.069356	-2.219580
			Br	-0.886566	2.524259	-0.085738
			Cr	-1.538898	-0.009411	-0.554740
			Br	-3.786647	0.038556	0.299452
E=-451.353837763 au						
PW91/LanL2DZ	Q1	$^{17}A_g$	Cr	-1.850721	-0.002911	0
			Cr	-5.515633	0.025483	0
			Br	-3.698968	1.807906	0
			Br	-3.698968	-1.807906	0
			Br	-7.741885	0.912020	0
			Cr	1.850721	0.002911	0
			Br	-0.004215	1.789811	0
			Br	0.004215	-1.789811	0
			Cr	5.515633	-0.025483	0
			Br	3.698968	1.807906	0
			Br	3.698968	-1.807906	0
			Br	7.741885	-0.912020	0

Table 6.3 *Continued*

Method	Structure	State	Atom	X	Y	Z
E=-451.354250658 au						
PW91/LanL2DZ	Q1	^9A_g	Cr	3.033488	0.014273	-0.445870
			Cr	-3.033488	-0.014273	0.445870
			Br	0.763192	-0.017911	-1.914435
			Br	-0.763192	0.017911	1.914435
			Br	5.397112	0.030653	-0.019401
			Br	-5.397112	-0.030653	0.019401
			Br	-2.395306	-2.362341	-0.489956
			Br	2.490558	-2.320844	0.532339
			Cr	0.047452	-1.832650	-0.040376
			Br	-2.490558	2.320844	-0.532339
			Br	2.395306	2.362341	0.489956
			Cr	-0.047452	1.832650	0.040376
E=-451.354873329 au						
PW91/LanL2DZ	Q1	^1A_g	Cr	-0.129476	1.839624	0
			Cr	-0.338083	5.435452	0
			Br	1.582495	3.777060	0
			Br	-2.071686	3.532777	0
			Br	0.338083	7.732327	0
			Cr	0.129476	-1.839624	0
			Br	1.788834	0.126869	0
			Br	-1.788834	-0.126869	0
			Cr	0.338083	-5.435452	0
			Br	2.071686	-3.532777	0
			Br	-1.582495	-3.777060	0
			Br	-0.338083	-7.732327	0

Table 6.3 *Continued*

Method	Structure	State	Atom	X	Y	Z
E=-451.343966831 au						
PW91/LanL2DZ	Q4	^9A	Cr	-2.990994	-0.280135	-0.820972
			Cr	0.143569	-1.752756	0.693455
			Br	-1.253293	-2.198631	-1.383703
			Br	-1.895850	-0.532735	1.885346
			Br	-5.279421	0.430231	-0.621045
			Cr	2.905062	0.199294	0.040351
			Br	1.556424	-0.181609	2.380218
			Br	2.366199	-2.342572	-0.389732
			Br	4.534685	0.554345	-1.690806
			Br	1.811167	2.595647	0.096276
			Br	-1.738824	2.008815	-0.909498
			Cr	-0.205057	1.347258	1.010209
E=-1842.26172522 au						
PW91	D1	$^9A_1$	Cr	0.246367	-1.693884	0
			Br	2.119577	0	0
			Cr	0.246367	1.693884	0
			Br	-0.469200	3.919108	0
			Br	-1.519052	0	0
			Br	-0.469200	-3.919108	0
E=-1842.26541662 au						
PW91	D1	$^1A_1$	Cr	0.026183	-1.641985	0
			Br	1.867494	0.000000	0
			Cr	0.026183	1.641985	0
			Br	0.025067	3.972854	0
			Br	-1.867494	0.000000	0
			Br	0.025067	-3.972854	0
E=-1842.26166402 au						
PW91	D2	^9A_g	Cr	-0.000345	1.488682	0
			Br	-1.954307	0.000000	0
			Cr	0.000345	-1.488682	0
			Br	-0.000345	-3.825476	0
			Br	1.954307	0.000000	0
			Br	0.000345	3.825476	0

Table 6.3 *Continued*

Method	Structure	State	Atom	X	Y	Z
E=-1842.26537145 au						
PW91	D2	^1A_g	Cr	0	0	0
			Br	0	0	2.481098
			Cr	2.436774	0	2.202213
			Br	3.951469	0	3.973879
			Br	-1.529209	0	-1.759154
			Br	2.436774	0	-0.278885
E=-2763.42889002 au						
PW91	T1	^5A_g	Cr	0	0	0
			Br	-0.747184	2.452590	0
			Cr	1.649109	3.058200	0
			Br	2.847139	5.061167	0
			Br	2.417712	0.714684	0
			Br	0.747184	-2.452590	0
			Cr	-1.649109	-3.058200	0
			Br	-2.847139	-5.061167	0
			Br	-2.417712	-0.714684	0
E=-2763.43197538 au						
PW91	T2	$^{13}A'$	Cr	1.320323	1.419760	0.091916
			Cr	1.320323	-1.419760	0.091916
			Br	3.428796	0	-0.127014
			Br	-0.917139	0	2.142073
			Br	-0.917257	-2.455329	0.015284
			Br	0.540430	0	-2.076015
			Br	-0.917257	2.455329	0.015284
			Cr	-1.516926	0	-0.502123
			Br	-3.760979	0	0.248978

Table 6.3 *Continued*

Method	Structure	State	Atom	X	Y	Z
E=-2763.43197538 au						
PW91	T2	^5A	Cr	1.277945	1.265293	0.065967
			Cr	1.155322	-1.193451	0.089824
			Br	3.396655	-0.065016	-0.145396
			Br	0.923046	0.072793	2.256330
			Br	-0.952720	-2.443057	0.087029
			Br	0.538809	-0.088435	-2.168339
			Br	-0.869453	2.437887	-0.065365
			Cr	-1.471161	-0.022798	-0.515284
			Br	-3.696066	0.052198	0.282250
E=-3684.5833963 au						
PW91	Q4	^{17}A	Cr	-2.921495	-0.208270	-0.804330
			Cr	0.138124	-1.657922	0.695512
			Br	-1.248067	-2.047831	-1.333156
			Br	-1.812887	-0.449015	1.864012
			Br	-5.205854	0.299580	-0.592697
			Cr	2.776826	0.159711	0.006021
			Br	1.541978	-0.153516	2.303304
			Br	2.285030	-2.315440	-0.340206
			Br	4.421992	0.459218	-1.662960
			Br	1.817430	2.514230	0.067954
			Br	-1.686057	1.959219	-0.890345
			Cr	-0.159072	1.317912	0.954601
E=-3684.60008799 au						
PW91	Q4	^9A	Cr	-2.851415	-0.256086	-0.758292
			Cr	0.214231	-1.345155	0.619184
			Br	-1.073503	-1.963306	-1.389287
			Br	-1.817588	-0.452307	1.864762
			Br	-5.154956	0.155242	-0.550284
			Cr	2.641059	0.142483	0.013472
			Br	1.560448	-0.080909	2.395515
			Br	2.311005	-2.345754	-0.191974
			Br	4.148614	0.406454	-1.783692
			Br	1.778648	2.523339	0.063330
			Br	-1.662972	1.927817	-0.924333
			Cr	-0.134681	1.210002	0.878084

Table 6.3 *Continued*

Method	Structure	State	Atom	X	Y	Z
E=-3684.59528095 au						
PW91	Q4	^1A	Cr	-2.548935	-0.287432	-0.647525
			Cr	0.381177	-1.584325	0.709502
			Br	-0.941360	-2.154882	-1.291932
			Br	-1.620217	-0.542270	1.935370
			Br	-4.849466	0.164400	-0.463715
			Cr	2.240236	0.224476	-0.163435
			Br	1.721091	-0.115396	2.376113
			Br	2.544050	-2.290982	-0.225558
			Br	2.743483	0.534780	-2.440053
			Br	1.866023	2.685278	0.304006
			Br	-1.504135	1.982778	-0.814506
			Cr	-0.013372	1.262708	1.006026

Table 6.4: Cartesian coordinates (in Å) and energies of the optimized CrI_2 oligomers.

Method	Structure	State	Atom	X	Y	Z
E=-218.524680965 au						
PW91/LanL2DZ	D1	$^9A_1$	Cr	1.847262	-0.426016	0
			I	0	-2.503390	0
			Cr	-1.847282	-0.426016	0
			I	-4.201076	0.660070	0
			I	0	1.568960	0
			I	4.201076	0.660070	0
E=-218.52546772 au						
PW91/LanL2DZ	D1	$^1A_1$	Cr	1.789451	0.415723	0
			I	0	2.514256	0
			Cr	-1.789451	0.415723	0
			I	0	-1.631762	0
			I	4.156897	-0.629499	0
			I	-4.156897	-0.629499	0

Table 6.4 *Continued*

Method	Structure	State	Atom	X	Y	Z
E=-218.523626043 au						
PW91/LanL2DZ	D2	^9A_g	Cr	-1.822060	-0.482800	0
			I	-0.539298	1.938206	0
			Cr	1.822060	0.482800	0
			I	0.539298	-1.938206	0
			I	-4.391408	-0.147313	0
			I	4.391408	0.147313	0
E=-218.524715873 au						
PW91/LanL2DZ	D2	^1A_g	Cr	-1.780546	0.350505	0
			I	-0.430102	-2.012950	0
			Cr	1.780546	-0.350505	0
			I	0.430102	2.012950	0
			I	-4.356334	0.133873	0
			I	4.356334	-0.133873	0
E=-327.818141776 au						
PW91/LanL2DZ	T1	$^{13}A_g$	Cr	0	0	0
			I	1.970801	-1.975794	0
			Cr	3.874548	0.027380	0
			I	6.262262	1.034652	0
			I	-1.970801	1.975794	0
			Cr	-3.874548	-0.027380	0
			I	-1.970801	-1.969492	0
			I	-6.262262	-1.034652	0
			I	1.970801	-1.975794	0
E=-327.818738908 au						
PW91/LanL2DZ	T1	^5A_g	Cr	0	0	0
			I	2.183302	-1.733668	0
			Cr	3.796369	0.446876	0
			I	6.304572	-0.192909	0
			I	-1.684017	-2.218166	0
			Cr	-3.796369	-0.446876	0
			I	-2.183302	1.733668	0
			I	-6.304572	0.192909	0
			I	1.684017	2.218166	0

Table 6.4 *Continued*

Method	Structure	State	Atom	X	Y	Z
E=-327.817920371 au						
PW91/LanL2DZ	T2	$^{13}A'$	Cr	1.474774	1.516992	0.099660
			Cr	1.474774	-1.516992	0.099660
			I	3.847640	0	0.032408
			I	0.767404	0	2.368578
			I	-0.965379	-2.736887	-0.051680
			I	0.728253	0	-2.343378
			I	-0.965379	2.736887	-0.051861
			Cr	-1.552209	0	-0.574851
			I	-4.045204	0	0.215840
E=-327.821102935 au						
PW91/LanL2DZ	T2	^{5}A	Cr	-1.366311	1.489688	-0.129158
			Cr	-1.366318	-1.489690	-0.129125
			I	-3.743888	0.000014	-0.363264
			I	-0.438135	0.000022	-2.349836
			I	0.971681	-2.809109	0.282897
			I	-0.928766	-0.000053	2.352946
			I	0.971661	2.809113	0.282971
			Cr	1.310392	-0.000001	0.508208
			I	3.811479	0.000015	-0.318887
E=-437.110318199 au						
PW91/LanL2DZ	Q3	$^{17}A_g$	Cr	-3.171455	-0.045777	0.451031
			Cr	3.171455	0.045777	-0.451031
			I	-0.819189	-0.019636	2.082957
			I	0.819189	0.019636	-2.082957
			I	-5.772513	0.049533	0.260628
			I	5.772513	-0.049533	-0.260628
			I	2.600259	-2.372542	0.760134
			I	-2.550291	-2.499151	-0.737950
			Cr	0.000283	-1.876903	0.004060
			I	2.550291	2.499151	0.737950
			I	-2.600259	2.372542	-0.760134
			Cr	-0.000283	1.876903	-0.004060

Table 6.4 *Continued*

Method	Structure	State	Atom	X	Y	Z
E=-437.111313713 au						
PW91/LanL2DZ	Q3	^9A	Cr	-3.203785	-0.000228	0.512531
			Cr	3.203905	-0.000732	-0.513127
			I	-0.928722	-0.138451	2.267747
			I	0.927824	-0.138951	-2.267069
			I	-5.783594	-0.062768	0.173319
			I	5.783917	-0.063446	-0.176193
			I	2.451087	-2.237201	0.943871
			I	-2.451513	-2.238563	-0.942349
			Cr	-0.000390	-1.504149	0.000602
			I	2.517542	2.432957	0.615188
			I	-2.516590	2.433799	-0.614564
			Cr	0.000379	1.532989	0.000105
E=-437.112901922 au						
PW91/LanL2DZ	Q3	^1A_g	Cr	-3.177249	-0.033667	-0.495165
			Cr	3.177249	0.033667	0.495165
			I	-0.933932	-0.078276	-2.266974
			I	0.933932	0.078276	2.266974
			I	-5.758487	-0.026392	-0.208664
			I	5.758487	0.026392	0.208664
			I	2.417720	2.349577	-0.839060
			I	-2.559489	2.311889	0.782124
			Cr	-0.054714	1.511098	-0.039488
			I	2.559489	-2.311889	-0.782124
			I	-2.417720	-2.349577	0.839060
			Cr	0.054714	-1.511098	0.039488

Table 6.4 *Continued*

Method	Structure	State	Atom	X	Y	Z
E=-437.112737145 au						
PW91/LanL2DZ	Q4	^{17}A	Cr	-3.074132	-0.156492	-0.982108
			Cr	0.316523	-1.938266	0.370835
			I	-0.716856	-1.195857	-2.080412
			I	-2.095035	-1.292116	1.698070
			I	-5.667432	-0.099143	-0.750862
			Cr	2.976660	0.213509	0.185000
			I	1.580400	-0.571643	2.603090
			I	2.798990	-2.485785	-0.623539
			I	4.858782	0.996894	-1.453888
			I	1.645943	2.655059	0.406389
			I	-2.321577	2.376978	-0.170109
			Cr	-0.402817	1.032396	1.246141
E=-437.120584013 au						
PW91/LanL2DZ	Q4	^{9}A	Cr	3.143465	0.291770	-0.830097
			Cr	-0.099169	1.683113	0.672725
			I	1.430058	2.403408	-1.477685
			I	2.116194	0.546763	2.037820
			I	5.528108	-0.727687	-0.587373
			Cr	-2.872972	-0.185893	0.107754
			I	-1.660511	0.342694	2.689277
			I	-2.423650	2.496374	-0.492436
			I	-4.662376	-0.629303	-1.748102
			I	-1.968839	-2.806246	0.351822
			I	1.528832	-1.932278	-1.189983
			Cr	0.076415	-1.112635	0.969743

Table 6.4 *Continued*

Method	Structure	State	Atom	X	Y	Z
E=-437.116982613 au						
PW91/LanL2DZ	Q4	^1A	Cr	-0.857234	1.387841	1.270324
			Cr	0.857181	-1.387797	1.270253
			I	3.367764	-2.076716	0.424789
			I	-1.643236	-1.038898	2.408838
			I	1.643132	1.038806	2.408998
			I	-3.367723	2.076871	0.424692
			I	0.130341	2.019912	-1.330216
			I	-0.130300	-2.019891	-1.330329
			Cr	-2.016636	0.102100	-1.010197
			Cr	2.016686	-0.102112	-1.010294
			I	-4.086983	-1.383902	-1.620984
			I	4.087007	1.383804	-1.621298
E=-1365.54309068 au						
PW91	D1	$^9A_1$	Cr	-0.000013	1.538790	0
			I	-2.158122	0	0
			Cr	0.000013	-1.538790	0
			I	-0.000072	-4.081640	0
			I	2.158122	0	0
			I	-0.000072	4.081640	0
E=-1365.54303937 au						
PW91	D1	$^1A_1$	Cr	0	1.724984	0
			I	2.201670	0.204153	0
			Cr	0.317367	-1.697302	0
			I	0.129580	-4.226776	0
			I	-1.853597	-0.174652	0
			I	-0.621366	4.184740	0

Table 6.4 *Continued*

Method	Structure	State	Atom	X	Y	Z
E=-1365.54295622 au						
PW91	D2	^1A_g	Cr	1.315773	1.122231	0
			I	1.315773	-1.543595	0
			Cr	-1.315376	-1.122231	0
			I	-3.245302	-2.767909	0
			I	3.245302	2.767909	0
			I	-1.315376	1.543595	0
E=-2048.33836491 au						
PW91	T2	$^{13}A'$	Cr	-1.418722	-1.446134	0.087228
			Cr	-1.418722	1.446134	0.087228
			I	-3.761652	0	-0.085606
			I	-0.897608	0	2.349141
			I	0.958205	2.663383	-0.006396
			I	-0.661405	0	-2.278052
			I	0.958205	-2.663383	-0.006396
			Cr	1.525523	0	-0.545565
			I	3.998331	0	0.195352
E=-2048.35374836 au						
PW91	T2	^5A	Cr	0.012376	1.507921	0.754774
			I	0.595508	1.617852	-1.894441
			I	0.441572	-0.752518	2.320702
			Cr	-1.110046	-1.216081	0.030359
			I	-2.867747	-2.389329	-1.454186
			I	2.593566	2.210533	1.257626
			Cr	1.809219	-0.015355	-0.083034
			I	1.119172	-2.344957	-1.160425
			I	-2.593504	1.020137	0.612654

Table 6.4 *Continued*

Method	Structure	State	Atom	X	Y	Z
E=-2731.13734089 au						
PW91	Q3	$^{17}A_g$	Cr	-3.105309	0.037645	-0.389202
			Cr	3.105309	-0.037645	0.389202
			I	-0.867392	0.014554	-2.058187
			I	0.867392	-0.014554	2.058187
			I	-5.666390	-0.037265	-0.297720
			I	5.666390	0.037265	0.297720
			I	2.509248	2.292839	-0.820970
			I	-2.453632	2.404591	0.798630
			Cr	0.001325	1.742872	-0.015886
			I	2.453631	-2.404591	-0.798630
			I	-2.509248	-2.292839	0.820970
			Cr	-0.001325	-1.742872	0.015886
E=-2731.15542547 au						
PW91	Q3	^{9}A	Cr	-2.810281	0.048807	0.251300
			Cr	2.810250	0.049649	-0.251468
			I	-0.945897	-0.347970	2.260342
			I	0.945398	-0.347276	-2.259559
			I	-5.362401	0.109713	-0.038053
			I	5.362812	0.109489	0.033607
			I	2.351390	-2.361884	0.894868
			I	-2.350558	-2.363178	-0.893368
			Cr	0.000208	-1.496238	0.000419
			I	2.208860	2.652016	0.074613
			I	-2.209614	2.651835	-0.072795
			Cr	-0.000156	1.170887	0.000511

Table 6.4 *Continued*

Method	Structure	State	Atom	X	Y	Z
E=-2731.15632149546 au						
PW91	Q3	^1A_g	Cr	2.644848	0.022934	-0.235307
			Cr	-2.644848	-0.022934	0.235307
			I	0.868130	-0.015968	-2.300716
			I	-0.868130	0.015968	2.300716
			I	5.183225	-0.010864	0.167874
			I	-5.183225	0.010864	-0.167874
			I	-2.265154	-2.641544	-0.300972
			I	2.277308	-2.604511	0.319378
			Cr	0.016751	-1.255849	-0.007603
			I	-2.277308	2.604511	-0.319378
			I	2.265154	2.641544	0.300972
			Cr	-0.016751	1.255849	0.007603

6.2 Experimental Electron Diffraction Molecular Intensities

Table 6.5: Electron diffraction molecular intensities (in $Å^{-1}$) for two camera ranges for $CrCl_2$

Camera range: 50 cm

$S_{min} = 2.00$ $S_{max} = 14.00$ step size = 0.125

-409.0	-443.2	-448.8	-406.1	-318.9	-195.4	-65.7	68.2
194.9	313.2	407.4	480.1	523.3	517.0	448.7	337.8
205.8	51.0	-84.6	-197.7	-302.7	-378.7	-429.0	-450.0
-457.2	-423.4	-363.2	-283.6	-156.4	-8.1	147.8	297.2
405.0	492.8	502.1	471.1	395.7	300.2	183.0	48.9
-47.6	-147.8	-229.4	-290.1	-334.7	-344.2	-343.9	-334.6
-280.9	-209.8	-128.9	-47.4	62.1	137.4	223.9	283.2
315.6	321.4	315.7	266.9	213.6	129.6	52.0	-19.4
-97.3	-158.9	-218.4	-249.1	-263.8	-260.0	-231.6	-200.1
-145.1	-90.2	-21.1	56.2	102.9	166.0	189.2	231.7
216.3	199.7	169.4	129.0	89.4	38.6	-11.7	-58.9
-96.0	-123.4	-144.1	-155.8	-170.8	-167.9	-146.8	-111.0
-59.1							

Camera range: 19 cm

$S_{min} = 9.25$ $S_{max} = 29.00$ step size = 0.25

					296.8	238.0	73.3
-90.7	-220.7	-278.2	-251.7	-141.9	-7.2	119.5	227.5
229.3	142.7	64.7	-29.0	-110.9	-155.2	-164.5	-121.2
-35.1	35.5	99.7	125.8	136.2	99.0	18.3	-34.5
-87.5	-132.6	-118.3	-70.4	-15.1	39.7	85.1	106.6
87.2	53.3	34.1	-33.5	-42.5	-82.4	-78.2	-58.5
-15.6	0.8	30.6	45.6	64.2	51.6	27.9	-12.9
-35.2	-16.8	-28.0	-23.8	-13.5	1.9	17.0	12.8
19.1	-4.2	0.0	-2.2	-0.8	-11.1	-18.6	0.3
16.1	11.9	1.2	-19.2	15.1	9.4	-1.1	4.6
-3.5	1.0	-21.7	-37.9	-21.3			

6.3 Modified Basis Sets for Cr, Br, and I

Table 6.6: Modified basis set for Cr.

Type	No. Contractions	Exponent	Coefficient
S	2	14.053450	0.8856241645
		11.735218	-1.030132191
S	1	5.9049150	1
S	1	1.6346650	1
S	1	0.6629310	1
S	1	0.0978000	1
S	1	0.0377050	1
S	1	0.0133690	1
P	2	51.317664	0.02967198637
		9.3214980	-1.012759535
P	1	3.7411210	1
P	1	1.5102140	1
P	1	0.5379560	1
P	1	0.0934080	1
P	1	0.0266450	1
P	1	0.0100000	1
D	3	26.781439	0.03497001324
		8.2316400	0.1721950652
		2.7816450	0.4270321617
D	1	0.9036780	1
D	1	0.2492580	1
D	1	0.0700000	1
D	1	0.0250000	1
F	6	7.7139000	0.0390498000
		3.0575000	0.168051500
		1.2119000	0.405014700
		0.4803000	0.450786500
		0.1904000	0.227614700
		0.0755000	0.0535853000
F	6	7.7139000	-0.0921689000
		3.0575000	-0.360906800
		1.2119000	-0.455905600
		0.4803000	0.247494900
		0.1904000	0.518272900
		0.0755000	0.192898900
F	6	7.7139000	0.204737400
		3.0575000	0.574575400
		1.2119000	-0.171444700
		0.4803000	-0.697253100
		0.1904000	0.457467300
		0.0755000	0.419648500

Table 6.7: Modified basis set for Br.

Type	No. Contractions	Exponent	Coefficient
S	6	2808.60	0.001606
		421.180	0.008393
		50.3457	0.069578
		17.9133	-0.389908
		3.80531	0.694497
		1.74968	0.491354
S	6	2808.60	-0.000635
		421.180	-0.003492
		50.3457	-0.025195
		17.9133	0.150113
		3.80531	-0.366226
		1.74968	-0.383422
S	1	0.448555	1
S	1	0.164498	1
S	1	0.0502	1
P	6	105.752	0.005341
		27.6368	-0.083084
		6.59656	0.447766
		2.78522	0.550617
		1.07812	0.123500
		0.393537	-0.003771
P	6	105.752	-0.001308
		27.6368	0.022921
		6.59656	-0.145029
		2.78522	-0.209037
		1.07812	0.093730
		0.393537	0.605021
P	1	0.127469	1
P	1	0.0394	1
D	6	143.865	0.010237
		46.1163	0.076083
		17.3694	0.229807
		6.95107	0.403347
		2.75607	0.409728
		1.01178	0.162790
D	1	0.4291	1
D	1	0.1548	1

Table 6.8: Modified basis set for I.

Type	No. Contractions	Exponent	Coefficient
S	6	2437.23	0.000430
		358.331	0.002292
		14.5856	0.393905
		9.18532	-0.925011
		2.10199	0.935200
		1.03944	0.391057
S	6	2437.23	0.000179
		358.331	0.001077
		14.5856	0.166524
		9.18532	-0.415575
		2.10199	0.630059
		1.03944	0.324446
S	1	0.317845	1
S	1	0.122187	1
S	1	0.0421	1
P	4	18.3299	0.083100
		11.4794	-0.258792
		2.75125	0.665756
		1.21708	0.451823
P	4	18.3299	-0.026616
		11.4794	0.0883472
		2.75125	-0.301465
		1.21708	-0.151315
P	1	0.342164	1
P	1	0.111445	1
P	1	0.0339	1
D	4	51.2059	0.004042
		15.7468	-0.004992
		4.51661	0.293292
		2.04408	0.512688
D	1	0.869864	1
D	1	0.3013	1
D	1	0.1196	1

Bibliography

[1] Hargittai, M. *Coord. Chem. Rev.*, **1988**, *91*, 35.

[2] Hargittai, M. *Chem. Rev.*, **2000**, *100*, 2233.

[3] Hargittai, M.; Dorofeeva, O. V.; Tremmel, J. *Inorg. Chem.*, **1985**, *24*, 3963.

[4] Zasorin, E. Z.; Gershikov, A. G.; Spiridonov, V. P.; Ivanov, A. A. *Zh. Strukt. Khim.*, **1987**, *28*, 56.

[5] Jacox, M. E.; Milligan, D. E. *J. Chem. Phys.*, **1969**, *51*, 4143.

[6] Hastie, J. W.; Hauge, R.; Margrave, J. L. *Chem. Comm.*, **1969**, 1452.

[7] Hastie, J. W.; Hauge, R. H.; Margrave, J. L. *High Temp. Sci.*, **1971**, *3*, 257.

[8] Kobra, V. M. *Zh. Neorg. Khim*, **1983**, *28*, 2689.

[9] Ogden, J. S.; Wyatt, R. S. *J. Chem. Soc. Dalton Trans.*, **1987**, 859.

[10] Konings, R. J. M.; Booij, A. S. *J. Mol. Struct.*, **1992**, *269*, 39.

[11] Gregory, P. D.; Ogden, J. S. *J. Chem. Soc. Dalton Trans.*, **1995**, 1423.

[12] Konings, R. J. M. *High Temp. Mat. Sci.*, **1996**, *35*, 105.

[13] Schoonmaker, R. C.; Friedman, A. H.; Porter, R. F. *J. Chem. Phys.*, **1959**, *31*, 1586.

[14] Ratkovskii, P. A.; Pribitkova, T. A.; Galickii, P. V. *Tepl. Vys. Temp.*, **1974**, *12*, 731.

[15] DeKock, C. W.; Gruen, D. M. *J. Chem. Phys.*, **1966**, *44*, 4387.

[16] DeKock, C. W.; Gruen, D. M. *J. Chem. Phys.*, **1968**, *49*, 4521.

[17] Garner, C. D.; Hillier, I. H.; Wood, C. *Inorg. Chem.*, **1978**, *17*, 168.

[18] Smith, S.; Hillier, I. H. *J. Chem. Soc. Chem. Commun.*, **1989**, 539.

[19] Wang, S. G.; Schwarz, W. H. E. *J. Chem. Phys.*, **1998**, *109*, 7252.

[20] Bridgeman, A. J.; Bridgeman, C. H. *Chem. Phys. Lett.*, **1997**, *272*, 173.

[21] Jensen, V. R. *Mol. Phys.*, **1997**, *91*, 131.

[22] Nielsen, I. M. B.; Allendorf, M. D. *J. Phys. Chem. A*, **2005**, *109*, 928.

[23] Schiefenhövel, N.; Binnewies, M.; Janetzko, F.; Jug, K. *Z. Anorg. Allg. Chem.*, **2001**, *627*, 1513.

[24] Li, X.; Paldus, J. *J. Chem. Phys.*, **2007**, *126*, 234303.

[25] Zhao, Y.; Truhlar, D. G. *J. Chem. Phys.*, **2006**, *124*, 224105.

[26] Gisdakis, P.; Rösch, N. R.; Görling, A.; Trickey, S. B. *Topics Organomet. Chem.*, **2006**, *4*, 109.

[27] Cococcioni, M.; de Gironcoli, S. *Phys. Rev. B*, **2005**, *71*, 035105.

[28] Anisimov, V. I.; Zaanen, J. *Phys. Rev. B*, **1991**, *44*, 943.

[29] Harvey, J. N. *Structure and Bonding*, **2004**, *112*, 151.

[30] Hermann, A.; Vest, B.; Schwerdtfeger, P. *Phys. Rev. B*, **2006**, *74*, 224402.

[31] Jensen, F. *Introduction to Computational Chemistry.* John Wiley and Sons: Chichester, 2003.

[32] Born, M.; Oppenheimer, R. *Annalen der Physik*, **1927**, *84*, 457.

[33] Slater, J. C. *Quantum Theory of Matter.* McGraw-Hill: New York, 2nd edition, 1968.

[34] Cook, D. B. *Handbook of Computational Quantum Chemistry.* Dover Publications: New York, 2005.

[35] Møller, C.; Plesset, M. *Phys. Rev.*, **1934**, *46*, 618.

[36] Bartlett, R. J. *J. Phys. Chem.*, **1989**, *93*, 1697.

[37] Hohenberg, P.; Kohn, W. *Phys. Rev.*, **1964**, *136*, B864.

[38] Kohn, W.; Sham, L. J. *Phys. Rev.*, **1965**, *140*, A1133.

[39] Dirac, P. A. M. *Proc. Camb. Phil. Soc.*, **1930**, *26*, 376.

[40] Vosko, S. H.; Wilk, L.; Nusair, M. *Can. J. Phys.*, **1980**, *58*, 1200.

[41] Perdew, J. P.; Chevary, J. A.; Vosko, S. H.; Jackson, K. A.; Pederson, M. R.; Singh, D. J.; Fiolhais, C. *Phys. Rev. B*, **1992**, *46*, 6671.

[42] Perdew, J. P.; Burke, K.; Ernzerof, M. *Phys. Rev. Lett.*, **1996**, *77*, 3865.

[43] Becke, A. D. *Phys. Rev. A*, **1988**, *38*, 3098.

[44] Perdew, J. P.; Burke, K.; Ernzerhof, M. *Phys. Rev. Lett.*, **1997**, *78*, 1396.

[45] Lee, C.; Yang, W.; Parr, R. G. *Phys. Rev. B*, **1988**, *37*, 785.

[46] Preuss, H. *Chem. Phys. Lett.*, **1989**, *157*, 200.

[47] Harris, J. *Phys. Rev. A*, **1984**, *29*, 1648.

[48] Becke, A. D. *J. Chem. Phys.*, **1993**, *98*, 5648.

[49] Stephens, P. J.; Devlin, F. J.; Chabalowski, C. F.; Frisch, M. J. *J. Phys. Chem.*, **1994**, *98*, 11623.

[50] Pople, J. A.; Nesbet, R. K. *J. Chem. Phys.*, **1954**, *22*, 571.

[51] Berthier, G. J. *J. Chim. Phys. Biol.*, **1954**, *51*, 363.

[52] Lovell, T.; McGrady, J. E.; Stranger, R.; Macgregor, S. A. *Inorg. Chem.*, **1996**, *35*, 3079.

[53] Rudra, I. R.; Wu, Q.; Voorhis, T. V. *J. Chem. Phys.*, **2006**, *124*, 9.

[54] Adamo, C.; Barone, V.; Bencini, A.; Totti, F.; Ciofini, I. *Inorg. Chem.*, **1999**, *38*, 1996.

[55] Cramer, C. J.; Smith, B. A.; Tolman, W. B. *J. Am. Chem. Soc.*, **1996**, *118*, 11283.

[56] Moreira, I. P. R.; Costa, R.; Filatov, M.; Illas, F. *J. Chem. Theory Comput.*, **2007**, *3*, 764.

[57] Noodleman, L. *J. Chem. Phys.*, **1981**, *74*, 5737.

[58] Filatov, M.; Shaik, S. *Chem. Phys. Lett.*, **1998**, *288*, 689.

[59] Filatov, M.; Shaik, S. *Chem. Phys. Lett.*, **1999**, *304*, 429.

[60] Gräffenstein, J.; Cremer, D. *Chem. Phys. Lett.*, **2000**, *316*, 569.

[61] Calzado, C. J.; Cabrero, J.; Malrieu, J. P.; Caballol, R. *J. Chem. Phys.*, **2002**, *116*, 2728.

[62] Boys, S. F.; Bernardi, F. *Mol. Phys.*, **1970**, *19*, 533.

[63] van Duijneveldt, F. B.; van Duijneveldt-van de Rijdt, J. G. C. M.; van Lenthe, J. H. *Chem. Rev.*, **1994**, *94*, 1873.

[64] Schwartz, W. H. E.; Andrae, D.; Arnold, S. R.; Heidberg, J.; Jr., H. H.; Hinze, J.; Karachalios, A.; Kovner, M. A.; Schmidt, P. C.; Zülicke, L.; Hellmann, H. G. A. *Ber. Bunsenges*, **1933**, *2*, 60.

[65] Hellmann, H. *J. Chem. Phys.*, **1934**, *3*, 61.

[66] Kaldor, U.; Wilson, S., Eds. *Theoretical Chemistry and Physics of Heavy and Superheavy Elements*. Kluwer: Dorecht, 2003.

[67] Dyall, K. *Theor. Chem. Acc.*, **1998**, *99*, 366.

[68] Faegri, K. *Theor. Chem. Acc.*, **1999**, *105*, 252.

[69] Tsuchiya, T.; Abe, M.; Nakajima, T.; Hirao, K. *J. Chem. Phys.*, **2001**, *115*, 4463.

[70] Tatewaki, H.; Mochizuki, Y.; Koga, T.; Karwowski, J. *J. Chem. Phys.*, **2001**, *115*, 9160.

[71] Knappe, P.; Rösch, N. *J. Chem. Phys.*, **1990**, *92*, 1153.

[72] Seminario, J. M.; Politzer, P. *Recent Developments and Applications of Modern Density Functional Theory*, volume 2. Elsevier: Amsterdam, 1995.

[73] Khan, L. R.; Baybutt, P.; Truhlar, D. G. *J. Chem. Phys.*, **1976**, *65*, 3826.

[74] Schwarz, W. H. E. *Theor. Chim. Acta*, **1968**, *11*, 307.

[75] Schwarz, W. H. E. *Theor. Chim. Acta*, **1968**, *11*, 377.

[76] Schwarz, W. H. E. *Acta Phys.*, **1969**, *27*, 391.

[77] Schwarz, W. H. E. *Theor. Chim. Acta*, **1969**, *15*, 235.

[78] Stoll, H.; Metz, B.; Dolg, M. *J. Comp. Chem.*, **2002**, *23*, 767.

[79] Hay, P. J.; Wadt, W. R. *J. Chem. Phys.*, **1985**, *82*, 270.

[80] Wadt, W. R.; Hay, P. J. *J. Chem. Phys*, **1985**, *82*, 284.

[81] Hay, P. J.; Wadt, W. R. *J. Chem. Phys*, **1985**, *82*, 299.

[82] Heinemann, C.; Koch, W.; Schwarz, H. *Chem. Phys. Lett.*, **1995**, *245*, 509.

[83] Hafner, P.; Schwarz, W. H. E. *Chem. Phys. Lett.*, **1979**, *63*, 537.

[84] Ermler, W. C.; Ross, R. R.; Christiansen, P. A. *Adv. Quantum Chem.*, **1988**, *19*, 139.

[85] Ermler, W. C.; Lee, Y. S.; Christiansen, P. A.; Pitzer, K. S. *Chem. Phys. Lett.*, **1981**, *81*, 70.

[86] Domenicano, A.; Hargittai, I., Eds. *Strength from Weakness: Structural Consequences of Weak Interactions in Molecules, Supermolecules, and Crystals*, volume 68 of *Nato Science Series: II. Mathematics, Physics, and Chemistry*. Kluwer: Dorecht, 2001.

[87] Dunning, T. H.; Hay, P. J. *Methods of Electronic Structure, Theory*, volume 2. Plenum Press, 1977.

[88] Dolg, M.; Wedig, U.; Stoll, H.; Preuss, H. *J. Chem. Phys.*, **1987**, *86*, 866.

[89] Woon, D. E.; Dunning, T. H. *J. Chem. Phys.*, **1993**, *98*, 1358.

[90] T. H. Dunning, J. *J. Chem. Phys.*, **1989**, *90*, 1007.

[91] Kendall, R. H.; T. H. Dunning, J. *J. Chem. Phys.*, **1992**, *96*, 6796.

[92] Peterson, K. A.; Figgen, D.; Goll, E.; Stoll, H.; Dolg, M. *J. Chem. Phys.*, **2003**, *119*, 11113.

[93] Frisch, M. J.; Trucks, G. W.; Schlegel, H. B.; Scuseria, G. E.; Robb, M. A.; Cheeseman, J. R.; Montgomery, J. A. Jr.; Vreven, T.; Kudin, K. N.; Burant, J. C.; Millam, J. M.; Iyengar, S. S.; Tomasi, J.; Barone, V.; Mennucci, B.; Cossi, M.; Scalmani, G.; Rega, N.; Petersson, G. A.; Nakatsuji, H.; Hada, M.; Ehara, M.; Toyota, K.; Fukuda, R.; Hasegawa, J.; Ishida, M.; Nakajima, T.; Honda, Y.; Kitao, O.; Nakai, H.; Klene, M.; Li, X.; Knox, J. E.; Hratchian, H. P.; Cross, J. B.; Bakken, V.; Adamo, C.; Jaramillo, J.; Gomperts, R.; Stratmann, R. E.; Yazyev, O.; Austin, A. J.; Cammi, R.; Pomelli, C.; Ochterski, J. W.; Ayala, P. Y.; Morokuma, K.; Voth, G. A.; Salvador, P.; Dannenberg, J. J.; Zakrzewski, V. G.; Dapprich, S.; Daniels, A. D.; Strain, M. C.; Farkas, O.; Malick, D. K.; Rabuck, A. D.; Raghavachari, K.; Foresman, J. B.; Ortiz, J. V.; Cui, Q.; Baboul, A. G.; Clifford, S.; Cioslowski, J.; Stefanov, B. B.; Liu, G.; Liashenko, A.; Piskorz, P.; Komaromi, I.; Martin, R. L.; Fox, D. J.; Keith, T.; Al-Laham, M. A.; Peng, C. Y.; Nanayakkara, A.; Challacombe, M.; Gill, P. M. W.; Johnson, B.; Chen, W.; Wong, M. W.; Gonzalez, C.; Pople, J. A. Gaussian 03, Revision C.03. Gaussian, Inc., Wallingford, CT, 2004.

[94] Werner, H.-J.; Knowles, P. J.; Lindh, R.; Manby, F. R.; Schütz, M.; Celani, P.; Korona, T.; Rauhut, G.; Amos, R. D.; Bernhardsson, A.; Berning, A.; Cooper, D. L.; Deegan, M. J. O.; Dobbyn, A. J.; Eckert, F.; Hampel, C.; Hetzer, G.; Lloyd, A. W.; McNicholas, S. J.; Meyer, W.; Mura, M. E.; Nicklass, A.; Palmieri, P.; Pitzer, R.; Schumann, U.; Stoll, H.; Stone, A. J.; Tarroni, R.; Thorsteinsson, T. Molpro, version 2006.1, a package of ab initio programs, 2006. see http://www.molpro.net.

[95] Kresse, G.; Furthmüller, J. *Phys. Rev. B*, **1996**, *54*, 11169.

[96] von Barth, U.; Hedin, L. *J. Phys. C*, **1972**, *5*, 1629.

[97] Blöchl, P. E. *Phys. Rev. B*, **1994**, *50*, 17953.

[98] Kresse, G.; Joubert, D. *Phys. Rev. B*, **1999**, *59*, 1758.

[99] Vinet, P.; Ferrante, J.; Smith, J. R.; Rose, J. H. *J. Phys. C*, **1986**, *19*, L467.

[100] Schäfer, H.; Laumanns, R. *Z. Anorg. Allg. Chem.*, **1977**, *47*, 436.

[101] Hargittai, I.; Hernádi, J.; Kolonits, M.; Schultz, G. *Rev. Sci. Instrum.*, **1971**, *42*, 546.

[102] Hargittai, I.; Bohatka, S.; Tremmel, J.; Berecz, I. *Hung. Sci. Instrum.*, **1980**, *50*, 51.

[103] Tremmel, J.; Hargittai, I. *J. Phys. E*, **1985**, *18*, 148.

[104] Schultz, G.; Tremmel, J.; Hargittai, I.; Berecz, I.; Bohatka, S.; Kagramanov, N. D.; Maltsev, A. K.; Nefedov, O. M. *J. Mol. Struct.*, **1979**, *55*, 207.

[105] Hedberg, L.; Mills, I. M. *J. Mol. Spectrosc.*, **1993**, *160*, 117.

[106] Strand, T. G. Program for calculation of partial waves electron scattering factors of atoms (oslo), 1968.

[107] Ross, A. W.; Fink, M.; Hilderbrandt, R.; Wang, J.; Smith, V. H. J. *International Tables for Crystallography C*. Kluwer: Dorecht, 1995.

[108] Andersen, B.; Seip, H. M.; Strand, T. G.; levik, R. S. *Acta Chem. Scand.*, **1969**, *23*, 3224.

[109] Hargittai, M.; Hargittai, I. *Int. J. Quant. Chem.*, **1992**, *44*, 1057.

[110] Hargittai, M.; Subbotina, N. Y.; Kolonits, M.; Gershikov, A. G. *J. Chem. Phys.*, **1991**, *94*, 7278.

[111] Roos, B. O.; Andersson, K.; Fülscher, M. P.; Malmqvist, P.; Serrano-Andrés, L.; Pierloot, K.; Merchán, M. *Advances in Chemical Physics*, volume XCIII. John Wiley and Sons: New York, 1996.

[112] Bersuker, I. B. *Chem. Rev.*, **2001**, *101*, 1067.

[113] Bersuker, I. B. *The Jahn-Teller Effect*. Cambridge University Press: Cambridge, 2006.

[114] Grein, F. *Chem. Phys. Lett.*, **2008**, *345*, 231.

[115] Oswald, H. R. *Helv. Chim. Acta*, **1961**, *44*, 1049.

[116] Tracy, J. W.; Gregory, N. W.; Lingafelter, E. C.; Dunitz, J. D.; Mez, H.-C.; Rundle, R. E.; Scheringer, C.; Jnr, H. L. Y.; Wilkinson, M. K. *Acta Cryst.*, **1961**, *14*, 927.

[117] Jack, K. H.; Maitland, R. *Proc. Chem. Soc.*, **1957**, 232.

[118] Tracy, J. W.; Gregory, N. W.; Lingafelter, E. C. *Acta Cryst.*, **1962**, *15*, 672.

[119] Tracy, J. W.; Gregory, N. W.; Stewart, J. M.; Lingafelter, E. C. *Acta Cryst.*, **1962**, *15*, 460.

[120] Besrest, P. F.; Jaulmes, S. *Acta Cryst. B*, **1973**, *29*, 1560.

[121] Hagiwara, M.; Katsumata, K. *J. Magn. Magn. Mater.*, **1995**, *140*, 1665.

[122] Winkelmann, M.; Baehr, M.; Reehuis, M.; Steiner, M.; Hagiwara, M.; Katsumata, K. *J. Phys. Chem. Solids*, **1997**, *58*, 481.

[123] Brewer, L.; Somayajulu, G. R.; Brackett, E. *Chem. Rev.*, **1963**, *63*, 111.

[124] Hargittai, M.; Schwerdtfeger, P.; Réffy, B.; Brown, R. *Chem. Eur. J.*, **2003**, *9*, 327.

[125] Martin, R. L.; Illas, F. *Phys. Rev. Lett.*, **1997**, *79*, 1539.

[126] Svane, A.; Gunnarsson, O. *Phys. Rev. Lett.*, **1990**, *65*, 1148.

[127] Dudarev, S. L.; Botton, G. A.; Savrasov, S. Y.; Szotek, Z.; Temmerman, W. M.; Sutton, A. P. *Phys. Status Solidi A*, **1998**, *166*, 429.

[128] Becke, A. D. *J. Chem. Phys.*, **1996**, *104*, 1040.

[129] Perdew, J. P.; Ernzerhof, M.; Burke, K. *J. Chem. Phys.*, **1996**, *105*, 982.

[130] Franchini, C.; Bayer, V.; Podloucky, R.; Paier, J.; Kresse, G. *Phys. Rev. B*, **2005**, *72*, 045132.

[131] Allen, T. L. *J. Am. Chem. Soc.*, **1956**, *78*, 5476.

[132] Brewer, L.; Bromley, L. A.; Gilles, P. W.; Lofgren, N. L. *Chemistry and Metallurgy of Miscellaneous Materials*. Paper No. 6. McGraw-Hill: New York, 1995. NNES-IV-19B.

[133] Doerner, A. H. *U. S. Bur. Mines Technical Paper*, **1937**.

[134] Gregory, N. W.; Burton, P. R. *J. Am. Chem. Soc.*, **1953**, *75*, 6054.

[135] Sime, R. J.; Gregory, N. W. *J. Am. Chem. Soc.*, **1960**, *82*, 800.

[136] Wilson, A. V.; Roberts, A. J.; Young, N. A. *Angew. Chem. Int. Ed.*, **2008**, *47*, 1798.

[137] Primas, H.; Müller-Herold, U. *Elementare Quantenchemie*. Teubner: Stuttgart, 1990.

[138] Cyvin, S. J. *Molecular Vibrations and Mean Square Amplitudes*. Elsevier: Amsterdam, 1968.